

Non-Invasive Functional MRI Methods for Measuring Cerebral Metabolism in Patients with
Cerebrovascular Disease

By

Spencer Leon Waddle

Dissertation

Submitted to the Faculty of the
Graduate School of Vanderbilt University
in partial fulfillment of the requirements
for the degree of

DOCTOR OF PHILOSOPHY

in

Chemical and Physical Biology

August 12, 2022

Nashville, Tennessee

Approved:

Manus Donahue, Ph.D.

Adam Anderson, Ph.D.

Lori Jordan, M.D. Ph.D.

Kevin Harkins, Ph.D.

Bennett Landman, Ph.D.

ACKNOWLEDGMENTS

Thank you to the friends, family, and colleagues who supported me throughout my academic journey. It takes a village to train a student and to complete scientific work, and I appreciate everyone who assisted me along the way. Thank you to the NIH/NINDS for financial support, to the BRET office for excellent assistance in navigating the details of grant submission and my academic program, and to all of the Vanderbilt faculty and staff who assisted in data acquisition. Thank you to my mom, dad, and grandparents. I would also like to thank the following people for their academic and personal contributions: Dr. Manus Donahue, Dr. Lori Jordan, Dr. Meher Juttukonda, Maria Garza, Chelsea Lee, Niral Patel, Jarrod Eisma, Dr. Kalen Petersen, Dr. Alexandria Oviatt, Dr. Megan Aumann, Sky Jones, Dr. Lindsay Klofas-Kozek, Dr. Krystian Kozek, Steven Winter, Dr. John Clem, Dr. Edward Lyman, Dr. Krishnan Padmanabhan, Bob Wilder, Jason Kreidler, and Jamie Wilks.

TABLE OF CONTENTS

1. Introduction	1
1.1. Overview	1
1.1.1. Medical Imaging Modalities	4
1.2. Stroke and Moyamoya.....	7
1.3. Cerebral Hemometabolism and Compensation Mechanisms	10
1.4. MRI Physics.....	11
1.4.1. Relaxation Parameters	13
1.4.2. Standard MRI Scans and Applications	16
1.4.3. Specialized MRI Scans and Applications	18
1.5. Improving Measurement of Cerebral Metabolism for Clinical Applications	24
1.5.1. Oxygen Extraction Fraction (OEF).....	24
1.5.2. Cerebrovascular Reactivity (CVR).....	25
1.5.3. Cerebral Blood Flow (CBF).....	26
1.6. MRI Processing and Machine Learning Algorithms.....	27
1.6.1. Image Coregistration.....	27
1.6.2. Machine Learning Approaches	28
2. Classifying Intracranial Stenosis Disease Severity from Functional MRI Data using Machine Learning	29
2.1. Introduction	29
2.2. Materials and Methods	31
2.2.1. Participant Demographics.....	31
2.2.2. Acquisition.....	31
2.2.3. Analysis.....	32
2.2.4. Quantification of Observables.....	35
2.2.5. Statistical Considerations and Hypothesis Testing.....	36
2.3. Results	38
2.4. Discussion.....	44
2.4.1. Limitations	47
2.4.2. Conclusion	48
3. A Magnetic Resonance Imaging Study of Pre-Surgical Indicators of Revascularization Response in Adults with Moyamoya Vasculopathy	49
3.1. Introduction	49
3.2. Methods	51
3.2.1. Participants	51
3.2.2. MRI.....	51
3.2.3. Revascularization Surgery	52
3.2.4. Digital Subtraction Angiography	52
3.2.5. Analysis.....	53
3.2.6. Posterior Circulation Variants	54
3.2.7. Statistical Analysis and Considerations	55
3.3. Results	56
3.3.1. Demographics.....	56
3.3.2. Revascularization Response	56
3.3.3. Pre-Surgical Indicators of Revascularization Success	57
3.4. Discussion.....	60
3.4.1. Limitations	63
3.4.2. Conclusion	64
4. Vascular Space Occupancy and Refocused Dual-Echo Asymmetric Spin Echo Variants Improve Quantitative Estimates of Cerebral Metabolism	64
4.1. Introduction	64
4.2. Methods	67
4.2.1. Participant Recruitment.....	67
4.2.2. Acquisition.....	67
4.2.3. Image Analysis and Processing.....	69
4.2.4. Statistical Analysis	71

4.3. Results	71
4.3.1. Participant Demographics	71
4.3.2. Imaging Results	72
4.4. Discussion.....	74
4.4.1. Limitations	77
4.4.2. Conclusion	78
5. Conclusion	79

LIST OF TABLES

1. Demographic Information for Moyamoya Participants in Chapter 2.....	31
2. Parameter Definitions in Chapter 2	36
3. High-Performing Functional Parameters for Predicting Moyamoya Stenosis	39
4. Demographic and Comorbidity Information for Moyamoya Participants in Chapter 3	55
5. Demographic and Surgical Information for Participants in Chapter 3	56
6. Demographic and Comorbidity Information: Demographic Makeup	56
7. Demographic and MRI-Measured Parameter Estimates of All Participants in Chapter 4.....	72
8. Mean and Standard Deviation Values for TRUST and ASE Variants	75

LIST OF FIGURES

1. Internal Carotid Artery Angiography in Moyamoya.....	3
2. Intracranial Cerebrovascular Anatomy	8
3. Illustration of Microvascular Anatomy.....	9
4. Diagram of pseudo-Continuous Arterial Spin Labeling	18
5. Micro- and Nano-Scale Phenomena Responsible for the Blood Oxygenation Level Dependent (BOLD) Effect	20
6. T2-Relaxation-Under-Spin-Tagging (TRUST) Pulse Sequence.....	21
7. Conventional Asymmetric Spin Echo (ASE) Pulse Sequence	22
8. Representative Images for Cerebral Metabolic Parameter Maps at Three Stages of Moyamoya Impairment.....	34
9. High-Performing Physiological Parameters for Predicting Moyamoya Stenosis Compared to Conventional Parameters in Support Vector Machines.....	40
10. Group-Wise Comparisons of Physiological Parameters by Moyamoya Stenosis Group.....	41
11. High-Performing and Conventional Physiological Parameters Compared Between Moyamoya Group Illustrated in Box Plots	42
12. Predicting Recurrent Infarcts in Moyamoya Using Machine Learning and Group-Wise Comparisons	43
13. Comparisons Between CBF-Mean, CBF-std, and CBF-CoV, Three Related Parameters	45
14. Angiograms for Patients with a Good and Poor Response to Revascularization Surgery.....	57
15. Structural and Functional MRI in Moyamoya Participants with Good and Poor Response to Revascularization Surgery.....	58
16. Group-Averaged CVR Parameter Maps for Patients with Good and Poor Response to Revascularization	59
17. Group-Wise Comparisons Between Functional and Demographic Parameters which Distinguish Surgical Outcome	60
18. All Pulse Sequences for the Asymmetric Spin Echo (ASE) that are Investigated in Chapter 4	68
19. Comparison of Corresponding Single-Slice and Multi-Slice ASE Methods.....	69
20. Decay and Signal Fitting in Asymmetric Spin Echo	70
21. A Signal Montage for Each ASE Method and Each Echo	73
22. Representative Parameter Maps for all ASE Variants	74
23. TRUST and ASE Variant Mean Value Group-Wise Comparisons	74
24. Group-Wise Comparisons of Signal-to-Noise Ratio in All ASE Variants.....	76
25. Reproducibility Measures of all ASE Variants and TRUST	77
26. Physiological Parameters of TRUST and ASE Using only the First ASE Echo	78

Chapter 1. Introduction

1.1 Overview

Stroke is caused by stenosis, occlusion, or rupture of a blood vessel supplying the brain, and is the leading cause of adult disability in the United States¹. Despite advances in acute stroke care, 20-30% of strokes result in death within one month, and 70-80% cause long-term disability^{2, 3}. However, due to advancements in therapies to prevention stroke or lessen stroke risk factors (termed primary stroke prevention), as well as treatments to prevent stroke recurrence (termed secondary stroke prevention), the majority of strokes may be avoidable as risk factors become better-defined⁴. Therapies which have played an important role in mitigating stroke are improved medical management, aneurysm stabilization with aneurysm coils, as well as revascularization with surgical procedures and stenting^{5, 6}. Currently, when an ischemic stroke or transient ischemic attack occurs, blood vessels are primarily evaluated for large vessel steno-occlusion, which is interpreted along with the pattern of ischemic injury and changes in symptomatology, as these are better characterized and measurement techniques are more accessible. This procedure however does not capture the wide range of tissue-level compensation mechanisms that may be present in patients. To improve clinical outcomes in stroke, the research in this document is focused on translational studies developing novel analysis and magnetic resonance imaging (MRI) methods for assessing functional hemodynamics in patients with cerebral metabolic dysfunction. Cerebral metabolism is the consumption of nutrients, often discussed in terms of oxygen in this context, and is maintained through blood flow and response to metabolic stress to avoid stroke or other damage to tissue. Examples where these methods have been used to improve patient care and outcomes are chronic anemia, such as in sickle cell disease^{7, 8}, or vasculopathies including atherosclerosis^{9, 10}. These methods may also extend to other non-vasculopathic conditions where cerebral metabolism may be affected, such as Parkinsons^{11, 12}.

MRI-measured functional parameters have demonstrated applicability for assigning therapies, and diagnosing patients with cerebrovascular^{13, 14} conditions. However, though tissue function plays an important role in stroke risk, risk for cognitive impairment, and mechanisms for compensation in cerebrovascular disease, functional parameters are rarely considered in clinical settings. However, by improving the accessibility and interpretability of functional images, patient care could be improved greatly. The functional parameters that will be considered most thoroughly in this work are oxygen extraction fraction (OEF), cerebrovascular

reactivity (CVR), and cerebral blood flow (CBF). OEF is a particularly appealing physiological parameter as it reflects the cumulative balance of the cerebral metabolic rate of oxygen (CMRO₂) to oxygen delivered, and may provide a composite biomarker of inadequate tissue-level compensation mechanisms¹⁵⁻¹⁸. However, OEF has not been fully realized as a biomarker of stroke risk due to technical difficulties associated with measuring this parameter. CVR parameters inform on parenchymal response to metabolic stress, and can provide information on both magnitude and delay in response to a vascular stimulus. CVR has been used to inform treatment decisions for patients¹⁹. Large-scale implementation of CVR has been slowed by difficulties in standardizing vascular stimuli, and difficulties associated with image interpretation. CBF is now a more commonly implemented MRI metric, and methods for measuring it have recently been included as a standard sequence on Philips MRI-scanners, however there are still standing difficulties associated with establishing MRI measured CBF as a standard in clinical practice. Primarily, MRI measured CBF is prone to artifacts that make interpreting these images difficult. Unfortunately, in cases of atypical physiology such as cerebrovascular disease, CBF maps can show large artifacts that require specialized techniques to understand underlying physiology. As will be explored further in this text, specialized analysis techniques, e.g. machine learning, show promise for assisting in interpretation of artifacts that result from unique physiologies of cerebrovascular diseases as novel contrasts. By focusing on developing MRI and analysis methods for improving our implementation of MRI-measured functional parameters, the work in this dissertation aims to bring these specialized techniques closer to the mainstream clinical practice.

Developments in this work include novel MRI methods for measuring cerebral metabolism, as well as machine learning techniques to classify patients according to their risk of cerebrovascular incident. While development of non-invasive MRI methods for measuring these parameters will improve their accessibility and acceptance in clinical practice, our understanding of these parameters is largely informed by previously existing measurements of oxygen consumption. The gold standard for most cerebral functional metrics is O-15 Positron Emission Tomography (O-15 PET)²⁰⁻²². However, O-15 PET exposes patients to ionizing radiation, and requires specialized equipment, particularly an on-site cyclotron to create O-15, as it has a half-life of approximately 2 minutes and therefore must be used almost immediately after leaving the cyclotron. O-15 PET is also invasive, as it requires arterial injection and sampling. In contrast to PET, MRI can measure OEF, CBF, and CVR non-invasively and rapidly, typically 2-6 minutes for a functional scan, and also provides unique avenues for contrast, such as the blood oxygen level dependent (BOLD) effect, which is used for reactivity imaging in this work.

The primary disease of study in this dissertation is moyamoya. Moyamoya is an intracranial arterial steno-occlusive disease, and is characterized by development of compensatory arterial collateral networks and high stroke risk ^{23, 24}.

Figure 1 shows an angiogram of an internal carotid artery displaying typical moyamoya pattern. Distal segments of the ICA undergo stenosis, which can progress to include the middle cerebral artery, anterior cerebral artery, and in later stages of moyamoya, the posterior circulation as well, which is not shown in **Figure 1**. Surgical revascularization is a common treatment for moyamoya, however

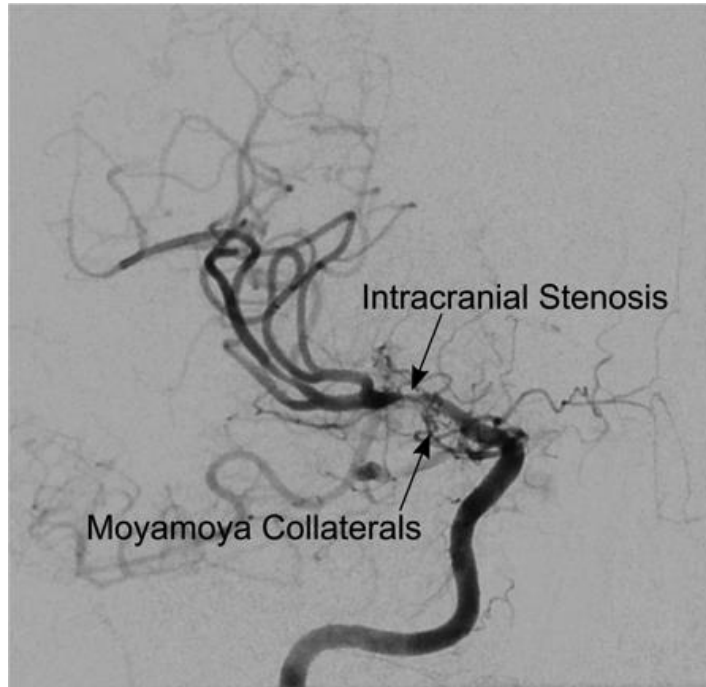


Figure 1. Internal Carotid Artery Angiography in Moyamoya. This is an angiogram of an internal carotid artery and its associated branches in a patient with moyamoya. The two important characteristics of moyamoya are shown here, where intracranial stenosis is causing reduced delivery of blood to proximal branches of the ICA, and compensatory moyamoya collaterals are developing to mitigate that reduction in blood delivery.

gaps persist in our abilities to (i) assign patient treatment options, e.g. surgery vs. conservative medical management and (ii) evaluate the impact of surgery on parenchymal health. Compared with atherosclerotic cerebrovascular conditions, moyamoya etiology is poorly understood, animal models do not exist, and randomized trials demonstrating surgical utility do not exist ²³⁻²⁵. Importantly regarding moyamoya, revascularization therapies do not have equal effectiveness for all individuals, and the demographics and physiology which determine surgical outcomes is not clear. More information on moyamoya, including how its unique physiology relates to the methods development pursued here, is given in further sections.

Given this background, the following three steps outline how each chapter in this thesis works towards improving our ability to quantify stroke risk in high risk populations:

1. Implement machine-learning techniques, which are becoming ubiquitous in imaging science, for the purpose of identifying recurrent stroke risk in patients with moyamoya.
2. Develop methodology for triaging moyamoya participants for therapies.

3. Improving methodology for measuring OEF in patients with local cerebrovascular impairment, as is common in vasculopathy.

1.1.1 *Medical Imaging Modalities*

While this work focuses on MRI, there are many alternate medical imaging modalities. Different imaging modalities are often implemented in tandem for diagnosis and research purposes, including in this dissertation, where gold standard angiography images are acquired with a separate imaging modality than MRI. Additionally, for one of the aims in this work, the primary motivation for developing MRI methods is to design a non-invasive and more accessible alternative to the O-15 PET method for measuring cerebral oxygen extraction. For these reasons, it is important to understand the basics of common medical imaging modalities to understand the context of this work. Depending on level of invasiveness, spatial and time resolution, ease of access, and possible therapeutic applications, different imaging modalities will be more suited for measuring different aspects of physiology and anatomy. A brief overview of these basics for many common imaging modalities is shown below.

*Magnetic Resonance Imaging (MRI)*²⁶: MRI has perhaps the widest array of applications of any imaging modality, due to its non-invasiveness and sensitivity to a wide range of tissue parameters. MRI can acquire structural images at sub-millimeter spatial resolution, functional images of brain activation, neuron fiber directionality maps, sub-second time-resolution real-time videos, and more. MRI has two major disadvantages, first of which is that obtaining an MRI can be cost prohibitive due to the costs associated with purchasing and maintaining an MRI scanner. Second, MRI is extremely sensitive to magnetic materials, which cause reduced image quality and can also be very hazardous. This drawback can often be avoided with specialized medical implants, however some implants, tattoos, piercings, dental work, and metal in the body from shrapnel or any other source can all be contraindications for MRI. The time and spatial resolution of MRI varies widely depending on the application. Some examples are high-resolution T1 images having 0.5mm resolution with minutes required for a single scan, and functional scans having a temporal resolution of a few seconds, but image resolutions of 3-5 mm.

Positron Emission Tomography (PET)^{27, 28}: PET utilizes intravenous or intraarterial injection of radio-labeled molecules, called radiotracers, typically to measure physiology and metabolism.

These radiotracers are designed to target specific physiology. One common example of this is F-18-fluorodeoxyglucose, which is a radiolabeled glucose molecule. Glucose molecules are disproportionately taken up by cancerous cells, and are for this reason, often used for cancer imaging. A second example, which is relevant to the methodology developed in this work is O-15²², which can be used to image oxygen metabolism (**Section 1.5**). Modern PET scanners can have a time resolution of 500 picoseconds, and spatial resolution of 4-6 mm. Due to high scanner costs, difficulties associated with acquisition of radiolabeled molecules, and exposure to ionizing radiation from injected radiotracers, accessibility to PET may be limited. The MRI methods developed in this work are, in part, intended as an alternative to invasive and expensive O-15 PET methods for measuring cerebral hemometabolism. One study found that the overall effective dose from an FDG PET scan was 6.23 mSv.

Computed Tomography (CT)^{28, 29}: CT uses rapidly axially rotating x-ray sources and detectors to acquire high-resolution 3-dimensional images. It is sensitive to differences in density, more specifically Hounsfield units, which are a measure of a materials radioabsorption. Because of this sensitivity, CT is ideal for imaging bones, and is therefore often used to provide a high-resolution image of the skull in MRI and ultrasound experiments that need accurate 3D representations of the skull for simulation purposes. However, medical applications of CT are ubiquitous, useful for investigating tumors, stroke, or angiography if implemented with an intravenous contrast agent, known as CT Angiography (CTA). Modern CT scanners acquire a temporal resolution of 66-138 ms and a spatial resolution of 0.5-0.625 mm. CT poses the highest exposure to ionizing radiation of the methods listed in this section, with radiation dosage from one study found to be 7.22 – 25.95 mSv, depending on protocol.

*Digital Subtraction Angiography (DSA)*³⁰: Like CT, DSA uses x-rays to acquire images, however DSA images are typically acquired in a single projection, rather than axially acquired 3-D images, though 3-D images are possible. Additionally, DSA utilizes multi-vessel intraarterial injection of contrast agents and each imaging acquisition requires radiation. In this work, DSA is used as the gold-standard angiography technique for identifying arterial stenosis and neoangiogenic collaterals.

*Single Photon Emission Computed Tomography (SPECT)*³¹: SPECT is a less commonly implemented imaging modality, because many of its applications are similar to PET, though SPECT images are more difficult to quantify. However, SPECT is sometimes used in cerebral

metabolism imaging similarly to PET, though SPECT is significantly less invasive in this application, as SPECT does not require arterial blood sampling.

*Ultrasound*³²: Like MRI, ultrasound has a wide range of applications, largely due to non-specialized ultrasound technology being relatively affordable and minimally invasive. Ultrasound can be used to measure both physiology and anatomy, and has growing relevance for therapeutic applications as well, particularly in the specialized technique high intensity focused ultrasound (HIFU)³³. In cerebrovascular imaging, transcranial Doppler ultrasound is used to measure intracranial blood-flow velocities in the middle-cerebral-artery to determine stroke risk in children with sickle cell anemia³⁴. Ultrasound will have greatly varying resolution depending on application, with reduced penetration depth when acquiring higher resolution images. However, high-resolution ultrasound is considered to be resolution of 0.15mm or better, which can be acquired with a penetration depth of 5-6 cm.

*Infrared Spectroscopy*³⁵: Infrared spectroscopy is used to measure concentrations of biomolecules. In the applications in this work, infrared spectroscopy is not used to collect images, however. Infrared spectroscopy is used to acquire arterial oxygen saturation values via a pulse-oximeter clipped onto the participant's finger.

It is also important to note that with specialized equipment, it is possible to perform multiple imaging modalities simultaneously. The most common examples of this are PET-MRI and PET-CT. Conducting tests with these technologies can help to remedy some challenges of imaging with multiple modalities. For example, when images are collected with two different modalities at two separate time-points, the participant will not be positioned identically in both scans. To compare images quantitatively under these conditions, coregistration (**Section 1.6**) is required to ensure identical brain tissue is being compared between separate images. However, this is especially complicated when images have low spatial-resolution, as PET typically does. Therefore, by collecting MRI and PET, or CT and PET images simultaneously, the relative spatial correspondence of images from separate modalities can be determined with greater confidence.

1.2 Stroke and Moyamoya

Stroke is the disruption of nutrient-rich oxygenated blood to the brain parenchyma, i.e. the functional tissue, which is comprised of neurons and glial cells. Stroke is often caused by a ruptured blood vessel or an obstructed blood vessel, however stroke can have other causes as well, such as a narrowed blood vessel or reduced oxygen content of the blood. Brain tissue cannot effectively operate anaerobically; therefore even brief disruptions in blood supply can damage tissue³⁶. This urgency in treating stroke is the origin of the colloquialism “time is brain.” More quantitatively, 1.9 million neurons are lost per minute of untreated stroke, approximately equivalent to the neuronal loss due to 3.6 years of normal brain aging³⁶. Approximately 795,000 Americans have a stroke each year³⁷, and stroke remains the leading cause of adult disability and second-most cause of death, with 20-30% of strokes resulting in death within one month, and 70-80% causing long-term disability^{2, 3}. However, stroke risk factors are becoming increasingly well understood, such as high blood pressure, diabetes mellitus, and smoking. As a result, stroke incidence has been decreasing over time³⁸. Additionally, improvements in acute stroke treatment play a role in improving outcomes to stroke. The goal of acute stroke treatment is to induce reperfusion as rapidly as possible, either by pharmacological or mechanical means. Intravenous recombinant tissue plasminogen activator (rtPA) is the current standard of care for acute stroke, however this treatment in most cases must be administered within 4.5 hours of stroke symptom onset, and most stroke patients do not receive this treatment. Recent studies have identified methods for extending the window for rtPA administration to 24 hours with advanced blood-flow imaging^{39, 40}. Thrombectomy and proximal artery occlusion are alternative treatments for acute stroke, however patients must be taken to specialized centers for these procedures⁴¹.

Diseases can increase the likelihood of stroke, one general class of these is cerebrovascular disease (CVD). The most common CVD is atherosclerosis, a disease that is typically extracranial¹. When extracranial, atherosclerosis is a relatively well characterized disease with standardized treatment procedures, such as that from the North American Stenting vs. Carotid Endarterectomy Trial (NASCET)⁴², and the Carotid Revascularization Endarterectomy versus Stenting Trial (CREST)⁴³. Similar trials for intracranial atherosclerosis, Stenting vs. Aggressive Medical Management in Patients at Risk for Stroke with Intracranial Stenosis (SAMMPRIS) and Vitesse Intracranial Stent Study for Acute Ischemic Stroke Therapy (VISSIT) found that aggressive medical management was the preferable treatment for intracranial stenosis. However aggressive medical management for intracranial stenosis

resulted in 12.2-15.5% recurrent stroke, compared to only 7% of patients with extracranial atherosclerosis who underwent carotid endarterectomy. This tendency towards poorer outcomes for intracranial CVD is why while intracranial CVD is less common it is still responsible for 7-24% of new strokes¹, and therefore requires improved treatments to reduce harm from these diseases. This lack of knowledge for treating intracranial CVD is the motivation for focusing on moyamoya in this study, a type of intracranial CVD that is particularly poorly characterized. The functional methods developed in this work will improve surveillance of and aid in treatment decisions for moyamoya and cerebrovascular disease generally.

Moyamoya is an intracranial arterial stenocclusive disease affecting the supraclinoid internal carotid artery (ICA) and its proximal branches, which leads to delayed blood arrival times²¹, delayed reactivity timing⁹, and development of compensatory collateral vessels. Moyamoya is clinically relevant as it incurs a seven-fold increase in stroke risk compared to age- and race-matched adults⁴⁴ and treatment regimens, which may comprise either medical management or surgical revascularization, have not

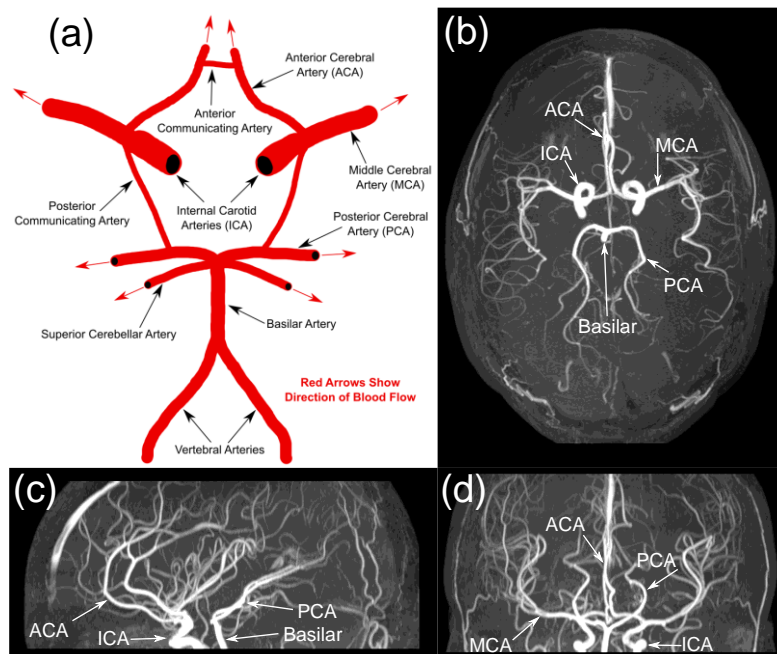


Figure 2. Intracranial Cerebrovascular Anatomy. An illustration (a) and magnetic resonance angiograms (b-d) showing intracranial vascular anatomy. All of the main vessels are illustrated in a simple view in (a), which shows an axial projection, as in (b). (c) and (d) show the same image volume as in (b), except from a coronal (c) and sagittal (d) projection. ICA = Internal Carotid Artery, ACA = Anterior Cerebral Artery, MCA = Middle Cerebral Artery, PCA = Posterior Cerebral Artery.

been established by randomized clinical trials. The current standard for identifying disease severity in moyamoya is stenosis grading of major intracranial vessels with catheter angiography, however this procedure carries perioperative risk and exposes patients to ionizing radiation, and for these reasons is suboptimal for surveillance. In moyamoya disease, stenocclusion of the intracranial segments of the ICA and its proximal branches causes the development of an elaborate network of collateral vessels⁴⁴. Moyamoya often progresses to involve bilateral intracranial arteries, but may begin as unilateral impairment⁴⁴. Stenosis usually occurs in the ICAs, anterior cerebral arteries (ACAs), and middle cerebral arteries (MCAs), with

the basilar artery and the posterior cerebral arteries (PCAs) being affected least often. Magnetic resonance angiographies and an illustration of cerebral vascular anatomy are shown in **Figure 2**. Moyamoya can be idiopathic or have a secondary presentation to other diseases such as sickle cell disease, obesity, diabetes, or atherosclerosis, though the causal relationship between these diseases and moyamoya is not clear. Idiopathic moyamoya is rare (<1 case per 100,000 children in North America)⁴⁵, while secondary moyamoya presentation is more common²⁵. Our understanding of moyamoya etiology is currently in development, animal models do not exist, and there is no known treatment to reverse or stop moyamoya disease progression. Current moyamoya treatments aim to improve blood flow to impaired regions to reduce risk of ischemia and stroke²⁴. This is typically accomplished with anti-platelet agents, or revascularization surgery when medication is insufficient, though these treatments do not reverse disease progression^{24,25}. The lack of disease-modifying treatment options and a poor understanding of etiology and physiology makes moyamoya a pressing subject for research.

Although moyamoya is the disease of focus in this dissertation, these techniques could be applied to a range of diseases, particularly other cerebrovascular diseases, though the general methodology could be applied to identify characteristic physiology for any disease with cerebral functional hemodynamic abnormality. For example, the functional imaging methods discussed in this work are also being implemented in other studies investigating sickle cell disease⁴⁶, Alzheimer's disease⁴⁷, Parkinson's disease, and Huntington's disease.

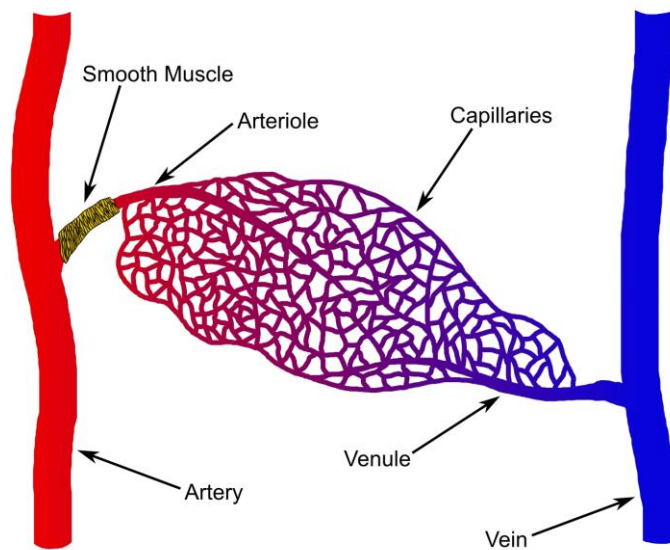


Figure 3. Illustration of Microvascular Anatomy. Oxygenated blood is flowing from the heart through the arteries, and branches out into arterioles, the diameter and flow through which is controlled by smooth muscle. The arterioles branch into capillaries, which form the blood-brain barrier, and are the exchange site of nutrients and waste products with tissue. Capillaries collect into venules, and drain into veins. Blood flows through the veins and returns to the lungs for oxygenation to return to circulation.

1.3 Cerebral Hemometabolism and Compensation Mechanisms

Micro- and macrovascular anatomy and function are affected in CVD, including by (i) delayed blood arrival, (ii) reduced vascular compliance, (iii) heterogeneous flow velocities, and (iv) large vessel stenosis. Understanding this underlying physiology is important for understanding why and how cerebral metabolic parameters are measured.

The anatomy of microvasculature is illustrated in **Figure 3**. After being oxygenated in the lungs, blood is pumped in to the arteries by the heart. This creates perfusion pressure, which causes blood to be pushed into the arterioles, which branch off of the arteries. Blood flow to tissue is controlled by smooth muscle, which largely responds to pH changes in the blood, driven by the pH difference between arterial and venous blood, where venous blood has pH 7.369 ± 0.120 and arterial blood has pH 7.384 ± 0.124 ⁴⁸. Arterioles branch further to form diffuse beds of capillaries, which serve as the exchange site, also called the blood-brain barrier, for nutrients and waste products between blood and tissue. After passing through the capillary beds, blood is deoxygenated and the capillaries come together into a venule, which in turn flows into a vein. The blood is then returned to the lungs, and circulation repeats. The amount of blood that flows into the capillary beds is determined by metabolic need, and is controlled by the smooth muscle, which can dilate and contract to control flow into the arterioles. The influx of oxygenated blood from dilatation, caused by the smooth muscle, is the origin of the BOLD effect. The blood that flows into the capillaries provides much greater nutrient content to tissue than is needed for neuronal activity, likely to guarantee neuronal survival under metabolically stressful conditions. This disproportionate response in blood supply to tissue is important for understanding the BOLD effect, and will be revisited in **Section 1.4** where the MR physics of BOLD is discussed.⁴⁹

As CVD progresses, vasculature can respond to reduced blood supply through compensation mechanisms. However when these compensation mechanisms are exhausted, stroke can occur. Moyamoya progression manifests as tissue-level hemodynamic changes due to arterial occlusion, development of arterial collaterals, and exhaustion of cerebrovascular reserve^{50, 51}. These physiological processes cause changes in baseline cerebral blood flow (CBF; rate of blood delivery to tissue), cerebrovascular reactivity (CVR; ability of microvasculature to increase flow to meet increased demand), or oxygen extraction fraction (OEF; ratio of oxygen consumed to oxygen delivered).

It is imperative that brain tissue receives a constant and steady supply of arterial blood to supply oxygen, glucose, and other metabolites as well as to carry away waste products. Cell death causes irreversible tissue damage after only 5 minutes of interrupted blood supply. The equation that describes tissue metabolism is shown below:

$$CMRO_2 = CBF \cdot OEF \cdot [Hb] \cdot C_a \quad (1)$$

Where $CMRO_2$ is the cerebral metabolic rate of oxygen here in mL O_2 / 100g Tissue / min, CBF is cerebral blood flow in mL blood / 100g Tissue / min, OEF is oxygen extraction fraction is unitless as O_2 consumed / O_2 delivered, [Hb] is hemoglobin in g / mL (typically must be converted from g/dL), and C_a is the oxygen carrying capacity of hemoglobin and is 1.34 mL / g.

Maintaining oxygen supply to tissue corresponds to maintaining $CMRO_2$ in **Equation 1**. Therefore, CBF and OEF can be elevated in response to reductions in [Hb], as occurs in Sickle Cell Anemia. In terms of microvasculature, CBF is elevated by maintaining dilation of the smooth muscle, and OEF is elevated as proportionally more oxygen from blood is extracted in the capillaries. Both of these compensation mechanisms are limited however. When blood flow can no longer be elevated from baseline, there will be no room for the vasculature to respond to stress. This room to respond to metabolic stress is called the cerebrovascular reserve, and testing this reserve is the underlying principle behind CVR imaging. When compensation mechanisms are exhausted, CBF can no longer be elevated, OEF can no longer be elevated, and cerebrovascular reserve is exhausted, $CMRO_2$ can no longer be maintained, and stroke occurs. Understanding the status of CBF, OEF, and CVR therefore give insight into stroke risk, and potentially into responses to therapies as well. This is the reason these methods are used to interrogate cerebral metabolism.

1.4 MRI Physics

To understand the MRI methods development component of **Chapter 4**, as well as the principles behind other methods used here, such as T2-Relaxation-Under-Spin-Tagging (TRUST) and pseudo-Continuous Arterial Spin Labeling (pCASL), it is necessary to review some relevant MRI physics principles⁵². The following section is a description of all of the most important details for my understanding of MRI, essentially what I would have wanted access to when I began my PhD.

When placed in a magnetic field, the energy of nuclear states can diverge. This is known as the Zeeman Effect, and these energy differences between states are fundamentally what is manipulated in MRI to acquire images. Outside of specialized cases⁵³⁻⁵⁵, MRI measures signal from the single proton nuclei of hydrogen in H₂O molecules, and these hydrogen protons have two states in a magnetic field. These states are the lower energy spin up state, aligned with the external field, and the higher energy spin down state. The word spin comes from the nuclear parameter spin, which refers to an inherent angular momentum that the nuclei possess. The nuclei exist in a superposition of the up and down state, however the individual wave functions overlap with one another on the scale of proton-densities utilized in MRI, and therefore quantum effects are not relevant, and this ensemble of spins is treated with classical electromagnetic theory. When aligned with a strong magnetic field, called \vec{B}_0 and measured in Tesla, these protons form a magnetic moment, which will precess about \vec{B}_0 and absorb externally applied energy in the form of radio-frequency (RF) pulses, the fields of which are referred to as B_1 . The frequency of the B_1 pulse will be selected to match the precession frequency of the magnetic moments, known as the Larmour Frequency, ω_0 , determined by a nuclei-dependent constant called the gyromagnetic ratio, γ , and the strength of \vec{B}_0 . This relationship is $\omega_0 = \gamma \cdot B_0$ where the gyromagnetic ratio for hydrogen is $\gamma = 42.58 \text{ MHz/T}$ or $\gamma = 267.7 \text{ Mrad/T}$ when expressed in radians. Because the RF pulse is played at the Larmour Frequency, \vec{B}_1 will be perpendicular to the magnetic moment \vec{M} . This relationship is often envisioned and handled mathematically by operating in a rotating reference frame, also rotating in accordance with the Larmour Frequency. When absorbing energy from this radio-frequency pulse, the spins will tilt away from alignment with the main magnetic field, as described by the right-hand rule, the motion of which is referred to as nutation. These moments will then relax back to equilibrium, during which time they emit energy detectable via magnetic induction with an antenna, called a coil. Engineering of specialized MRI coils is a field in and of itself. Coil design is complicated, because MRI relies on the generation of very precise gradient fields. These gradients can be used for multiple purposes, such as diffusion labeling, flow velocity selective labeling, and crushing of residual MRI signal. However, these gradients will be used ubiquitously in MRI for slice selection, which is the process by which slices of tissue are imaged in isolation from the rest of the subject. Stacks of these slices create three-dimensional volumes, however three-dimensional volumes can also be acquired directly in MRI, called 3D acquisition. Both 2D and 3D acquisition have advantages and therefore both are utilized in MRI. For slice selection, first a gradient is applied.

This gradient causes the magnetic field to vary linearly through space. Based on the relationship mentioned previously, $\omega = \gamma \cdot B$, the spatial variation of the gradient will correspond to a variation of Larmour frequency. An RF pulse can be applied which is tuned to the frequency that corresponds to a slice that we are interested in imaging, which will cause the magnetic moment of that specific region to nutate. The total amount of rotation can be selected based on RF pulse strength and duration through an equation derived by integrating the frequency equation given earlier as $\phi = \gamma \cdot B_1 \cdot t$. The region of space that is excited is a slice that can now be imaged. By applying magnetic field gradients, always facing in the axial-direction though the intensity of which varies in all directions, the ensemble of these moments can be wound and unwound in space, corresponding to traversal through frequency space, also called k-space. By recording the signal at various points in k-space, a frequency-domain image is collected. These k-space images can be two- or three- dimensional, with advantages and drawbacks to these acquisition styles. Via a Fourier transform, the k-space image can be converted into a spatial domain image, i.e. the images we are familiar with seeing in MRI. The signal that this ensemble of protons emits will depend on the direction and magnitude of the magnetic moment when each line of k-space is acquired. Only the lateral component of the magnetic moment is measured in MRI, and the lateral direction of the moment is referred to as the phase. It is possible to select for these two parameters, the direction and magnitude of the magnetic moment, by utilizing carefully-selected radio-frequency pulses and knowledge of how the moments will relax back to their equilibrium after being excited. This sequence of radio-frequency pulses is referred to as a pulse-sequence, and the complexity of pulse sequences can vary greatly. MRI contrast will depend on how protons relax in their local environments, the specific study of which is called relaxometry. In some cases, as with the use of a vasodilatory stimulus in the work presented here, the local proton relaxation can be controlled as well as the MRI pulse sequence. MRI pulse sequences make careful use of the parameters that describe MRI relaxation, and therefore these relaxation parameters are important for MRI methods development and contrast mechanisms. The work presented here focuses partly on developing a novel MRI pulse sequence, therefore the following introductory sections will discuss MRI contrast mechanisms and how they relate to the methods developed in this work.

1.4.1 Relaxation Parameters

Relaxation parameters are most often discussed in terms of constants, known as T_1 , T_2 , T_2' (tee-two-prime), and T_2^* (tee-two-star), each of which are typically in units of seconds. The

inverse of these is R_1 , R_2 , R_2' , and R_2^* , which are in units of 1 / seconds, and therefore are rates of relaxation. Since, $R_2' = R_2 - R_2^*$, R_2' is discussed less often, partially because it is a linear combination of R_2 and R_2^* , and partially because the physical property which R_2' represents causes decay that is recoverable in MRI, and therefore is not relevant in many MRI applications. R_2 is caused by spin-spin interactions on the microscopic or mesoscopic scale. R_2' is caused by local field inhomogeneity on the macroscopic scale. R_2^* is the fastest decay constant, and is the combination of decay from both R_2 and R_2' sources. R_1 is caused by spin-lattice interactions. R_1 and the R_2 parameters are independent from one another, and describe longitudinal relaxation and transverse decay respectively. The motion of magnetic moments is described by an empirical system of differential equations known as the Bloch Equations. Expressed as a vector, the Bloch Equations are:

$$\frac{d\vec{M}}{dt} = \gamma \vec{M} \times \vec{B}_0 + \frac{1}{T_1} (M_0 - M_z) \hat{z} - \frac{\vec{M}_{\text{Perpendicular}}}{T_2} \quad (2),$$

where \vec{M} is the magnetic moment vector, \vec{B}_0 is the main magnetic field vector, M_0 is the magnitude of the magnetic moment at equilibrium, M_z is the component of \vec{M} that is parallel to \vec{B}_0 , and $\vec{M}_{\text{Perpendicular}}$ is the component of \vec{M} that is perpendicular to \vec{B}_0 . Expressing the Bloch Equations in Cartesian coordinates:

$$\frac{dM_z}{dt} = \frac{M_0 - M_z}{T_1} \quad (3)$$

$$\frac{dM_x}{dt} = \omega_0 M_y - \frac{M_x}{T_2} \quad (4)$$

$$\frac{dM_y}{dt} = -\omega_0 M_x - \frac{M_y}{T_2} \quad (5)$$

Where x and y are orthogonal to the main magnetic field B_0 , and z is parallel with B_0 ; ω_0 is the Larmour Frequency. Just a few techniques form the foundation of most modern MRI sequences and take the form of exponential decay equations.

T₁ Recovery Solution

This equation describes the longitudinal component of the magnetic moment following an inversion, i.e. 180 degree excitation from equilibrium. The magnetic moment will then recover to equilibrium according to the following equation.

$$\frac{M_z}{M_0} = 1 - 2e^{-\frac{TI}{T_1}} \quad (6)$$

Where T_1 is the time between excitation and the sequence read-out. However, in most cases, the magnetization will not be at equilibrium following successive excitations. In this case, we can use the repetition time (T_R), or the time between consecutive excitations for a solution that accounts for multiple acquisitions.

$$\frac{M_z}{M_0} = 1 - 2e^{-\frac{TI}{T_1}} + e^{-\frac{TR}{T_1}} \quad (7)$$

T₂ Decay Solution*

When excited into the transverse position, via a 90 degree excitation pulse, the transverse component of the magnetization will begin to decay rapidly due to both T_2^* and T_2' effects. This decay with time, t , is described by the following equation.

$$\frac{M_{xy}}{M_0} = 1 - e^{-\frac{t}{T_2^*}} \quad (8)$$

As above, this first solution does not account for multiple acquisitions, and therefore a more complete solution is:

$$\frac{M_{xy}}{M_0} = e^{-\frac{TR}{T_1}} \cdot \left(1 - e^{-\frac{t}{T_2^*}}\right) \quad (9)$$

Where $e^{-\frac{TR}{T_1}}$ is the magnitude of the longitudinal component of the magnetic moment after recovering for a full TR , at which point it is excited again. The T_2^* decay is applicable in sequences where readouts are occurring very rapidly. Gradient echo sequences, also sometimes called echo planar imaging (EPI), are rapid and commonly implemented in situations where T_2^* contrast is of interest.

T₂ Decay Solution

If after an excitation pulse, a 180-degree pulse is applied to reverse the phase of the magnetization vector, some signal can be recovered. As described previously, T_2 decay is caused by spin-spin interactions, T_2' however represents signal lost to local field inhomogeneity and therefore this signal will recover. The signal measured by a pulse sequence like this is described by the following equation:

$$\frac{M_{xy}}{M_0} = 1 - e^{-\frac{TE}{T_2}} \quad (10)$$

Where T_E is the echo time, and is the time between the excitation pulse and readout in a spin-echo sequence. Because R_2' can be recovered in a spin-echo sequence, spin echo sequences are governed by R_2 decay. However, since a gradient-echo does not have any spin refocusing, gradient-echo sequences are governed by R_2^* decay and are therefore much more susceptible to field inhomogeneity. R_2 -weighted images are less affected by this drawback. This sensitivity to susceptibility can be a disadvantage, e.g. when a patient has dental work that causes signal loss in the frontal lobe, or an advantage, e.g. when susceptibility can be used as a source of contrast as it is in BOLD imaging. There is a similar solution for spin-echo sequences when accounting for multiple repetition times.

$$\frac{M_{xy}}{M_0} = e^{-\frac{TR}{T_1}} \cdot \left(1 - e^{-\frac{TE}{T_2}}\right) \quad (11)$$

1.4.2 Standard MRI Scans and Applications

The focus of this research is on developing novel MRI methods for measuring cerebral metabolism, however standard anatomical scans are also acquired in all cases. These standard scans are commonly applied in clinical practice as well as research, and can help to characterize a cohort by defining presence of infarcts, tumors, and other structural abnormalities. Without standard structural MRI, it can sometimes be difficult to interpret specialized functional imaging. The physical difference between these scans is the number and timing of applied RF pulses and gradients.

T_1 -Weighted Magnetization Prepared Rapid Gradient Echo (MPRAGE)⁵⁶: MPRAGE is the most common scan for acquiring high-resolution structural images using a three-dimensional readout, a 180 degree pre-pulse, and rapid gradient-echo acquisitions. MPRAGE produces high contrast between grey and white matter, and can acquire sub-millimeter resolution on modern hardware.

T_2^ -Weighted Gradient Echo*: In accordance with **Equation 9**, T_2^* -weighted images can be acquired. T_2^* -weighted images are highly vulnerable to susceptibility effects. This results in large artifacts in regions with inhomogeneous magnetic field, particularly near the sinuses, but also enables BOLD imaging, where susceptibility effects from deoxygenated blood are used to measure neuronal activation and vascular response to stimulus.

T_2 -Weighted Spin Echo: From **Equation 11**, T_E and T_R can be chosen to acquire a T_2 -weighted image. These images can be used for detection of infarcts, particularly when modified for a FLAIR sequence, below.

*Fluid Attenuated Inversion Recovery (FLAIR)*⁵⁷: The T_1 of cerebral spinal fluid (CSF) at 3 Tesla is 4300 ms⁵⁸. Using this information along with **Equation 7**, it is possible to solve for a T_1 that completely nulls CSF signal. FLAIR uses this principle to produce a T_2 -weighted and CSF nulled image that has hyper-intensities in regions affected by stroke where macrophages can accumulate to clear tissue, and blood flow is reduced⁵⁹. As a result, FLAIR is the most reliable way to identify infarcted tissue using MRI.

*Diffusion Weighted Imaging (DWI) and Diffusion Tensor Imaging (DTI)*⁶⁰: Diffusion weighted and diffusion tensor MRI both use bipolar gradients to encode diffusion information. Diffusion weighted MRI, however, does not provide a direction to this diffusion, and is mostly used for early detection of stroke. Diffusion tensor imaging does provide direction information for diffusion, and can therefore be used for white matter fiber tracking and measuring nerve regeneration.

MRI Angiography^{61, 62}: MR angiographies are often considered separately from other standard structural MRI scans. This distinction may be made because angiography scans utilize MR contrast agents, especially chelated gadolinium, more often than other structural applications. Angiography utilizing contrast agents takes advantage of an inflow effect, however there are two common non-contrast MRI angiography methods. These are Time of Flight Angiography (ToF), and Phase Contrast Angiography (PC). ToF uses an RF pulse to label blood in the neck, and images this blood once it arrives in the brain, this labeled blood having flown into the cerebral vessels. PC uses a bipolar gradient to label blood flowing at arterial velocities, and the acquired velocity map highlights the arteries.

Many of these scans play a role in diagnosis of stroke. For example, lesions which have not cleared tissue and become fluid filled can be detected on FLAIR, in which they are hyper-intense. As lesions become chronic, they can be detected on T_1 , where they are dark and approaching CSF signal. DWI imaging can detect acute lesions, where the apparent diffusion coefficient will be reduced in tissue suffering from insufficient blood flow. Infarct type can also be defined using imaging, where cerebral infarcts are often defined as being greater than 3mm in at least one dimension, and are white matter hyperintensities otherwise.

1.4.3 Specialized MRI Scans and Applications

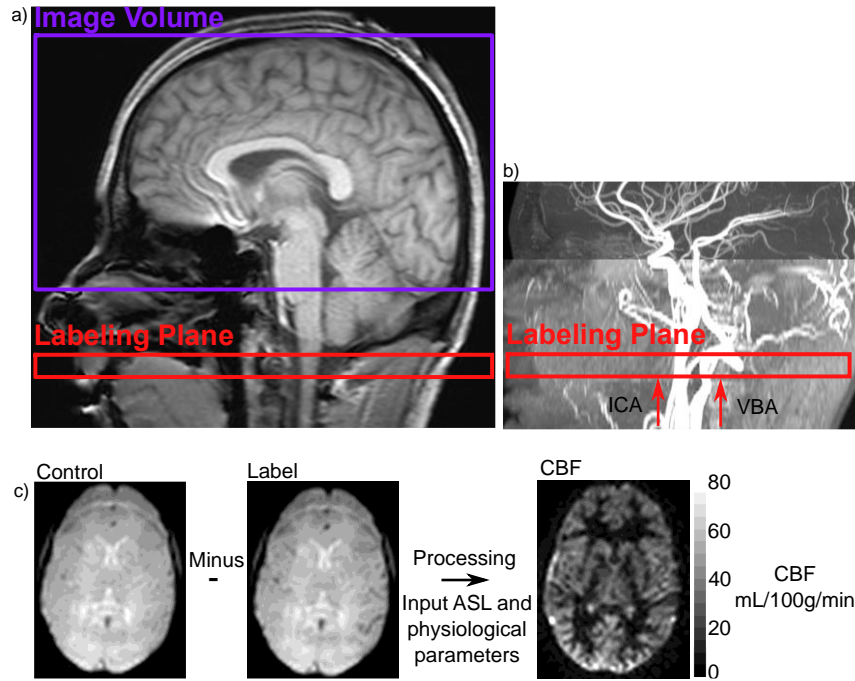


Figure 4. Diagram of pseudo-Continuous Arterial Spin Labeling. (a) shows an anatomical image, overlaid with the image volume and labeling plane associated with pseudo-continuous arterial spin labeling. (b) shows the vessels through which blood is delivered to the brain and passes through the labeling plane, where arterial blood-water is labeled with radiofrequency pulses. A labeled and non-labeled image are shown in (c), subtraction of which and processing can yield a quantitative map of cerebral blood flow.

Arterial Spin Labeling (ASL)

A diagram demonstrating the principles behind ASL is shown in **Figure 4**. Blood in the neck is magnetically labeled as it flows into the brain. The labeling plane is positioned so that blood is flowing orthogonal to the labeling plane, and the imaging volume covers as much of the brain as possible. An image of the brain is acquired, after waiting a post-label delay, for magnetically labeled blood to flow into the brain; this is the label image. Additionally, an image is acquired without a label; this is the control image. The difference between the control and label image shows a map where the labeled blood flowed during the post-label delay, and can be converted to a quantitative map of cerebral blood flow by using the flow modified Bloch equation⁶³. The method used in this work is called pseudo-continuous arterial spin labeling (pCASL), in which a rapid train of RF pulses approximate a continuous RF field. This method works due to a phenomenon known as flow-driven adiabatic inversion, in which the flow of blood through the applied gradient field improves labeling. Quantitative analysis of pCASL is described by the following equation, which is derived from the Bloch equations modified to consider flow, as is the case in arteries⁶⁴:

$$CBF = \frac{\lambda}{T_{1app}} \cdot \frac{M_{control}(TR) - M_{label}(TR)}{2M_0(TR)} \quad (12)$$

Which can be further analyzed with a dual compartment model for inside and outside the vascular system, which cannot be solved analytically, and must be fit for CBF^{65, 66}:

$$M_{control} - M_{label} = \frac{2M_0\alpha \cdot CBF}{\lambda} \cdot \frac{e^{-\delta R_{1a}}}{R_{1app}} \left[e^{(\delta-w) \cdot R_{1app}} - e^{(\delta-\tau-w) \cdot R_{1app}} \right] \quad (13)$$

Where M_{label} is the magnetization of the labeled pCASL image, $M_{control}$ is the magnetization of the unlabeled control pCASL image, M_0 is equilibrium magnetization, f is CBF in mL/g/s, $\alpha = 0.85$ is pCASL labeling efficiency, $\lambda = 0.9 \text{ ml/g}$ is the whole-brain blood-brain partition coefficient, $\delta = 1.5s$ is the tissue transit time, $R_{1a} = 0.59 \text{ s}^{-1}$ is the longitudinal relaxation rate for oxygenated macrovascular arterial blood water at 3.0T⁶⁷, R_{1app} is the apparent longitudinal relaxation rate of perfused tissue ($R_{1app} = R_{1,Tissue} + \frac{f}{\lambda}$), $R_{1,Tissue} = 0.77 \text{ s}^{-1}$, w is the pCASL post-label delay time, and τ is the pCASL labeling duration. CBF is converted to units of mL/100g/min by multiplying by a factor of 6000.

Finally, pCASL can be processed with a single compartment model, which assumes complete mixing of labeled blood-water with cerebral blood-water⁶³:

$$CBF = \frac{6000 \cdot \lambda \cdot (M_{control} - M_{label}) \cdot e^{\frac{PLD}{T_{1blood}}}}{2 \cdot \alpha \cdot T_{I_1} \cdot M_0 \cdot \left(1 - e^{-\frac{\tau}{T_{1blood}}} \right)} \quad (14)$$

Oxygenated vs. Deoxygenated Hemoglobin

In deoxygenated hemoglobin, the iron molecules have unpaired electrons and therefore produce magnetic fields in response to an externally applied magnetic field, i.e. deoxygenated hemoglobin is a paramagnetic protein. However, the iron in oxygenated hemoglobin does not have unpaired electrons, and is a diamagnetic protein, and produces much weaker magnetic fields in comparison to its paramagnetic counterpart. This difference in magnetic properties results in different magnetic susceptibilities for arterial and venous blood, which can be detected with MRI as decreased T_2 and T_2^* caused by deoxygenated hemoglobin⁶⁸. A diagram demonstrating this phenomenon is shown in **Figure 5**. Due to its paramagnetism, deoxyhemoglobin produces greater magnetic fields in the MRI scanner compared to oxyhemoglobin. In MRI, we measure signal primarily from the nuclei of hydrogen atoms in water molecules. These protons are perturbed by fields from hemoglobin, and therefore have weaker

MRI signal for deoxyhemoglobin compared to oxyhemoglobin. Therefore, arterial blood gives stronger MRI signal than venous blood. This difference can be quantified to calibrate the percentage oxygen saturation that corresponds to different MRI-measured parameters. The difference between oxy- and deoxyhemoglobin is the basis for a large part of this work, and the following methods. Generally, this is referred to as the BOLD effect.

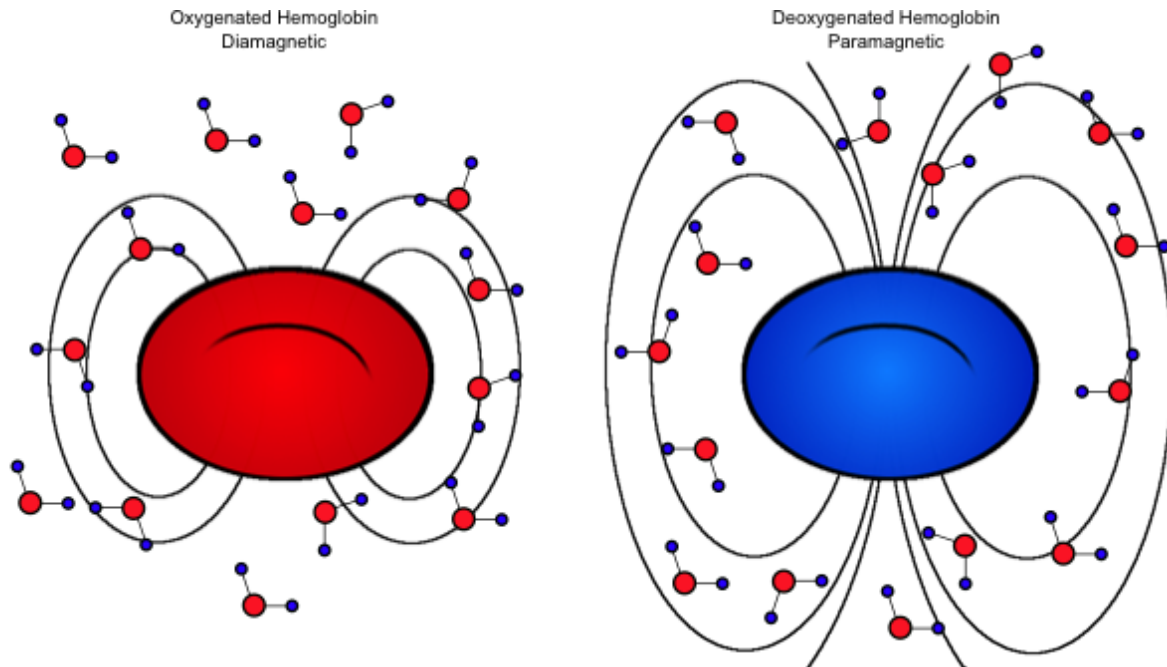
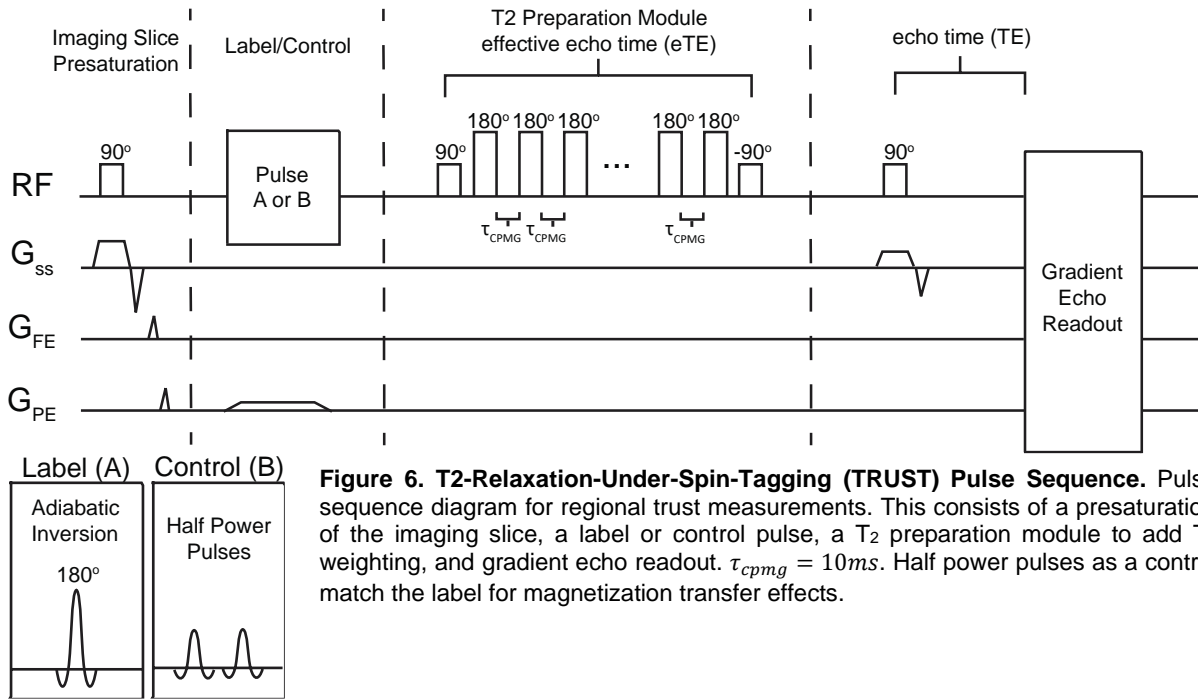


Figure 5. Micro- and Nano-Scale Phenomena Responsible for the Blood Oxygenation Level Dependent (BOLD) Effect. The oxygenated red blood cell (left) has oxygenated hemoglobin, which is diamagnetic due to electrons in hemoglobin iron being bound to oxygen. Because it is diamagnetic, the oxygenated red blood cell produces a much smaller local magnetic field as compared to the paramagnetic deoxygenated hemoglobin, represented on the right. The spins of water molecule hydrogen nuclei are perturbed by the large field from deoxygenated hemoglobin, and therefore produce a lower MRI signal as compared to the water molecules surrounding the red blood cell on the left. Oxygenated hemoglobin and deoxygenated hemoglobin correspond to arterial and venous blood respectively, and therefore these differences in signal can be used to measure oxygen saturation, and rapid changes in bloodflow.

T2-Relaxation-Under-Spin-Tagging (TRUST)

TRUST is a method for estimating whole-brain oxygen extraction fraction, a biomarker for cerebrovascular disease⁴⁹, using a calibrated model relating T_2 , hematocrit, and blood oxygenation status^{69,70}. The TRUST pulse sequence is shown in **Figure 6**. A spin labeling

RF pulse is implemented to label cerebral venous blood, and a T2-weighting module, with a duration called the effective echo time (eTE) applies a T2-weighting. This T2-weighting module is a rapid chain of 180-degree pulses following a 90-degree excitation pulse. The time between each 180-degree pulse is called the τ_{CPMG} , which has been set to 10ms after determining that



this value gives the closest estimates to a true T₂ value from TRUST⁷⁰. The superior sagittal sinus (SSS) is the main vein that drains the brain after blood has circulated through the capillaries, and is typically where venous oxygenation is measured to determine cerebral oxygen consumption⁷⁰. After a post-label delay, that cerebral venous blood is imaged in the SSS, with a slice perpendicular to the SSS. Varied eTE values in the T₂-weighting module give a T₂ decay curve. This T₂ decay value is then input to an empirical model, which relates T₂, hematocrit, and blood oxygen saturation to calculate in-vivo venous blood oxygen saturation in the SSS. Thus, TRUST can be used to calculate whole-brain venous oxygen saturation (Y_v). Where Y_a is the arterial oxygen saturation, measured via pulse-oximetry, whole-brain OEF can be calculated from TRUST using the following equation.

$$OEF = \frac{Y_a - Y_v}{Y_a} \quad (15)$$

The signal in the SSS from a whole-brain TRUST measurement is⁶⁹:

$$S_{blood,label} = \left(1 - 2 \cdot e^{-\frac{(T1 - eTE)}{T1b}}\right) \cdot e^{-\frac{eTE}{T2b}} \cdot e^{-\frac{TE}{T2b^*}} \quad (16)$$

$$S_{blood,control} = e^{-\frac{eTE}{T2b}} \cdot e^{-TE/T2b^*} \quad (17)$$

By taking the difference of the control and label images, we find:

$$\Delta S = S_o \cdot e^{eTE \cdot C} \quad (18)$$

Where $S_o = 2 \cdot e^{-\frac{TI}{T_{1b}} - \frac{TE}{T_{2b}^*}}$ and $C = \frac{1}{T_{1b}} - \frac{1}{T_{2b}}$. We can fit for C and calculate T_{2b} after calculating T_{1b} from hematocrit⁶⁷.

To measure OEF, we must first collect Y_a and Y_v values for the brain. Arterial oxygen saturation is regionally invariant in a patient, and is typically 95-100%. Because of this, pulse-oximetry on the finger is sufficient for determining Y_a in the brain. However, venous oxygenation is variable depending on blood supply and metabolic needs of the region of interest⁷¹. Using MRI, we can measure venous blood T_2 in the SSS and calculate oxygenation with a calibrated relationship between T_2 , hematocrit, and oxygenation. There are two primary methods for measuring cerebral OEF with MRI, TRUST and the asymmetric spin echo described below. TRUST has the advantage of being highly reproducible in its estimation of T_2 , with its primary limitation being that it does not provide spatial information regarding OEF, and therefore gives a whole-brain estimate. TRUST also has the limitation of being dependent on a calibrated model, which is currently contentious, however ASE also suffers from limitations regarding its model.

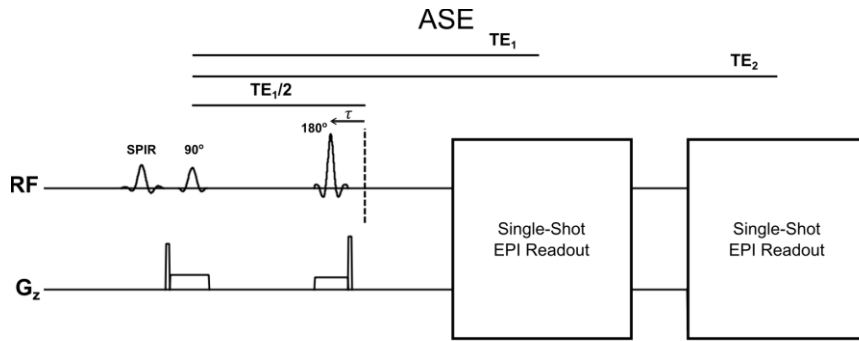


Figure 7. Conventional Asymmetric Spin Echo (ASE) Pulse Sequence. This pulse sequence is similar to a simple spin echo, however the refocusing pulse is shifted from the center point by a value τ . This shifting induces R_2' weighting, which for multiple values of τ can be fit to calculate oxygen extraction fraction and venous cerebral blood volume.

Asymmetric Spin Echo (ASE)

Susceptibility methods, namely ASE, have shown promise for measurement of OEF⁷²⁻⁷⁵. ASE uses a spin-echo sequence with the refocusing pulse shifted from $TE/2$ by a value called τ , the ASE pulse sequence is shown in **Figure 7**. This shifting imparts an R_2' weighting on the image, which can be input to a model of R_2' , hematocrit, OEF, and cerebral blood volume to fit quantitative MRI maps of OEF. Compared to TRUST, ASE has the benefit of providing topographical maps of OEF rather than a whole brain mean value. However, the susceptibility model to which ASE data is fit is sensitive to several assumptions. The model assumes

randomly oriented blood vessels, which is not satisfied in all regions of the brain, such as where vessels drain into large veins. Additionally, the model is exclusively a tissue model, so any cerebral spinal fluid (CSF) contamination ruins data from that voxel. Also, the model assumes that all susceptibility effects are from deoxygenation blood, however the brain has other sources of susceptibility particularly iron concentrations, which will vary by brain region. Diffusion effects are also assumed to be negligible, as the model is a tissue model in the static dephasing regime, however simulations have suggested that diffusion effect contributions to ASE measured parameters may not be negligible⁷⁶. The fourth chapter of this work involves the development of new ASE methods to address these challenges by making modifications to the ASE pulse sequence, which help to compensate for these limitations of ASE. If accuracy and reproducibility of ASE are improved, this sequence may help to integrate OEF into standard stroke screening, and increase the rate of early stroke risk detection. ASE has two primary benefits, first that it provides a topographical map of hemometabolic parameters, and second that it can be used to estimate multiple parameters. However, the limitations described earlier currently confound the widespread adoption of ASE.

BOLD Reactivity Imaging

The implementation of BOLD MRI relies on the BOLD effect. The BOLD effect is the name of the phenomenon where MRI signal increases in a brain region upon activation. When neurons are activated, oxygen is consumed. However, to compensate for this oxygen consumption, arterioles dilate and oxygenated blood flows into the tissue, flushing away the deoxygenated, diamagnetic venous blood. This removal of diamagnetic blood causes a reduction in susceptibility dephasing effects, and corresponding increases in MRI signal, especially T_2^* -weighted signal, which is highly sensitive to susceptibility effects. By using rapid acquisition (approximately 2 second T_R) with T_2^* -weighted gradient echo sequences, neuronal activation can be measured, though approximately, by BOLD MRI. BOLD signal however is also affected by outside effects such as cerebral blood flow, cerebral blood volume, blood oxygen saturation, and unaccounted for susceptibility effects such as iron concentrations and air-tissue interfaces⁷⁷. By measuring the magnitude of signal change in response to stimuli, as well as delay in that response, maximum CVR and CVR delay can be calculated from BOLD imaging. Applications outside of this research use stimuli such as finger tapping, visual stimuli, or even resting-state acquisitions to measure neuronal activation in the brain. BOLD is unique in its ability to measure reactivity and functional information, however it suffers from several

limitations. These limitations include multiple signal sources, as described previously, as well as a lack of standardization of BOLD protocol.

1.5 Improving Measurement of Cerebral Metabolism for Clinical Applications

Stroke occurs when blood supply to tissue is insufficient. A normal blood flow in healthy grey matter is 55 ± 6 mL/100g/min⁷⁸, and rough estimates of thresholds for tissue functioning have been identified with reversible tissue damage beginning at 20 mL/100g/min, and 10 mL/100g/min for irreversible tissue damage⁷⁹. However, in reality the damage to tissue from inadequate blood supply is dependent on many factors, and the thresholds for neurological damage are less clear. These factors include duration of blood supply restriction, delay in tissue response to metabolic stress, the magnitude of response to metabolic stress, cerebral blood volume, and how severely blood flow is restricted. These tissue parameters can be adjusted on a tissue level to maintain cerebral metabolism, typically represented by the rate of oxygen metabolism, which should remain around 2.0 ± 0.6 mL/100g/min. As a result of the complexity of this system, wide ranges of values are observed in tissue which went on to develop infarcts and that which did not⁷⁹. While CBF and OEF measurements give baseline values for these parameters, CVR tells us how tissue will respond to stress in the future. An understanding of cerebral metabolism can improve our ability to understand tissue risk for stroke as well as best treatment options. The MRI methods ASL and BOLD, described in the previous section, have improved our ability to monitor hemodynamic impairment in patients with cerebrovascular disease through non-invasive measurement of CBF and CVR. This functional hemodynamic information has been used in acute^{80, 81} and chronic^{82, 83} stages of cerebrovascular disease to aid in diagnosis, as well as in surveillance imaging to evaluate response to intervention^{19, 84}. OEF measures are promising, though are less frequently considered in clinical decisions due to very limited access to techniques for measuring it. To understand how these physiological parameters are used in a clinical setting, this section describes CBF, CVR, and OEF, as well as how they are measured, interpreted, and what may improve their usefulness, in further detail.

1.5.1 Oxygen Extraction Fraction (OEF)

According to **Equation 1**⁸⁵, if CBF decreases, as it tends to in cerebrovascular disease, the brain tissue must extract more oxygen per volume blood to satisfy metabolic requirements and maintain CMRO₂. Because of this, elevations in OEF are indicative of a potential imbalance

in oxygen delivered to oxygen consumed, as has been validated previously where regional elevation in OEF has been demonstrated with PET imaging in patients with regional cerebrovascular impairment⁸⁶. OEF is elevated in patients with impaired vasculature, demonstrated in Watchmaker et al. where healthy TRUST measured OEF was reported with an interquartile range of 0.29-0.38, and moyamoya OEF was 0.38-0.45⁸⁷. The gold standard OEF measure is O-15 PET; however, PET is invasive and requires an on-site cyclotron for production of radiolabeled oxygen. For these reasons, O-15 PET measurement of OEF is infrequently employed as an indicator of cerebrovascular impairment. TRUST has been developed for measuring OEF, and has high reproducibility⁶⁹. However, TRUST provides exclusively whole-brain measures and the calculation of OEF from TRUST-measured T_2 requires a calibrated curve, which is contested^{70, 88}. The ASE sequence will allow for regional measurements of OEF. ASE consistently under-estimates OEF and over-estimates CBV, and therefore improvements on accessible methods for reliable and regional OEF measurement are needed to allow its application in clinical practice.

1.5.2 Cerebrovascular Reactivity (CVR)

CVR indicates the effectiveness of vascular response to an increase in metabolic demand⁸⁹. CVR is often acquired with BOLD contrast and a respiratory challenge. By measuring the time delay and magnitude of maximum BOLD signal following the respiratory stimulus, CVR measurements indicate effectiveness of vascular response and cerebrovascular reserve⁹. Delays in and limited magnitude of vascular response, indicate possible impairment in blood arrival time, function of smooth muscle, or elasticity of arterioles⁹. These properties inform on how tissue will respond to stress, and therefore make CVR a sensitive metric of cerebrovascular impairment in moyamoya and other cerebrovascular diseases.

Vascular stimuli for reactivity studies are vasodilatory, in that they cause relaxation of arteriolar smooth muscle, increasing CBF and CBV locally. These stimuli can be oral, respiratory, or endogenous. Respective examples of these are the carbonic anhydrase inhibitor acetazolamide⁹⁰, mild hypercapnia induced by inhaling an air mixture containing 5% CO_2 ¹³, and breath holds⁹¹. Acetazolamide cannot be modulated down after a dose has been given, additionally there are dosage concerns when applying acetazolamide¹. Breath holds, while least invasive, can present challenges associated with patient compliance. Respiratory stimuli however, are minimally invasive, and easily modulated. However, there are different choices in selection of gas mixtures for vasodilatory stimuli. Two common choices are hypercapnic

hyperoxia (i.e. carbogen, 95% O₂ 5% CO₂) and hypercapnic normoxia (95% room air mixture 5% CO₂). There is some controversy in selection of these gasses, due to the fact that hyperoxia in carbogen administration leads to small increases in capillary and venous oxyhemoglobin¹³, which results in increased measurements of CVR due to hyperoxia rather than true CVR. Additionally, it is possible that the Haldane effect⁹², in which CO₂ binds to hemoglobin competitively with O₂, may affect measured CVR parameters when utilizing carbogen as a stimulus. However, vascular responses from hypercapnic hyperoxia and hypercapnic normoxia are correlated (p<0.05)¹³, and either stimulus is acceptable for reactivity studies. CVR measurements are generally safe, however vasoactive stimuli can make the participant feel breathless. They can also influence cerebral metabolism slightly, and therefore are typically performed under medical supervision in case of a cerebrovascular event.

On CVR-weighted BOLD-MRI maps, delays in vascular compliance can manifest as apparent negative signal or underestimation of CVR on statistical analysis, due to misidentification of baseline BOLD signal^{9, 50, 93, 94}. These artifacts are fundamental, as they preclude accurate quantitative assessment of hemodynamic parameters in one of the most obvious applications, cerebrovascular disease. In these cases, more advanced methods, which measure both maximum CVR (as opposed to baseline CVR) and CVR delay may help to extract time delay information and help to improve interpretability of CVR images. Additionally, application procedure of CVR, including best practice for stimulus delivery as well as processing technique, is not standardized.

CVR measures have demonstrated utility in identifying cerebrovascular reserve in patients at high risk for stroke⁹⁵⁻⁹⁷, and give information beyond baseline measurements of metabolism. CVR measurements inform on how a participant is likely to respond to cerebrovascular challenge in the future, and is therefore a promising marker for stroke risk. To increase the utility of CVR parameters, interpretability of CVR in cases of cerebrovascular disease must be expanded. This may be achieved with specialized analysis techniques, and through the standardization of BOLD protocols.

1.5.3 Cerebral Blood Flow

Gold standard CBF is calculated from time varying concentration of intravenously administered contrast agents in CT, PET, or MRI, however these contrast agents are invasive and PET methods require an on-site cyclotron. In MRI, the use of contrast agents may become unnecessary due to the ASL pulse sequence, which is non-invasive and utilizes an endogenous

label for perfusion signal ⁶³. The ASL pulse sequence labels arterial blood water with an RF pulse or series of pulses. The arterial blood water acts as an endogenous contrast agent, allowing for CBF measurements to be taken non-invasively. Though contrast-based methods are the gold standard, ASL measurements have improved by accounting for multiple compartments ⁹⁸, or fine-tuning parameters like label location and flip angle based on velocity measurements ^{99, 100}. In pCASL, labeling efficiency is a function of arterial flow velocity, which is fast and asymmetric in patients with flow-limiting stenosis ¹⁰¹. This can lead to error in CBF estimation. By modulating pCASL pulse sequence parameters with vessel encoding on a patient-specific level, we can improve labeling efficiency and accuracy of CBF measurement in patients with moyamoya disease.

CBF measurement with MRI is a promising and non-invasive alternative to contrast-based perfusion methods, and have also demonstrated utility in patient populations with cerebrovascular and neurological conditions^{46, 54, 102}. However, complications arise when measuring CBF under conditions of cerebral ischemia and arterial steno-occlusion. Blood transit through the arterial system and associated blood arrival times may be lengthened, which can manifest as image artifacts on CBF maps. For instance, delayed blood arrival on ASL-MRI can manifest as signal voids in extreme cases, or hyperintense endovascular signal in more modest cases, owing to labeled blood water that remains in the arterial tree prior to exchange with tissue water^{97, 102}. This is the case in moyamoya, and the relationships between ASL and moyamoya physiology must be better characterized before ASL can be implemented more regularly in clinical practice. ASL improvements have been made by interpreting signal artifacts as a source of contrast for underlying physiology, as well as through modifications to ASL implementation based on the unique physiology found in cerebrovascular disease.

1.6 MRI Processing and Machine Learning Approaches

1.6.1 Image Coregistration

One technique that is common to MRI image analysis is image coregistration¹⁰³. Coregistration refers to the process by which two images in different resolution and spatial orientation are aligned with one another, and can be implemented by either linear or non-linear transformations. In this work, small sub-structures of the brain are not investigated in great detail, and therefore coregistrations will be performed using linear registration. This allows for uniform comparison of different patient scans, so differences between groups can be compared.

An alternative to coregistration is to segment images, such that values from regions of interest are extracted. Coregistration has the benefit of allowing images to be compared visually in a similar space, however it is possible that coregistration may alter the quantitative values estimated from an image, and also the choice of coregistration technique will affect values as well. Extraction also depends on technique, but may impart less distortion of quantitative measurements compared to coregistration. Both techniques have advantages and disadvantages, however in this work, coregistration is implemented so as to allow for simpler visual comparison between images, some of these comparisons are displayed in figures.

1.6.2 Machine Learning Approaches

Machine learning is a set of techniques in which algorithms are developed to improve their performance at a given task when iterating over appropriate training data. For example, artificial neural networks (ANNs), logistic regression models, and support vector machines (SVMs) are supervised and unsupervised learning techniques that have shown success in classification of medical imaging data^{47, 104, 105}. The choice of technique depends on the specific task being addressed, as well as what resources and data are available for developing and training the algorithm. Supervised learning is a branch of machine learning in which the algorithm is provided with training data including inputs and desired outputs. Supervised learning algorithms identify patterns in training data, allowing for subsequent identification of outputs for new data.

While machine learning approaches have grown in acceptance and popularity, especially the convolutional neural network (CNN) which is well suited for extracting features from images, challenges exist for further adoption of these algorithms. For example, real-world data is complex, and creation of uniform training data is difficult. One component of addressing this challenge is the development of techniques to train algorithms under conditions of missing data. Two promising techniques are data deletion and imputation, which are still being tested in real world applications¹⁰⁶. One challenge more specific to medical imaging data is the fact that typically, 2D CNNs are implemented in 3D spaces. This leads to challenges that are being addressed by the development of models with more effectively integrate 3D information^{107, 108}. Another important development in data processing is to improve consideration of multiple clinical data elements (CDEs) in processing, rather than processing imaging modalities and demographic information separately. CDEs can include different MRI contrasts such as structural imaging and diffusion weighted imaging, different imaging modalities such as MRI and

CT, as well as demographic factors like race or age, all of which can be integrated using processing networks and principle component analysis approaches^{106, 109}.

The work in this dissertation utilizes supervised learning techniques, which have existed longer than their unsupervised learning counterparts and are a robust choice for processing small data sets. Supervised learning techniques have shown promise in a wide range of classification problems, including identification of disease in medical images^{47, 104, 110}. By analyzing medical images to identify patient disease, supervised learning algorithms may be able to aid radiologists in their diagnoses or help to identify treatment options in medical facilities with limited training in medical image interpretation. Further development of machine learning techniques in clinical applications will provide greater indication of what might be necessary to implement supervised learning techniques routinely in a clinical setting, and which diseases and applications might be best suited for a supervised learning approach.

Chapter 2: Classifying Intracranial Stenosis Disease Severity from Functional MRI Data using Machine Learning

2.1 Introduction

While functional imaging with MRI is growing in popularity, several key factors preclude widespread adoption of these methods. One important limitation is that functional imaging typically performs best under normal physiological conditions, and the unique blood flow properties of cerebrovascular diseases complicate image interpretation. However, the image artifacts that result from abnormal physiology may convey information on that same physiology. Therefore, it is possible that artifacts, which would typically be considered to confound image interpretation, can be viewed instead as a source of contrast. In this chapter, we use machine learning techniques to interpret functional images in moyamoya in an attempt to use artifacts that result from long arterial transit times and delays in reactivity as contrast for moyamoya severity.

Under conditions of cerebral ischemia and arterial steno-occlusion, blood transit through the arterial system and associated blood arrival times may be lengthened, which can manifest as image artifacts on CBF and CVR-weighted maps. For instance, delayed blood arrival on ASL-MRI can manifest as signal voids in extreme cases, or hyperintense endovascular signal in more modest cases, owing to labeled blood water that remains in the arterial tree prior to exchange with tissue water in the capillaries^{97, 102}. On CVR-weighted BOLD-MRI maps, delays in vascular compliance can manifest as apparent negative signal or underestimation of CVR on

statistical analysis, due to misidentification of baseline BOLD signal^{9, 50, 93, 94}. These artifacts are fundamental, as they preclude accurate quantitative assessment of hemodynamic parameters in cerebrovascular disease. We investigated whether emerging machine learning approaches could exploit contrast from these apparent artifacts as novel contrast sources to distinguish flow territories with vs. without clinical indicators of hemodynamic impairment in patients with moyamoya.

Moyamoya is an intracranial arterial steno-occlusive disease affecting the supraclinoid internal carotid artery (ICA) and its proximal branches, which leads to delayed blood arrival times²¹, delayed reactivity timing⁹, and development of compensatory collateral vessels. Moyamoya is clinically relevant as it incurs a seven-fold increase in stroke risk compared to age- and race-matched adults⁴⁴ and treatment regimens, which may comprise either medical management or surgical revascularization, have not been established by randomized clinical trials. The current standard for identifying disease severity in moyamoya is stenosis grading of major intracranial vessels with catheter angiography, however this procedure carries perioperative risk and exposes patients to ionizing radiation, and for these reasons is suboptimal for surveillance.

Machine-learning techniques, which have been successfully applied in both anatomical^{111, 112} and functional imaging^{47, 104}, should have relevance for identifying functional hemodynamic biomarkers in patients with moyamoya. Machine learning algorithms include but are not limited to artificial neural networks (ANN)^{111, 113}, random forests¹¹⁴, decision trees¹¹⁵, and support vector machines (SVM)^{47, 104, 116}. To investigate the possibility of analyzing contrasts in functional hemodynamic maps with machine learning techniques, we applied SVMs to evaluate multiple functional imaging contrasts to discriminate hemispheres with vs. without known hemodynamic impairment.

We hypothesized that transit time related artifacts in hemodynamic images, such as endovascular signal on ASL-MRI and reactivity delays on CVR-weighted MRI (CVRw-MRI), can classify brain parenchyma supplied by angiographically-confirmed stenotic vessels. To test this hypothesis, we sequentially acquired catheter angiography, anatomical imaging, and ASL- and BOLD-MRI in a cohort of moyamoya patients, and evaluated discriminatory capacity of hemodynamic imaging methods for hemispheres supplied by steno-occlusive vessels using machine learning approaches. As an exploratory analysis, we used similar methods to identify variables indicative of new infarct risk in tissue. Finally, we discuss potential and remaining limitations to machine learning algorithms in this cohort, as well as potential relevance of these findings to more common atherosclerotic cerebrovascular disease patients.

2.2 Materials and Methods

2.2.1 Participant demographics

All participants provided informed, written consent, and all components of the study were approved by the Vanderbilt University Institutional Review Board. Criteria for inclusion were adult patients with a clinical diagnosis of moyamoya confirmed by catheter angiography, identified from the Vanderbilt Neurology and Neurosurgery services between January 27, 2011 and January 19, 2018. Hemispheres with prior surgical revascularization (direct or indirect) were excluded. Healthy controls were recruited if they had no prior neurological condition and no current cerebrovascular disease confirmed by vascular and anatomical imaging at the time of enrollment. Demographic information is shown in **Table 1**. All components of this study were performed in compliance with the Declaration of Helsinki of 1975 (and as revised in 1983), Health Insurance Portability and Accountability Act, and all protocols were approved by the Vanderbilt University Institutional Review Board (IRB Study 140915).

2.2.2 Acquisition

Data were acquired using a 3.0T MRI scanner (Philips, Best, The Netherlands) with body coil RF transmission and 16-channel SENSE-array neurovascular coil reception.

Anatomical imaging. MRI acquisition included T_2 -weighted (TR/TE=3000/80 ms; resolution=0.6x0.6x4.0 mm³), T_2 -weighted axial fluid-attenuated inversion recovery (FLAIR) (turbo inversion recovery; TR/TI/TE=11000/2800/120 ms; spatial resolution=0.9x1.1x3.0 mm), and T_1 -weighted (magnetization-prepared-rapid-gradient-echo; spatial resolution=1.0x1.0x1.0 mm³, 3D turbo field echo; TR/TE=8.2/3.7 ms) scans.

	Controls	All Patients
N (count)	10	53
Age (years)	29 ± 4.1	45 ± 14.2
Sex	60% F	81% F
Race (Black)	0%	38%
Race (Asian)	0%	9%
Race (White)	100%	53%
Diabetes	0%	36%
Smoking	0%	25%
Stenosis Location		
ICA	none	33 Right, 30 Left
MCA	none	31 Right, 25 Left
ACA	none	18 Right, 10 Left
PCA	none	4 Right, 3 Left

Table 1. Demographic information for Moyamoya Participants in Chapter 2. Continuous variables are shown as mean ± one standard deviation. Categorical variables are shown as percentages.

Catheter angiography. Clinically-indicated digital subtraction angiography (DSA) was performed with a Philips Allura Xper biplane neuro X-ray system. Data were collected per clinical indication with manual catheter injection of contrast to the common carotid arteries or ICAs and vertebral arteries (four injections per patient)¹¹⁷.

Arterial spin labeling. Quantitative CBF measurements were obtained with a 2D multi-slice (slices=17; spatial resolution=3x3x7 mm³) pseudo-continuous ASL (pCASL) sequence (TR/TE=4200/12.5 ms)¹¹⁸. Due to the seven-year duration of this study, pCASL parameters were similar but varied slightly: protocol A (label duration=1600 ms; label delay=1525 ms) and pCASL protocol B (label duration=1650 ms; label delay=1800 ms). These post-label delay values are common for 3.0T ASL studies, but are shorter than expected circulation times in many moyamoya patients^{102, 117}, which may lead to endovascular signal artifacts that are of interest to this study. The potential influence of multiple pCASL protocols is addressed in the *Discussion*.

CVR-weighted BOLD imaging. CVR-weighted measurements were obtained during BOLD imaging (TR/TE=2000/30 ms; spatial resolution 2.7x2.7x3.5 mm³; 360 dynamics) with a vasodilatory hypercapnic-hyperoxic stimulus (95% O₂, 5% CO₂). The stimulus paradigm consisted of 180 seconds hypercapnic-hyperoxia interleaved with 180 seconds normocapnic-normoxia repeated once. This stimulus has been investigated previously for reproducibility and sensitivity to lateralizing disease in the moyamoya patient population^{13, 119}. Differences between stimuli are addressed in the *Discussion*. Throughout the scan, respiratory rate, blood pressure, end-tidal CO₂, arterial oxygen saturation, and heart rate were monitored (Medtronic, Dublin, Ireland).

2.2.3 Analysis

Anatomical imaging and catheter angiography. T₂-weighted, T₂-weighted FLAIR, and T₁-weighted MRI were used to record prior infarcts by a board-certified radiologist (LTD) who was blinded to other hemodynamic and functional imaging findings. Moyamoya patient hemispheres were separated into groups that were supplied by either a severely stenotic vessel or mildly stenotic vessels, in which Stenting versus Aggressive Medical Management in Patients at-Risk for stroke with Intracranial Stenosis (SAMMPRIS)⁶ criteria were used. More specifically, a hemisphere with severe stenosis was supplied by a major intracranial vessel (first segment of

middle cerebral artery, posterior cerebral artery, or anterior cerebral artery; intracranial ICA; or basilar artery) with $\geq 70\%$ stenosis, and mild stenosis was a hemisphere with all supplying vessels $< 70\%$. Although stenosis of smaller and more distal vessels is possible, vascular stenosis of these more distal segments is difficult to quantify even on catheter angiography, and more importantly, the spatial extent of impairment from these vessels will be more focal and potentially variable. Here, as a first-principle study, and to ensure that the regions considered met accepted clinical criteria for impairment as recommended by prior trials⁶, we focused on stenosis in major intracranial vessels as defined above. We define stenosis $< 70\%$ as mildly impaired, as moyamoya is a bilateral condition and stenosis of smaller vessels not apparent on angiography is likely.

Arterial spin labeling. ASL preprocessing included affine motion correction¹²⁰, spatial smoothing (full-width-half-maximum=3 mm), slice-time correction, control and label pair-wise subtraction, and dynamic averaging (protocol A: measurements=27; protocol B: measurements=20). Additionally, T_1 -weighted images served as an intermediate template to register the control images from ASL acquisition to Montreal Neurological Institute (MNI) space using linear co-registration (FMRIB's Linear Image Registration Tool; FLIRT) with 12 degrees of freedom. Images were co-registered to ensure that comparisons could be made between hemispheres while keeping proportions of gray and white matter approximately consistent in volumes of interest, and so that anterior and posterior flow territories could be identified consistently between participants. The transformation matrix was recorded and applied to the quantitative ASL difference magnetization map. Quantitative CBF maps were calculated according to a two-compartment model applied to the processed difference magnetization ($M_{control} - M_{label}$), using the fmincon constrained non-linear optimization function in Matlab^{65, 66}:

$$M_{control} - M_{label} = \frac{2M_0 f \alpha}{\lambda} \cdot \frac{e^{-\delta R_{1a}}}{R_{1app}} \left[e^{(\delta-w) \cdot R_{1app}} - e^{(\delta-\tau-w) \cdot R_{1app}} \right] \quad (19)$$

where M_{label} is the magnetization of the labeled pCASL image, $M_{control}$ is the magnetization of the unlabeled control pCASL image, M_0 is equilibrium magnetization, f is CBF in mL/g/s, $\alpha = 0.85$ is pCASL labeling efficiency, $\lambda = 0.9 \text{ ml/g}$ is the whole-brain blood-brain partition coefficient, $\delta = 1.5s$ is the tissue transit time, $R_{1a} = 0.59 \text{ s}^{-1}$ is the longitudinal relaxation rate for oxygenated macrovascular arterial blood water at $3.0T$ ⁶⁷, R_{1app} is the apparent longitudinal

relaxation rate of perfused tissue ($R_{1app} = R_{1,Tissue} + \frac{f}{\lambda}$), $R_{1,Tissue} = 0.77 \text{ s}^{-1}$, w is the pCASL post-label delay time, and τ is the pCASL labeling duration. CBF is converted to units of mL/100g/min by multiplying by a factor of 6000. Note that R_{1app} contains a dependence on f , which makes the minimization routine required. We chose to use a more complete form of the kinetic model compared with a recently-proposed simplified model⁶³, since the simplified model explicitly assumes that all labeled blood water spins are delivered to tissue at the post-labeling delay time and also that the labeled spin relaxation is only due to blood water R_1 , whereas tissue water R_1 also contributes. In practice, these assumptions are not expected to influence findings in a significant way, and the above model also makes approximations regarding expected blood and tissue transit times; note that in this study the different models will only scale the endovascular signal slightly differently. However, as the purpose of this study was specifically to consider contrast in the context of endovascular artifacts, we used the more complete model to reduce the number of assumptions that were fundamentally in conflict with our primary hypothesis. The CBF images resulting from this approach are expected to have endovascular artifacts, which can be exploited with machine learning analysis as an indicator of arterial collateralization and long blood arrival times^{121, 122}.

CVR-weighted BOLD imaging. BOLD preprocessing included motion correction and spatial smoothing, similar to ASL preprocessing, and images were corrected for slice-timing using the FSL software, FEAT¹⁰³. Following affine motion

correction, both BOLD and ASL images were qualitatively evaluated for residual motion effects,

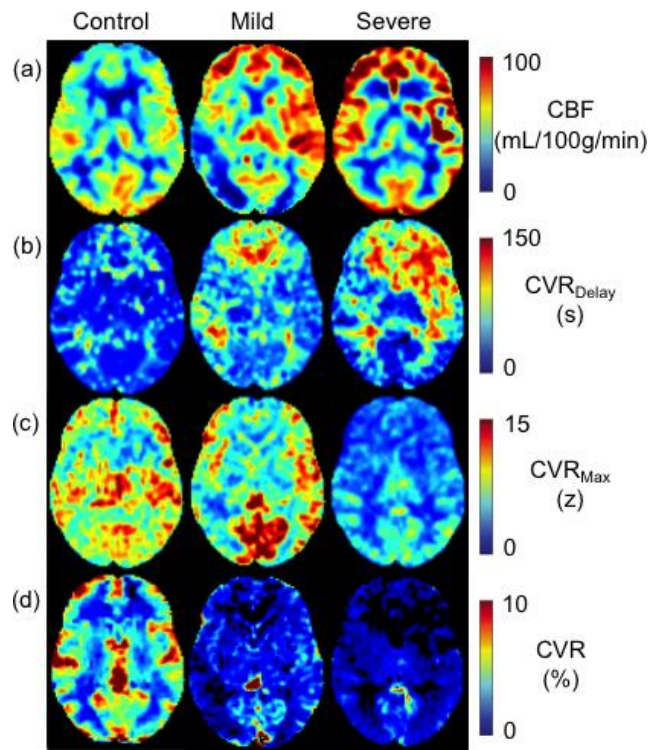


Figure 8. Representative Images for Cerebral Metabolic Parameter Maps at Three Stages of Moyamoya Impairment. Representative images for each physiological parameter (rows) and patient group (columns) used to test the primary hypothesis in this study. The mild stenosis moyamoya patient is a 48 year old female with stenosis in the right M1 segment of the MCA and left supraclinoid ICA. The severe stenosis patient is a 23 year old female with stenosis bilaterally in both M1 MCA and supraclinoid ICA segments. With increasing arterial steno-occlusion, CBF-weighted data demonstrate heterogeneous hyperintense endovascular signal, CVR_{Delay} lengthening, and CVR reduction.

manifesting as peripheral signal hyperintensities on the ASL difference images and focal hyperintensities on the BOLD time courses, and any images with residual motion that was deemed to preclude interpretability were excluded. BOLD images were co-registered to an MNI atlas using the same techniques as described in the *Arterial spin labeling* section above. Three CVR parameters were calculated from BOLD reactivity data. First, CVR was defined as the mean BOLD signal change in response to stimulus, for which the last 60s of both 180s hypercapnic stimulus blocks (30 images per 60 seconds) were averaged to calculate a stimulus image and the last 120s of the 180s interleaved period were averaged to calculate a baseline image. The CVR map is the fractional signal change map. To analyze time-delayed vascular response to stimulus⁹, a rectangular regressor was applied to represent on and off stages of the paradigm. This regressor was advanced in time until maximum correlation between voxel time course and shifted regressor was found. Time until maximum correlation was defined as CVR_{Delay} (seconds), and the value of maximum correlation is CVR_{Max} (z-statistic between shifted regressor and voxel time course). These values are calculated on a voxel-wise basis to create CVR_{Delay} (time delay) and CVR_{Max} (maximal statistical response) maps. Representative maps are shown in **Figure 8**; all parameters are defined in **Table 2**.

2.2.4 Quantification of observables

While moyamoya is generally a bilateral condition, severity can vary regionally²⁴. Each hemisphere was separated into two regions, one approximately supplied by the ICA and another by the vertebrobasilar (VBA) arteries. These were estimated from a common flow territory map atlas calculated with vessel-encoded ASL^{123, 124}. A standard histogram and associated voxel-intensity threshold approach was applied to the T_1 -weighted atlas to estimate the fractional tissue volumes in each region.

The inputs to machine learning techniques are regional imaging and demographic information. In ICA and VBA flow territories, we calculated three standard statistical measures (i) 99th percentile (99th%), (ii) mean, and (iii) standard deviation (std) of the voxel intensities for CBF, CVR, CVR_{Delay}, and CVR_{Max} maps (**Table 2**). Owing to recent evidence suggesting that the coefficient of variation (CoV) in ASL maps has relevance for discerning important arrival time information¹²¹, spatial CoV of CBF was also calculated in both ICA and VBA flow territories according to the following equation¹²¹.

$$CBF\ CoV = \frac{CBF\ std}{CBF\ mean} \cdot 100\% \quad (20)$$

This yielded 13 imaging measures per flow territory (26 per brain hemisphere). Additionally, five demographic and risk factor variables, including age (continuous), sex (dichotomous), race (categorical: Black, Asian, or White), smoking status (dichotomous), and diabetes (dichotomous) were considered.

Parameter	Acquisition Method	Description	Unit
CBF	pCASL	Rate of blood delivery to brain tissue at physiological baseline	mL/100g/min
CBF-CoV	CBF-CoV	Ratio of CBF standard deviation to CBF mean.	Percentage
CVR	BOLD	Mean BOLD signal change in response to vasodilatory stimulus	Percentage
CVR _{Delay}	BOLD	Statistical measure of vascular response delay time (i.e., time for the regressor to become maximally correlated with the experimental data)	Seconds
CVR _{Max}	BOLD	Statistical measure of vascular response magnitude to stimulus (i.e., the z-statistic at the CVR _{Delay} time)	Z-Statistic

Table 2 Parameter Definitions in Chapter 2. Definitions of the four physiological parameters used in this study. For each parameter except CBF coefficient of variation (CoV), we calculated mean, 99th percentile, and standard deviation values in flow territories supplied by both the left and right internal carotid arteries as well as the vertebrobasilar flow territory. For CBF-CoV, only the mean value of this parameter by convention.

2.2.5 Statistical Considerations and Hypothesis Testing.

The overall goal of this work was to consider each brain hemisphere in each patient as a separate data point, and to divide these hemispheres into (i) healthy controls (control), (ii) patients with all supplying vessels with stenosis < 70% (mild), or (iii) patients with at least one supplying vessel with stenosis \geq 70% (severe). Next, we evaluated the performance of single or combinations of imaging and demographic variables using machine learning for discriminating the hemispheres by category.

For machine learning, the support vector machine (SVM) classifier algorithm was utilized. An SVM performs binary classifications by transforming the data space into a higher dimensional space using a kernel, and optimizing the position of a hyper-plane to define a boundary separating input groups¹¹⁶. SVM classifiers were trained in MATLAB using the `fitsvm` function with a radial bias function kernel and `fitsvm` default parameters, including kernel scale set to 1, box constraints set to 1, standardized data, and solving with sequential minimal optimization¹²⁵. Predictive performance was assessed with receiver operating characteristic

(ROC) analysis using the ROC area under the curve (ROCAUC). Sensitivity and specificity were recorded at the point along the ROC curve that yielded maximum Youden's index¹²⁶. Youden's index is the sum of sensitivity and specificity minus one, and is a common method used to define a threshold with optimal compromise between sensitivity and specificity^{127, 128}. For comparisons made by stenosis extent, classifiers were validated with stratified, repeated 3-fold validation, where ROC curves were averaged for each fold, and the final reported ROC was the average of all repetitions¹²⁹.

Hemispheres were grouped into one of three categories: (i) control (from healthy subjects), (ii) mild (major supplying vessels all with stenosis <70%) and (iii) severe (at least one major intracranial vessel with stenosis ≥70%). Single-variable, two-variable, and three-variable SVM classifiers were tested with all combinations of variables for each of the three group-comparisons: controls vs. mild regions, controls vs. severe regions, and mild vs. severe regions. The number of variable combinations tested is,

$$C(v, k) = \frac{v!}{k! \cdot (v - k)!} \quad (21)$$

Where C is the total number of combinations, $v=31$ is the number of variables being tested per hemisphere, and $k=1, 2, \text{ or } 3$ is the dimensionality of the SVM algorithm. A suitable number of repetitions for cross validation was determined when the ROCAUC value was found not to change by more than 0.01 for 95% of these variable combinations when the number of repetitions was doubled. Single- and two-variable classifiers were implemented with 100 repetitions, and three-variable SVMs were implemented with 200 repetitions.

The process of ranking best performing variables was by maximum ROCAUC value for the control vs. mild hemispheres as this was a more clinically meaningful and challenging criteria (e.g., compared with distinguishing control vs. severe), however ROCAUC values for other hemisphere classifications are also included.

As an exploratory analysis, hemispheres were grouped by those with vs. without new infarcts in the subgroup of patients with surveillance imaging. A similar procedure with single- and two-variable classifiers was applied to determine potential for identifying hemispheres that progressed to develop new infarcts. Here, due to a smaller sample size, a leave-one-out approach was used instead of 3-fold validation for cross validation.

While the primary focus of this study was on SVM performance, we also summarize group-wise comparisons of the input variables using two-sided p-values calculated with a

Wilcoxon rank-sum test for parameters in each of the three hemisphere groups: control vs. mild, control vs. severe, and mild vs. severe. When $p < 0.0038$ (after a correction for the 13 functional variables calculated in each flow territory) the group-wise difference was denoted as significant. This analysis was repeated in the exploratory analysis to determine group-wise effects in hemispheres that had recurrent stroke at follow up.

CBF-CoV, CBF-mean, and CBF-std were compared in separate linear regression analyses, in which the Pearson correlation coefficient (r) was used to assess correlation between variables. For presenting variables, the map used is shown first, followed by the hyphenated statistical measure and the flow territory denoted in parentheses. For example *CBF-std (ICA)* denotes the standard deviation of the CBF in the ICA territory.

2.3 Results

Sixty-six moyamoya patients were enrolled, of whom 53 patients met inclusion criteria, and 22 patients received follow-up imaging (follow-up duration= 363 ± 145 days). Eleven patients were excluded due to prior bilateral revascularization surgeries and two for incomplete or motion-corrupted data sets. Fourteen patients had only one hemisphere excluded due to unilateral revascularization surgery. *Ultimately, this study included 92 patient hemispheres from 53 moyamoya patients, and 20 control hemispheres from 10 control subjects.* Of 92 patient hemispheres, 64 were supplied by at least one flow-limiting stenotic vessel of the anterior circulation. The distribution of stenotic arteries were the intracranial segment of the ICA (33 right, 30 left), first segment of the MCA (31 right, 25 left), first segment of the ACA (18 right, 10 left), and first segment of the PCA (4 right, 3 left) (**Table 1**). Preservation of posterior circulation until late disease stages is common in moyamoya, consistent with the finding that all hemispheres had anterior vessel stenosis, but only 7.6% of hemispheres were also supplied by a severely stenotic vessel from the posterior circulation. The mild stenosis group had 20 hemispheres collected with pCASL protocol A, and 8 hemispheres collected with protocol B; the severe stenosis group had 32 hemispheres collected with pCASL protocol A and 32 hemispheres collected with protocol B. All control data were collected with pCASL protocol B.

Twenty-two patients received follow-up imaging. Five hemispheres were excluded from recurrent stroke analysis due to unilateral revascularization surgery. Six hemispheres had new infarcts and 33 hemispheres had no new infarcts at follow-up. All but one of the new infarcts occurred in anterior flow territories. Of the six hemispheres with new infarcts, two had arterial stenosis $< 70\%$ of the supplying vessels in that hemisphere and four had stenosis $\geq 70\%$. Of the 33 hemispheres without new infarcts, 11 had arterial stenosis $< 70\%$ and 22 had stenosis $\geq 70\%$.

Variable 1	Variable 2	Variable 3	Control hemispheres vs. hemispheres supplied by mildly stenotic vessel			Hemispheres supplied by mildly vs. severely stenotic vessels		
			ROC AUC	Specificity	Sensitivity	ROC AUC	Specificity	Sensitivity
Machine learning results: performance of two commonly recorded variables								
CBF-Mean (ICA)	CVR-Mean (ICA)	None	0.65	0.83	0.43	0.54	1.0	0.20
Machine learning results: three-variable performance								
CBF-std (ICA)	CBF-mean (VBA)	CVR _{Delay} -mean (VBA)	0.71	0.67	0.69	0.75	0.67	0.74
CBF-std (ICA)	CVR-mean (VBA)	CBF-CoV (ICA)	0.71	0.83	0.53	0.75	0.67	0.74
CBF-std (ICA)	CVR-mean (VBA)	CBF-CoV (VBA)	0.71	0.67	0.69	0.75	0.67	0.76
CBF-std (ICA)	CVR _{Delay} -mean (ICA)	Diabetes	0.71	0.83	0.53	0.74	0.67	0.73
CBF-std (ICA)	CVR _{Delay} -std (ICA)	CVR-mean (VBA)	0.71	0.83	0.52	0.74	0.67	0.75
CBF-std (ICA)	CVR _{Delay} -std (ICA)	Smoking	0.71	0.67	0.70	0.74	0.67	0.73
CBF-std (ICA)	CVR _{Delay} -99 th % (VBA)	CVR _{Max} -mean (VBA)	0.71	0.67	0.69	0.74	0.67	0.74
CBF-std (ICA)	CVR _{Max} -Std (ICA)	CBF-CoV (ICA)	0.71	0.83	0.52	0.74	0.67	0.74
CBF-std (ICA)	CVR _{Max} -99 th % (VBA)	CVR-mean (ICA)	0.71	0.83	0.52	0.74	0.67	0.73
Machine learning results: two-variable performance								
CBF-std (ICA)	CVR _{Delay} -mean (ICA)	None	0.70	0.83	0.52	0.75	0.67	0.75
CBF-std (ICA)	CVR _{Max} -Std (VBA)	None	0.70	0.67	0.66	0.75	0.67	0.75
CBF-std (ICA)	CBF-mean (VBA)	None	0.70	0.83	0.51	0.75	0.67	0.74
CBF-std (ICA)	CVR _{Max} -mean (ICA)	None	0.70	0.67	0.67	0.74	0.67	0.73
CBF-std (ICA)	CVR-std (ICA)	None	0.70	0.67	0.69	0.74	0.67	0.73
CBF-std (ICA)	CVR-mean (VBA)	None	0.70	0.83	0.52	0.74	0.67	0.74
Machine learning results single-variable performance								
CBF-std (ICA)	None	None	0.70	0.83	0.52	0.75	0.67	0.74

Table 3. High-Performing Functional Parameters for Predicting Moyamoya Stenosis. The highest performing variable combinations, for control vs. mildly stenotic and mildly stenotic vs. severely stenotic hemisphere SVM algorithms, in comparison to one combination of commonly measured variables (CVR-mean and CBF-mean measured in the ICA flow territory; top). Region is shown in parentheses for each variable. CBF-std (ICA) is the only single variable that displays classification with ROCAUC > 0.60 for both control vs. mild and mild vs. severe comparisons. Additionally, CBF-std (ICA) is present in all of the highest performing variable combinations. Sensitivity and specificity are reported at the point along the ROC curve with maximum Youden's index.

Mean tissue composition was calculated in each of the flow territory maps and was determined to be 64% and 70% gray matter for ICA and VBA flow territories, respectively. The same regions were used in all subjects and therefore tissue composition bias is anticipated to be similar across all subjects. This fraction of gray matter is to be expected for typical BOLD and ASL voxel dimensions of 2-7 mm as used here.

In machine learning analysis, data were input to single-variable ($C=31$ total variable combinations), two-

variable ($C=465$ total variable combinations), and three-variable ($C=4495$ total variable combinations) SVM algorithms, in which all possible combinations of variables were tested for classification performance. In single variable learning, the best performing variable was CBF-std (ICA) with ROCAUC=0.70 for control vs. mild classification and ROCAUC=0.75 for mild vs. severe classification. No other variables yielded ROCAUC>0.60 for all classifications.

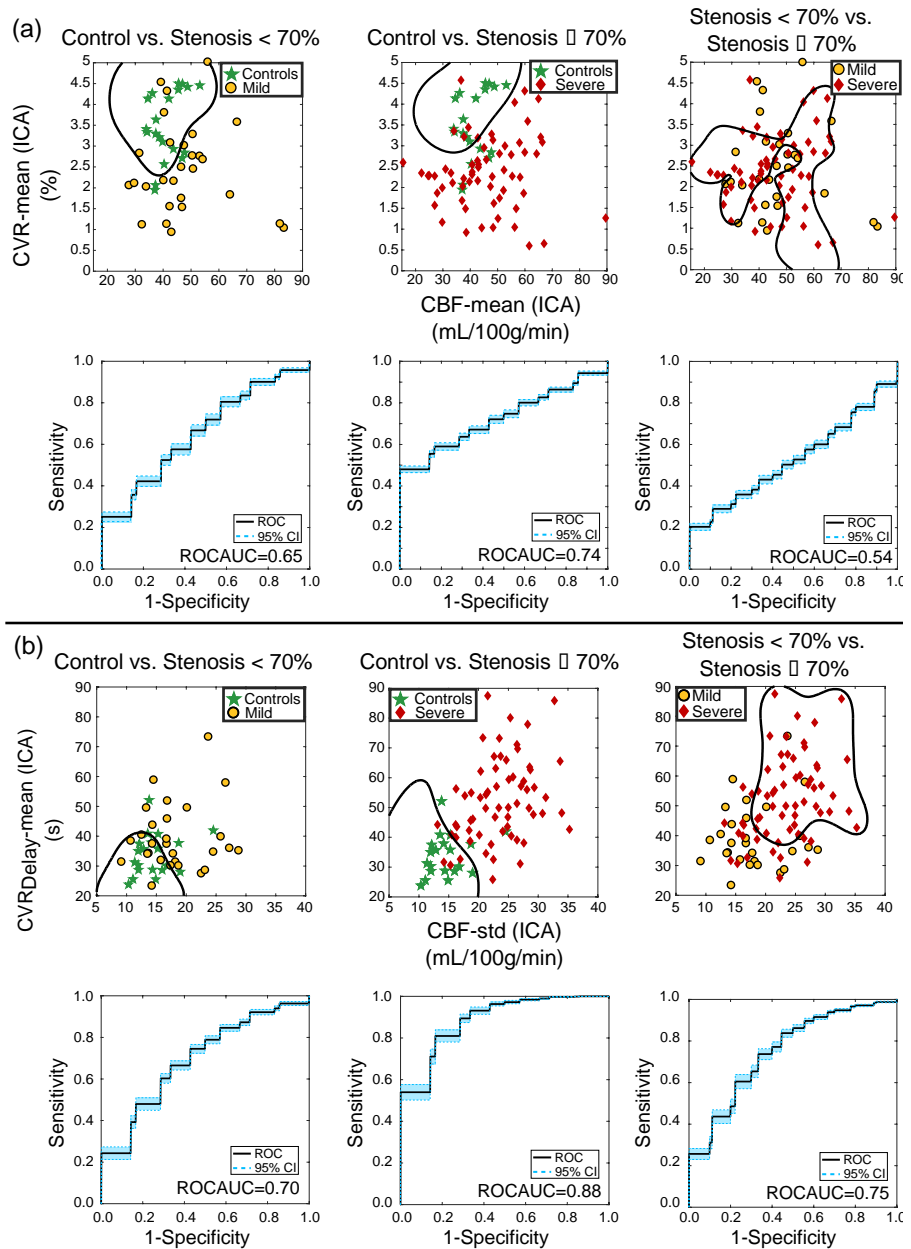


Figure 9 High-Performing Physiological Parameters for Predicting Moyamoya Stenosis Compared to Conventional Parameters in Support Vector Machines. A comparison of classification performance for variables more commonly used for identifying cerebrovascular impairment (CVR-mean and CBF-mean measured in the ICA flow territory; a) to the newly identified variables from the SVM analysis (CBF-std and CVR_{Delay}-mean in the ICA territory; b).

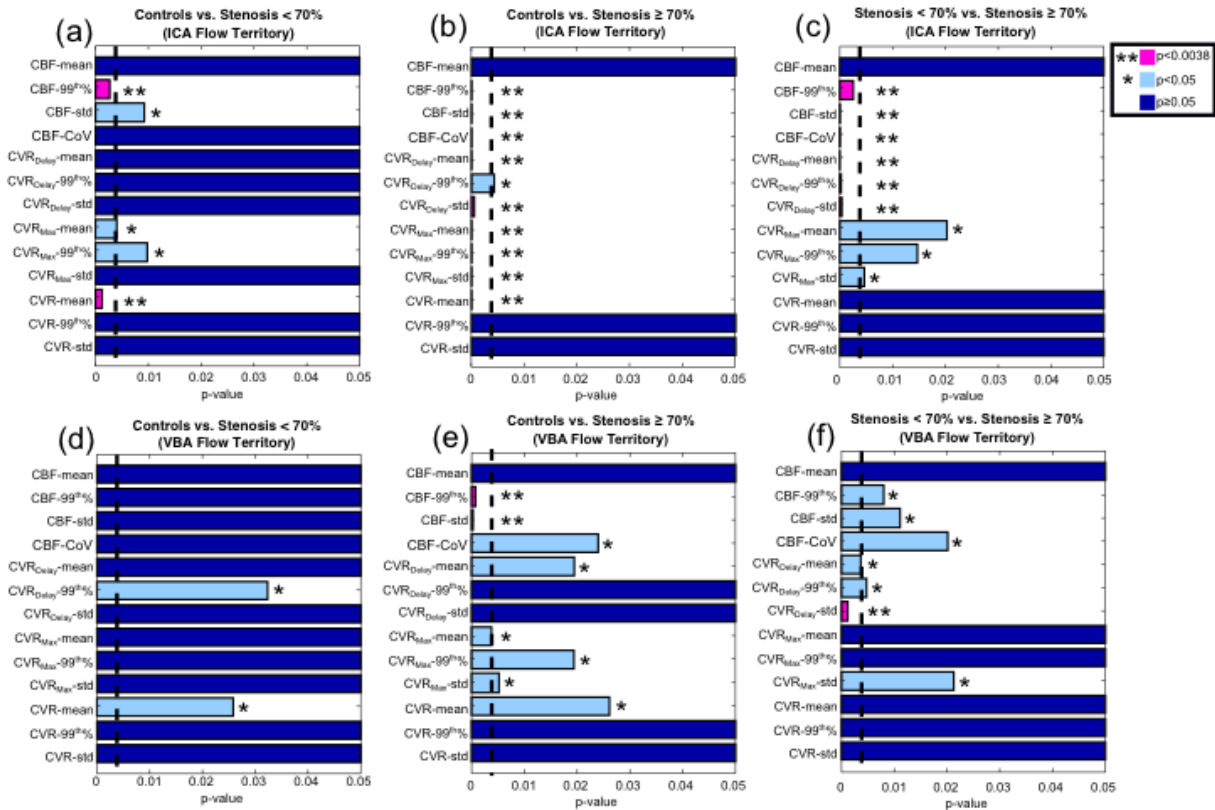


Figure 10. Group-Wise Comparisons of Physiological Parameters by Moyamoya Stenosis Group. P-values from a Wilcoxon rank-sum test for each imaging variable when comparing controls to hemispheres supplied by mildly stenotic vessels (a, d), controls to hemispheres supplied by severely stenotic vessels (c, e), and hemispheres supplied by mildly versus severely stenotic vessels (c, f). Each variable is shown for the ICA flow territory (top) and the VBA flow territory values (bottom). Variables are considered significant at or below $p=0.0038$, which includes a multiple-comparison correction accounting for 13 imaging variables.

The highest performing two and three variable classifications are shown in **Table 3**. All highest performing variable combinations contained CBF-std (ICA). Fifteen imaging variables and two demographic variables (diabetes and smoking) were identified. A high performing two-variable SVM using CBF-std (ICA) and CVR_{Delay} -mean (ICA) is displayed in **Figure 9** in comparison to a two-variable SVM using variables that are often recorded: CVR-mean (ICA) and CBF-mean (ICA). In **Figure 9**, when comparing control vs. mild hemispheres, SVM performance is similar for CBF-mean (ICA) and CVR-mean (ICA) (ROCAUC=0.65) compared to CBF-std (ICA) and CVR_{Delay} -mean (ICA) (ROCAUC=0.70). However, when classifying mild vs. severe hemispheres, CBF-mean (ICA) and CVR-mean (ICA) (ROCAUC=0.54) are outperformed by CBF-std (ICA) and CVR_{Delay} -mean (ICA) (ROCAUC=0.75).

Figure 10 summarizes all functional variables using standard Wilcoxon rank-sum analysis. In control vs. mild hemisphere comparison, two significant variables were found in the ICA territory, CBF-99th%, and CVR-mean, compared to no variables from the VBA territory. In comparisons between hemispheres supplied by mild vs. severely stenotic vessels, significance was found for six variables in the ICA flow territory: CBF-99th%, CBF-std, CBF-CoV, CVR_{Delay}-mean, CVR_{Delay}-99th%, and CVR_{Delay}-std, compared to only one from the VBA territory, CVR_{Delay}-std. **Figure 11** contains box plots comparing two commonly recorded hemodynamic variables displayed in **Figure 9** (CVR-mean and CBF-mean from the ICA flow territory) to candidate variables identified through SVM analysis from **Figure 9** (CBF-std and CVR_{Delay}-mean in the ICA flow territory). Variables identified from SVM analysis are consistent with moyamoya pathophysiology and prolonged blood arrival times.

Relationships between CBF-CoV, CBF-mean, and CBF-std from the ICA territory were investigated with linear regression to identify how these variables, which all reflect spatial properties of CBF heterogeneity and blood arrival, may be related at different stages of impairment in moyamoya disease

(**Figure 1**). CBF-std (ICA) correlated with CBF-mean (ICA) for control ($r=0.72$) and mild ($r=0.74$) hemispheres, but not in hemispheres supplied by severely stenotic vessels ($r=0.37$). The CBF-CoV (ICA) was correlated with CBF-std (ICA) in control hemispheres ($r=0.81$) and inversely with CBF-mean (ICA) in hemispheres supplied by severely stenotic vessels ($r=-0.72$). In all comparisons, significance of relationships between CBF-CoV (which comprises CBF-std and CBF-mean; **Equation 20**), CBF-std, and CBF-mean were dependent on supplying artery stenosis. Results demonstrate that CBF-CoV may be closely related to CBF-std in control

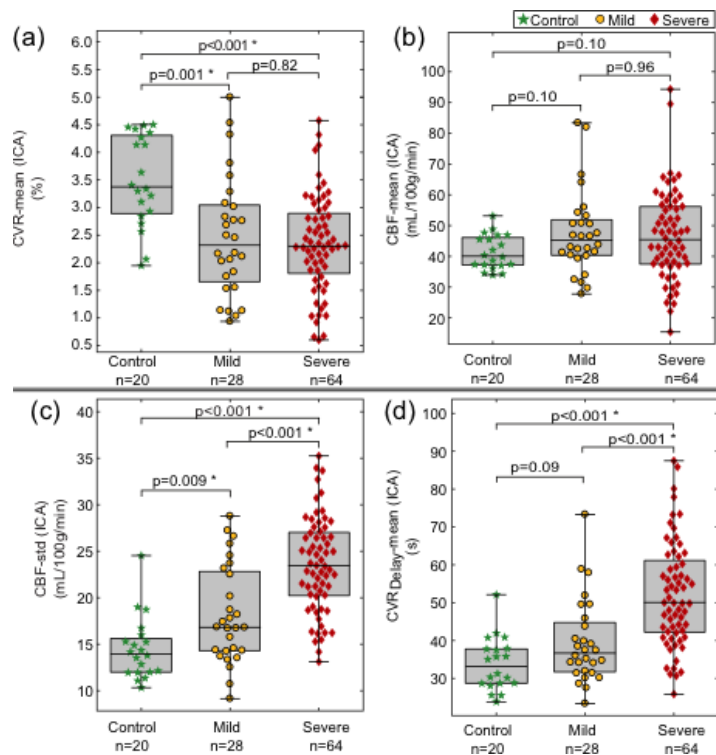


Figure 11. High-Performing and Conventional Physiological Parameters Compared Between Moyamoya Group Illustrated in Boxplots. Group-wise comparisons for variables more commonly used for identifying cerebrovascular impairment (CVR-mean and CBF-mean measured in the ICA flow territory; a, b) to that from non-conventional variables (CBF-std and CVR_{Delay}-mean in the ICA flow territory; c, d).

hemispheres and to CBF-mean in severely stenotic hemispheres, however CBF-CoV may present unique information in hemispheres supplied by mildly stenotic vessels.

As an exploratory analysis, in the subgroup of patients with follow-up imaging, we investigated abilities to distinguish hemispheres with vs. without new infarcts at follow-up using single and two-variable SVM classifiers applied to data acquired at the first time point (**Figure 12**). In single-variable machine learning analysis, the four highest performing variables were CVR_{Delay}-mean (VBA) (ROCAUC=0.90, Specificity=0.97, Sensitivity=0.83), Age (ROCAUC=0.84, Specificity=0.70, Sensitivity=1.0), CBF-mean (ICA) (ROCAUC=0.82, Specificity=0.91, Sensitivity=0.83), and CBF-mean (VBA) (ROCAUC=0.65, Specificity=0.55, Sensitivity=0.83). In two-variable SVM analysis, the four highest performing variable combinations were CBF-mean (ICA) and CVR_{Delay}-mean (VBA) (ROCAUC=0.94, Specificity=0.85, Sensitivity=1.0), CBF-mean (ICA) and CVR_{Delay}-99th% (VBA) (ROCAUC=0.93, Specificity=0.79, Sensitivity=1.0), CVR_{Delay}-mean (VBA) and CVR_{Delay}-99th% (VBA) (ROCAUC=0.89, Specificity=0.97, Sensitivity=0.83), and CVR_{Delay}-mean (VBA) and CBF-CoV (ICA) (ROCAUC=0.88, Specificity=0.88, Sensitivity=0.83). Four variables discriminated hemispheres progressing to new infarcts on Wilcoxon rank-sum analysis: CBF-mean (ICA) ($p=0.001$), CVR_{Delay}-mean (VBA) ($p=0.006$), CBF-CoV (ICA) ($p=0.045$), and CBF-std (VBA) ($p=0.049$).

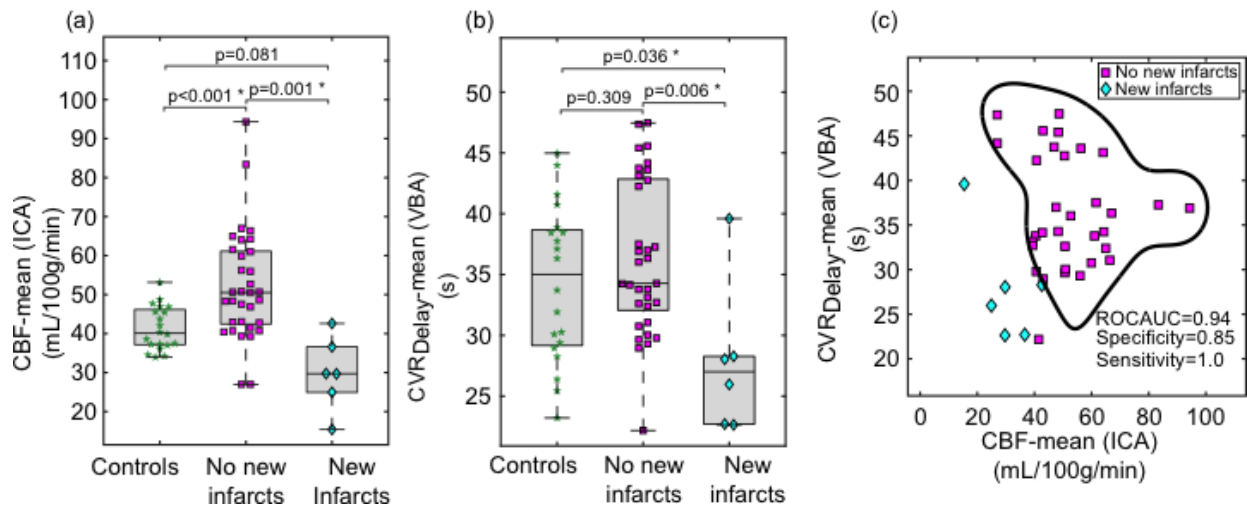


Figure 12. Predicting Recurrent Infarcts in Moyamoya Using Machine Learning and Group-Wise Comparisons. Boxplots and SVM analysis with two promising variables for distinguishing hemispheres with vs. without new infarcts. Boxplots are (a) CBF-mean (ICA) in which recurrent vs. no recurrent stroke hemispheres has $p=0.001$ and (b) CVR_{Delay}-mean (VBA) in which recurrent vs. no recurrent stroke hemispheres has $p=0.006$. SVM analysis is shown in (c), in which an ROCAUC=0.94, Specificity=0.85, and Sensitivity=1.0 is found for distinguishing recurrent stroke risk with CVR_{Delay}-mean (VBA) and CBF-mean (ICA).

2.4 Discussion

This study analyzed non-invasive hemodynamic imaging and demographic variables from patients with non-atherosclerotic intracranial stenosis and moyamoya to understand if machine learning could be applied to classify hemispheres by arterial stenosis confirmed by gold-standard, invasive catheter angiography. The primary hypothesis is that endovascular image artifacts, which are often assumed to complicate interpretation, display maximal performance of the variables considered in support vector machine (SVM) algorithms for distinguishing moyamoya hemispheres supplied by vessels with vs. without arterial steno-occlusion. In an exploratory analysis, $CVR_{\text{Delay-mean}}$ (VBA), CBF-mean (ICA), $CVR_{\text{Delay-99}^{\text{th}}\%}$ (VBA), CBF-CoV (ICA), and age were identified through similar machine learning procedures as having potential relevance for discriminating hemispheres at risk of developing new infarcts.

Functional contrasts identified for classifying arterial stenosis or recurrent stroke status reflect physiology previously identified in the literature. CBF-std (ICA) is consistent with endovascular signal artifacts due to delayed blood arrival. Increasing arterial collateralization throughout moyamoya progression causes longer blood arrival and arterial circulation times on the order of 2-3s in many patients¹¹⁷, resulting in labeled blood water remaining in the arterial tree during pCASL acquisition when typical post-labeling delays of 1.5-2s are used. This incomplete water exchange can result in heterogeneous signal intensity and over-estimation of CBF in pCASL data. Zaharchuk et al.¹²², showed that hyper-intense endovascular signal artifacts on arterial spin labeling MRI indicated arterial collateralization in moyamoya disease, confirmed by digital subtraction angiography. Mutsaerts et al.¹²¹ also explored the relationship of CBF-CoV to complex cerebrovascular architecture in older adults with hypertension, and demonstrated that CBF-CoV is correlated with arterial transit time. More recently in patients with steno-occlusive disease it was shown that CBF-CoV can provide contrast consistent with perfusion abnormalities¹³⁰. Customization of pCASL labeling parameters is also an active area of research to address these limitations, and both correction and optimization strategies have been proposed¹³¹. In reactivity experiments, it was also previously demonstrated through cross-correlation time-delay analysis that moyamoya patients with intracranial stenosis have delayed hemodynamic response functions to respiratory stimuli⁹. These findings agree with the results of machine learning techniques presented in this work and specifically that arterial arrival artifacts on commonly-parameterized ASL images have potential diagnostic relevance in patients with moyamoya. Interestingly, CBF-mean (ICA), while commonly used to identify status of cerebrovascular disease, was not identified as a high performing variable for distinguishing

hemispheres supplied by stenotic vessels in this study. This may be unique to moyamoya pathophysiology, possibly resulting from high endovascular signal artifacts artificially elevating the quantified mean CBF values. Functional variables that are conventionally used for distinguishing cerebrovascular impairment, such as CBF-mean and CVR-mean did not always have highest performance in machine learning classification and group-wise comparisons compared to time delay variables that are less often recorded, such as CBF standard deviation and mean reactivity delay.

It is also likely that some hemodynamic parameters considered here represent redundant information. For example, both CBF-std (ICA) and CBF-99th% (ICA) were found to be significant in group-wise analyses. CBF-std is elevated in patients with moyamoya due to hyperintense signal artifacts in pCASL acquisition caused by long arterial transit times. However, CBF-99th% is elevated in moyamoya due to the same reasons in many cases. Additionally, since the CBF-CoV was found to be correlated with CBF-std (ICA) in controls ($r=0.72$) and hemispheres with mild stenosis ($r=0.74$) and with CBF-mean (ICA) in hemispheres with severe stenosis ($r=-0.72$), CBF-std, CBF-mean, and CBF-CoV represent redundant information to some extent, however this appears to vary with stenosis severity (**Figure 13**).

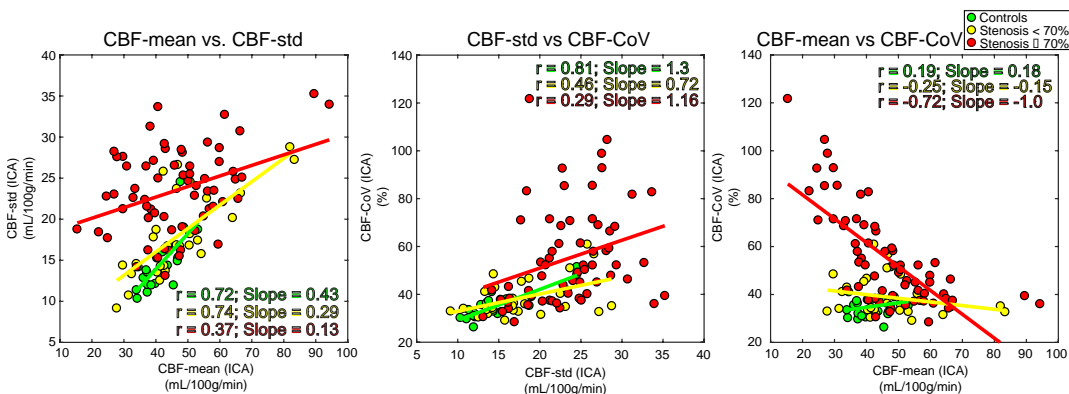


Figure 13 Comparisons Between CBF-mean, CBF-std, and CBF-CoV, Three Related Parameters. A regression analysis comparing ICA variables CBF-CoV, CBF-std, and CBF-mean at different stages of moyamoya severity, defined as control hemispheres, moyamoya hemispheres supplied by arteries with stenosis < 70%, and moyamoya hemispheres supplied by arteries with stenosis \geq 70%. CBF-std (ICA) is correlated with CBF-mean (ICA) for controls ($r=0.72$) and hemispheres supplied by mildly stenotic vessels ($r=0.74$), but not in hemispheres supplied by severely stenotic vessels ($r=0.37$). The CBF-CoV was correlated with CBF-std (ICA) in control hemispheres ($r=0.81$) and with CBF mean (ICA) in hemispheres supplied by severely stenotic vessels ($r=-0.72$), however no other regressions including CBF-CoV presented $|r| > 0.46$. These findings indicate that CBF-CoV is more closely related to CBF-std in control hemispheres, but is more determined by CBF mean in tissue affected by reduced blood flow and increased arterial transit times at later stages of moyamoya.

SVM use with functional hemodynamic information extends earlier results demonstrating that machine learning, which has been applied to provide promising anatomical¹¹², and functional^{47, 104, 132} classifications, also has diagnostic potential in cerebrovascular disease patients with complex vascular architecture and function. For example, Asadi et al. 2014¹³³ used

ANN and SVM algorithms to predict outcomes for patients receiving thrombectomy for acute ischemic stroke. Additionally, Collij et al. 2016¹⁰⁴ used SVM classifiers to discriminate patients with suspected Alzheimer's disease, from mild cognitive impairment, from subjective cognitive decline using ASL perfusion maps. These findings collectively offer increased support that both anatomical and functional hemodynamic imaging can serve as important machine learning inputs. As functional changes generally precede anatomical changes, machine learning using functional data may have even more relevance for identifying disease trajectory. Applying different classification algorithms to the problem addressed in this study has the potential to improve classification performance. SVM algorithms have the advantage of high performance in binary classification, and no local minima in optimization, however SVM performance is dependent on the choice of kernel, and most SVM theory is developed for binary classification¹³⁴. One possible alternate classifier is the convolutional neural network (CNN)¹³⁵, which exhibits good feature extraction and high performance for analyzing and processing MRI images, and has been implemented in processing and interpretation applications for functional data¹³⁶, segmentation^{111, 137}, and reconstruction¹¹³. The random forest classifier may also perform well for distinguishing moyamoya patients based on functional image properties¹³⁸. The random forest algorithm can be robust against over-fitting, having high performance in classification tasks, and success in a wide variety of applications, including image segmentation¹³⁹, and disease classification¹¹⁴. Many algorithms may be suited for identifying characteristic physiology in hemo-metabolic images, however we chose SVM since it inherently accounts for non-linearity in data, always finds global solutions, and is relatively resistant to over-fitting for a non-parametric algorithm¹³⁴. Finally, machine learning is often associated with big data applications, to which this study's sample size is comparatively small. Particularly in the exploratory analysis (22 patients with follow-up imaging), where sample size imbalances could bias SVM algorithms. Therefore, these results should be interpreted with caution. However, they could provide motivation for future investigations with larger sample sizes. We considered sample size concerns here by using supervised SVM algorithms with no more than three dimensions, reducing model complexity and sensitivity to over-fitting.

VBA involvement in patients with new infarcts was unexpected, since only one hemisphere that displayed new infarcts had their stroke in the VBA flow territory. However, this could suggest that abnormal vascular compliance in the VBA territory may indicate a global increase in infarct risk. One possible explanation for the finding that CVR_{Delay} in the VBA flow territory is reduced at later stages of disease is that since highly impaired moyamoya patients typically have extreme stenosis in bilateral anterior flow territories, the VBA supplies anterior

flow territories via flow through the posterior communicating artery or other collateral pathways. This may reduce CVR_{Delay} in the VBA flow territory. This could occur with greater severity at later stages of disease, making reduced CVR_{Delay} (VBA) in moyamoya patients indirectly representative of anterior flow impairment and high risk for stroke. Importantly, of all the parameters considered, the parameter most prognostic for new infarcts was simply the mean hemispheric CBF.

It is worthwhile to consider how machine learning results may generalize to other more common cerebrovascular conditions. In atherosclerosis for example, reductions in vascular compliance⁸³ and increased arterial collateralization¹⁰ are also associated with increased severity of impairment, therefore CVR_{Delay} and CBF-std may also provide information for identifying impairment or risk. However, collateralization and hyper-intense signal artifacts are often less extreme and may influence fewer vessels in patients with atherosclerosis. It is likely that atherosclerotic intracranial stenosis will exhibit similar patterns as moyamoya, however the extent and conspicuity of these patterns may often be more subtle; as such, such investigations may require larger sample sizes. For both stenosis severity and new infarct classification, demographic variables were not as prevalent in high-performing SVM algorithms as imaging variables. This is likely due to moyamoya patients not exhibiting many traditional stroke risk factors (e.g., smoking, diabetes, hypercholesterolemia, hypertension) as older atherosclerotic patients. However, age was identified as a high performing single-variable SVM for classifying hemispheres by new infarct status. For these reasons, the findings in this study may not translate directly to atherosclerotic intracranial stenosis or other cerebrovascular disease patients.

2.4.1 Limitations

The results should be considered in light of the following limitations. Patient heterogeneity is always a potential confound in clinical studies. To address this, we enrolled only patients with non-atherosclerotic intracranial stenosis who are typically younger (25-45 years) and in whom traditional stroke risk factors (e.g., hypercholesterolemia, hypertension, and atherosclerosis) are less variable, as these generally become more significant in later life. Additionally, brain hemispheres with prior revascularization surgery were excluded. Second, we utilized a hypercapnic-hyperoxic stimulus, which is medical grade and available at most medical centers, although application for reactivity mapping remains as an off-label use. Hypercapnic-hyperoxia does not elicit the same CVR response as hypercapnic-normoxia, however

hypercapnic-hyperoxia has been characterized in terms of its effect on blood and tissue R_2^{*119} , sensitivity to lateralizing disease in patients with cerebrovascular disease^{13, 97}, and its correlation with hypercapnic-normoxic stimuli (though the relationship is not 1:1)¹³. Third, the proportion of gray and white matter in volumes of interest will affect values calculated in these regions, due to different levels of perfusion, transit time, and reactivity in gray matter versus white matter; however, this is likely not a major confound in this study as we utilized identical regions in all subjects and therefore similar levels of gray and white matter were present in all participants. Fourth, two slightly different pCASL labeling protocols were implemented in this study, which resulted from the long 7-year duration of data collection and a minor change to the imaging protocol. The main difference between these protocols is a 275 ms (1525 ms vs. 1800 ms) difference in post-labeling delay. Error associated with this variation is not expected to be a major confound relative to the long arterial circulation times in patients with moyamoya which are typically 2000-3000 ms¹¹⁷, however some variability could arise due to this difference. Finally, patient motion is always a potential confound in imaging studies. To address this, we implemented standard motion correction protocols, and visually inspected images for residual peripheral signal brightening artifacts on ASL or focal hyperintensities in the BOLD CVR time course before inclusion in data analysis. We did not observe any differences in motion between groups, however we cannot rule out that some residual variation did exist.

2.4.2 Conclusion

In conclusion, we utilized machine-learning techniques to identify characteristic moyamoya physiology from functional hemodynamic images, and used this information to classify patients into groups determined by clinical indicators of impairment, including both vasculopathy extent and development of new infarcts. We found that functional properties that perform well for classification, such as standard deviation of cerebral blood flow and mean delay in cerebrovascular response to stimulus, can be attributed to known characteristics of moyamoya progression, such as development of arterial collaterals and smooth muscle dysfunction. In an exploratory analysis of patients with new infarcts, the most prominent variable of those measured for predicting new infarcts was the baseline CBF in the anterior flow territory.

CHAPTER 3: A Magnetic Resonance Imaging Study of Pre-Surgical Indicators of Revascularization Response in Adults with Moyamoya Vasculopathy

3.1 Introduction

In clinical practice, symptomatology and anatomical information largely in the form of angiography inform clinical decisions. However, this information does not provide insight regarding tissue function, which is critical for understanding how tissue is responding to impairment. Tissue function can also inform on disease trajectory, which is particularly relevant in diseases like moyamoya, in which treatment outcomes are difficult to predict. In this chapter, we investigate tissue reactivity parameters as biomarkers for positive outcomes to surgery with the goal that these parameters may help to triage patients with moyamoya for therapies.

Moyamoya disease (MMD) is a cerebrovascular condition characterized by frequently progressive non-atherosclerotic arterial stenosis of the intracranial segments of the internal carotid arteries (ICA), as well as proximal middle cerebral arteries (MCA), and anterior cerebral arteries (ACA), and carries more than a seven-fold increased risk of stroke²⁴.

Appropriate MMD management frequently includes surgical revascularization with direct revascularization (e.g., superficial artery to middle cerebral artery bypass), indirect revascularization (e.g., encephaloduroarteriosynangiosis, EDAS or pial synangiosis), or a combination of the two procedures¹²². However, not all persons with moyamoya who undergo surgical revascularization have similar or successful outcomes, and the factors which underlie these differences in response to surgery are inconclusive²⁴. Previous work has been conducted on vessel patency post-surgery in moyamoya disease, however work investigating metabolic function and neoangiogenic response post-surgery is more limited¹⁴⁰. An important issue that would improve informed selection of patients for therapies pertains to whether personalized functional tissue signatures may be used to portend the variable course of surgical response.

The standard for grading moyamoya severity and revascularization success is digital subtraction angiography (DSA), however this method provides an incomplete picture of disease as it does not convey functional information^{51, 141}. Unfortunately, MRI-measures of CBF are complicated in moyamoya by long arterial circulation times, which can lead to low signal-to-noise ratio and endovascular signal artifacts on non-invasive approaches, particularly ASL¹²². Cerebrovascular reserve capacity and collateral circulation may be more specific indicators of vascular health and potential for collateral pathway formation in patients with moyamoya, and as such CVR measures are being adopted with increasing frequency^{89, 142}. In CVR measurements conducted in this study, vessels are challenged using a hypercapnic-hyperoxic stimulus

vasodilatory stimulus to evaluate abilities of arteriolar smooth muscle to relax to increase CBV and CBF, an indicator of the hemodynamic reserve capacity^{124, 143, 144}. This stimulus has been investigated previously for reproducibility and sensitivity to lateralizing disease in moyamoya¹³. Promising CVR measurements without an external stimulus are under development as well^{89, 95}.

The *time* for the maximal CVR response (i.e., CVR_{Delay}) and the maximal CVR response itself (i.e., CVR_{Max}) may provide a more complete perspective on hemodynamic status than a static measure of basal CBF or macrovasculopathy alone, especially in MRI studies owing to known limitations of non-invasive CBF measurements in the setting of arterial vasculopathy^{9, 102}. In small cohort studies, reactivity metrics have recently been reported to correlate with infarct progression in adults with moyamoya¹⁴¹. Moyamoya frequently has preserved patency of the vertebrobasilar arteries (VBA) until advanced stages of disease, including preserved CBF and possibly autoregulatory capacity of posterior territory microvasculature as well^{122, 145}. Due to the severe intracranial stenosis that occurs in the internal carotid arteries and their main branches in moyamoya and the relative preservation of the posterior circulation, blood from the VBAs often supply anterior brain regions through circuitous collateral flow pathways, and may also provide an important route for circulating growth factors or other markers of ischemic stress which may play a fundamental role in neoangiogenesis¹⁴⁶⁻¹⁴⁹.

Of additional interest, it remains unclear whether demographic parameters such as age, race, and gender might affect revascularization outcome. This is particularly important given the increasingly recognized North American moyamoya phenotype²⁴. Specifically, while idiopathic MMD was historically identified in persons of East Asian ancestry, a more common North America moyamoya phenotype in the United States has been identified as well, and it is possible that risk factors that influence East Asian versus North American moyamoya condition trajectory are non-overlapping^{44, 150-152}. In support of this, an analysis of moyamoya patients identified from the United States National Inpatient Sample between 2008 and 2015 provided evidence for increasing moyamoya prevalence in that time, and for moyamoya incidence being inversely related to median income and directly related to urban locations¹⁵². Following retrospective analysis of records from 4,474 adult and pediatric North American moyamoya patients, it was also observed that Black patients were less likely to undergo surgical revascularization compared to patients of other races¹⁵¹. As such, understanding the North American moyamoya phenotype, and specifically potential influence of race on treatment response, is warranted.

The logical extension of this work is to understand whether pre-surgical hemodynamic profiles may predispose patients to collateral vessel formation and as such better surgical outcomes. The aim of this study was to identify pre-surgical hemodynamic MRI profiles, specifically higher VBA flow-territory CVR and reduced CVR response times in response to a vasoactive stimulus, that are associated with better revascularization outcomes at one-year follow-up. A secondary aim is to confirm that both race and age influence revascularization success between racial demographic groups included in this study, which includes Black and White moyamoya participants.

3.2 Methods

3.2.1 Participants

All participants provided informed, written consent for this prospective, interventional study. All study components were performed in compliance with the Declaration of Helsinki of 1975 (and as revised in 1983), Health Insurance Portability and Accountability Act, and all components of the study were approved by the local Institutional Review Board (*number and location removed to preserve double-blind peer-review*).

Participants were identified from the local Neurology and Neurosurgery services between November 1, 2013 and January 8, 2019. Criteria for inclusion were adults with a clinical diagnosis of moyamoya confirmed by DSA and scheduled for revascularization surgery in one or both hemispheres. Idiopathic or syndromic etiology were documented and considered separately in sub-analyses, in which age analysis comparing response groups was repeated excluding participants with syndromic moyamoya (who are older, as expected, given increasing prevalence of atherosclerosis with age). Exclusion criteria were pregnancy, moyamoya secondary to sickle cell anemia, chronic infarct larger than 1/3 of the MCA territory, greater than 1/3 MCA territory vascular collateralization before surgical intervention (determined from pre-surgical clinically indicated DSA), or independent condition expected to lead to death in less than two years. Participants received DSA within one month prior to a clinically-indicated surgical revascularization and again at approximately one-year follow-up. A target of one-year follow-up was chosen as this is the approximate expected timeline for neovascularity to occur post-EDAS, as has recently been summarized from 63 revascularized hemispheres at median follow-up of 14 months) ¹⁵³. Within six months prior to revascularization, MRI including anatomical and hemodynamic imaging was performed as outlined below.

3.2.2 MRI

MRI studies were performed using a 3.0T MRI scanner (Philips Healthcare, Best, The Netherlands) with body coil RF transmission and phased array SENSE reception.

Anatomical images included diffusion-weighted imaging (spatial resolution=2.05x2.56x4.00mm, $b=1000$ s/mm², single shot echo planar imaging (EPI), repetition time (TR) and echo time (TE) TR/TE=3149/83 ms), T_2 -weighted (TR/TE=3000/80 ms; resolution=0.6x0.6x4.0 mm³), T_2 -weighted axial fluid-attenuated inversion recovery (FLAIR) (turbo inversion recovery; TR/TI/TE=11000/2800/120 ms; spatial resolution=0.9x1.1x3.0 mm³), and T_1 -weighted (magnetization-prepared-rapid-gradient-echo; spatial resolution=1.0x1.0x1.0 mm³, 3D turbo field echo; TR/TE=8.2/3.7 ms) scans.

Pre-surgical CVR-weighted images were obtained during BOLD imaging (TR/TE=2000/30 ms; spatial resolution 3.0x3.0x3.5 mm³; 360 dynamics) with a vasodilatory hypercapnic-hyperoxic stimulus (95% O₂, 5% CO₂). Stimulus was delivered via a non-rebreathing facemask supplied by compressed gas cylinders at a flow rate of 12 L/min with nasal cannula for end-tidal CO₂ (ETCO₂) monitoring. The stimulus paradigm consisted of 180 seconds hypercapnic-hyperoxia interleaved with 180 seconds room-air repeated once. Throughout the scan, respiratory rate, blood pressure, end-tidal CO₂, arterial oxygen saturation, and heart rate were monitored (Medtronic, Dublin, Ireland), the stimulus was considered well-tolerated if the participant was able complete the study without an adverse event.

3.2.3 Revascularization surgery

All participants underwent a form of indirect surgical revascularization. Participants underwent either indirect revascularization via encephaloduroarteriosynangiosis (EDAS) or combination superficial temporal artery-to-middle cerebral artery (STA-MCA) bypass and indirect surgery; participants with different surgery types were considered separately on sub-analyses¹⁵⁴. Revascularization type was determined by clinical indication and caliber of the STA and MCA, when appropriate. Postoperatively, participants were brought to the neuro-intensive care unit for recovery where they were closely monitored for neurologic changes. Participants were maintained on antiplatelet medication and intravenous fluids overnight for hydration. Blood pressure parameters were managed to minimize hypertensive episodes that could lead to hemorrhage, or hypotensive episodes that could lead to ischemia.

3.2.4 Digital subtraction angiography

Both *pre-* and *post-* surgical DSA utilized a six-vessel injection protocol, performed in the neuroangiography suite using a Philips Allura Xper biplane neuro X-ray system with the participant in the supine position. Selected arterial catheterizations of bilateral external carotid arteries, bilateral internal carotid arteries, and bilateral vertebral arteries were performed in multiple projections using nonionic, water-soluble intra-arterial contrast. All injections were performed by hand by the collaborating neurovascular surgeon using the following volumes and rates: ICA injections: 3–4 cc over 0.5s, external carotid artery injections: 2–3 cc over 2s, common carotid artery injections: 4–5 cc over 0.5s, and VBA injections: 4 cc over 2s. Digital images were acquired at three frames/second.

3.2.5 Analysis

Post-surgical arterial collateral grading was performed by three independent raters, including one board-certified neuroradiologist (LTD, experience = 8 years) and two board-certified cerebrovascular neurosurgeons (RVC, experience = 8 years; MRF, experience = 9 years). At the Vanderbilt Hospital where this study was conducted, catheter angiograms of the head and neck are performed and evaluated exclusively by the cerebrovascular neurosurgery service. Therefore, members of this service, along with neuroradiology, were included as qualified raters. The three raters independently used DSA to ensure inclusion criteria and classify participant hemispheres. The graders were blinded to results of all MR experiments. Gradings were taken from a lateral projection of DSA during the late arterial phase following external carotid artery injection, depending on MCA territory filling due to arterial collateralization^{19, 155}. One group comprised participants with poor response to revascularization surgery, with less than 1/3 MCA territory collateralization. The second group of participants consisted of those with good responses, defined as greater than 1/3 MCA territory collateralization. Additionally, modified Suzuki Scores (mSS), were recorded by a board-certified neuroradiologist using standard criteria¹⁵⁵. Stage 0: no evidence of vessel disease; Stage 1: mild-to-moderate stenosis around the carotid bifurcation with absent or slightly developed ICA disease; Stage 2: severe stenosis around the carotid bifurcation or occlusion of either the proximal ACA or MCA with well-developed ICA disease; Stage 3: occlusion of both the proximal ACA and MCA with well-developed ICA disease (few ACA or MCA branches are faintly opacified in antegrade fashion); and Stage 4: complete occlusion of both the proximal ACA and MCA (without antegrade opacification).

Prior infarcts were recorded by the same neuroradiologist using structural MRI results. Infarcts were defined as being hyperintense, visible in two planes, and being at least 3 mm in one dimension on T_2 -weighted FLAIR, and hypointense approaching CSF signal on T_1 -weighted imaging. The rater was blinded to other hemodynamic and functional imaging findings while recording prior infarcts.

BOLD preprocessing included motion correction using Functional Magnetic Resonance Imaging of the Brain Software Library (FSL) and spatial smoothing with a kernel of full-width-half-maximum = 3 mm¹⁰³. Following affine motion correction, BOLD images were evaluated for motion corruption, and any images with residual motion that was deemed to preclude interpretability were documented and excluded. BOLD images were co-registered to a 2 mm Montreal Neurological Institute (MNI) atlas, where T_1 -weighted images served as an intermediate template to register images from BOLD to standard MNI space using linear co-registration (FMRIB's Linear Image Registration Tool; FLIRT) with 12 degrees of freedom. Next, two CVR parameters were calculated from the BOLD reactivity data. To analyze time-delayed vascular response to stimulus, a rectangular regressor, which represents the gas stimulus paradigm, was applied and advanced in time until maximum correlation between voxel time course and shifted regressor was found¹³. Time until maximum correlation was defined as CVR_{Delay} (seconds), and the value of maximum correlation as CVR_{Max} (unitless; normalized z-statistic between shifted regressor and voxel time course). These values were calculated on a voxel-wise basis to generate CVR_{Delay} (time delay) and CVR_{Max} (maximal statistical response) maps.

Next, VBA territory masks were applied, and eroded to render them relevant appropriate for the VBA territory regardless of circle of Willis variant¹²⁴. Cerebrovascular reactivity parameters, CVR_{Delay} and CVR_{Max} were calculated within the flow territory mask. In all analyses, flow territories in each hemisphere are considered separately, as moyamoya progression can be asymmetric and separate hemispheres can have aggressive or indolent disease course¹⁵⁵. *Pre-surgical* hemispheres from each parameter map (CVR_{Max} , and CVR_{Delay}) were averaged for participants with poor vs. good collateralization, as defined using criteria from DSA above.

Finally, non-imaging stroke risk factors including age, sex, race, vasculopathy extent, and type 2 diabetes status were recorded.

3.2.6 Posterior circulation variants

To evaluate posterior circulation, the same three raters described above evaluated angiography data to determine PCOM size relative to the PCA in each hemisphere. The posterior circulation

was graded as: (i) only P1 PCA segment visible (PCOM not visible), (ii) P1 PCA segment larger than PCOM, (iii) P1 PCA segment same size as PCOM, (iv) P1 PCA segment smaller than PCOM, and (v) only PCOM visible (P1 PCA segment not visible; i.e., fetal variant). Participants were then categorized into those that had a fetal or fetal-type variant (i.e., categories iii-v) or without any fetal variant (i.e., categories i or ii).

3.2.7 Statistical analysis and considerations

A Wilcoxon rank-sum test was applied to evaluate differences in VBA flow-territory CVR_{Delay} and CVR_{Max} between those with good (e.g., >1/3 MCA territory revascularized) vs. poor (e.g., <1/3 MCA territory revascularized) surgical outcomes. For both functional evaluations, significance was defined as two-sided $p < 0.05$. To control for age and race, CVR_{Delay} and CVR_{Max} were also interrogated via separate logistic regressions as independent variables along with age and race, and with surgical response as the dependent variable. Fisher's exact test was used to determine whether there were significant differences in surgical outcome between participants with or without PCOM greater than or equal to P1 gauge on angiography.

For completeness, descriptive statistics for demographic parameters and other angiographic parameters were reported although these were not part of hypothesis testing. A Wilcoxon rank-sum test was applied to evaluate age differences between groups, whereas a Fisher's exact test was applied to compare race, sex, and posterior circle of Willis variant. To elucidate any potentially confounding correlations, a Fisher's exact test was applied to evaluate if there were significant differences between (i) revascularization procedure (combined vs. indirect) and surgical response (good vs. poor), (ii) moyamoya type (idiopathic vs. syndromic) and surgical response (good vs. poor), (iii) race (Black vs. White) and moyamoya origin (idiopathic vs. syndromic), (iv) surgical procedure (combined vs. indirect) and moyamoya origin (idiopathic vs. syndromic). A Wilcoxon rank-sum test was applied for (v) age and moyamoya origin (idiopathic vs. syndromic).

All Participants: Demographics			
	Idiopathic	Syndromic	Total
N	26	5	31
Age (Years)	42±13	61±9	45±14
Sex (% female)	23F (89%)	3F (60%)	26F (84%)
Black (%)	8 (31%)	1 (20%)	9 (29%)
White (%)	18 (69%)	4 (80%)	22 (71%)
Body Mass Index (kg/m²)	32.6±10.2	33.4±9.9	32.7±10.0
Type 2 Diabetes (%)	7 (27%)	3(60%)	10(32%)
Current Smoker (%)	11 (42%)	1(20%)	12(39%)
Hypertension (%)	10 (39%)	4(80%)	14(45%)
Infarcts (%)	22 (85%)	5 (100%)	27 (87%)

Table 4 Demographic and Comorbidity Information for Moyamoya Participants in Chapter 3.

3.3 Results

3.3.1 Demographics

MR imaging and angiography was performed on 37 participants with moyamoya. Of these, one participant was excluded due to sickle cell anemia, four were excluded for having inadequate and/or non-diagnostic quality imaging, and one participant was excluded for having pre-surgical collateralization >1/3 of the MCA territory. As such, the remaining sample consisted of 31 participants (**Table 4**; sex= 26F / 5M; age= 45±13 years), from which 41 total revascularized hemispheres were considered (**Table 5**). Of 31 participants, 29% were Black and 71% were White (**Table 6**). Participants with idiopathic (n=26) and syndromic moyamoya secondary to atherosclerosis (n=5) were included.

3.3.2 Revascularization response

MRI was acquired 3±3 months before revascularization surgery. No participants had overt strokes between the research scan and revascularization surgery. Of the 41 hemispheres, revascularization procedures were indirect (n=32) or combination (n=9). For post-surgical follow-up, DSA was acquired at 13±8 months post-surgery to evaluate collateral filling of the MCA territory. **Figure 14** illustrates the categorical scoring criteria. For EDAS hemispheres, 18/32 (56%) met angiographic criteria for poor collateralization and 14/32 (44%) met angiographic criteria for good collateralization at follow-up. For combination surgery hemispheres, 5/9 (56%)

All Hemispheres: Revascularization Response			
	Good	Poor	Total
N	23	18	41
Age (years)	41±14	50±11	45±14
Sex (% female)	21F (91%)	13F (72%)	34F (83%)
Black (%)	4 (17%)	9 (50%)	13 (32%)
White (%)	19 (83%)	9 (50%)	28 (68%)
Direct + Indirect (%)	5 (22%)	4 (22%)	9 (22%)
Indirect Only (%)	18 (78%)	14 (78%)	32 (78%)
Fetal or Fetal-Type Posterior Circulation	4 (17.4%)	5 (27.7%)	9 (22.0%)
Modified Suzuki Score	2.3±0.8	2.4±0.9	2.4±0.8

Table 5. Demographic and Surgical Information for Participants in Chapter 3. Demographic and surgical information for all hemispheres separated by those meeting angiographic criteria for good vs. poor neoangiogenic responses to revascularization surgery. A good vs. poor response to revascularization surgery is defined as neoangiogenic collaterals filling >1/3 middle cerebral artery (MCA) territory or <1/3 MCA territory, respectively. Fetal or Fetal-Type Posterior Circulation is defined as the ipsilateral posterior communicating artery being greater than or equal to the size of the P1 segment of the Posterior Cerebellar Artery.

Racial Demographics			
	Black	White	p-value
N	9 (29%)	22 (71%)	
Age (years)	47.3±11.9	44.3±14.5	0.47
Sex (% female)	8F (89%)	18F (82%)	1.00
Body Mass Index (kg/m²)	33.1±10.0	32.6±10.3	0.85
Type 2 Diabetes (%)	4 (44%)	6 (27%)	0.42
Current Smoker (%)	2 (22%)	10 (45%)	0.42
Hypertension (%)	5 (56%)	9 (41%)	0.69

Table 6 Demographic and Comorbidity Information: Demographic Makeup

met criteria for poor collateralization and 4/9 (44%) met criteria for good collateralization at follow-up (**Table 5**). No significant difference was observed between collateralization responses to combination direct+indirect vs. indirect only procedures ($p=1.00$). All participants tolerated the respiratory stimulus well.

3.3.3 Pre-surgical indicators of revascularization success

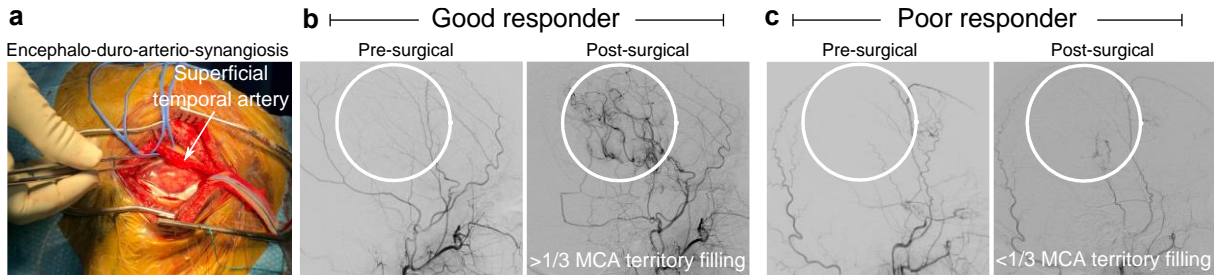


Figure 14 Angiograms for Patients with a Good and Poor Response to Revascularization Surgery. Encephalo-duro-arterio-synangiosis (EDAS) indirect surgical revascularization and varied collateralization responses. (a) During the EDAS procedure, the dura is opened, and the pia and arachnoid are exposed. The superficial temporal artery (white arrow), reflected superiorly by blue vascular loops, is then laid on the surface of the brain, and its adventitia is sutured to the pia to complete the indirect bypass. Pre-surgical and post-surgical Digital Subtraction Angiography (DSA) from a participant meeting criteria for (b) good (25 year-old White female) vs. (c) poor (57 year-old Black female) surgical revascularization response. The poor response fills $<1/3$ the middle cerebral artery (MCA) territory with new collateral vessels, and the good response fills $>1/3$ MCA territory with new collateral vessels. These angiograms show lateral projections from the DSA during the late arterial phase following external carotid artery injection.

All participants tolerated the the respiratory stimulus well by the stated criteria. The EtCO_2 responses to stimulus was 5 ± 1 mmHg (mean \pm standard deviation). Maximum cerebrovascular reactivity in the VBA flow-territory (CVR_{Max}), normalized to the whole-brain mean, was significantly reduced in those meeting angiographic criteria for poor (1.04 ± 0.05 unitless) vs. good (1.12 ± 0.13 unitless) responses. There was no significant difference between mean $\text{CVR}_{\text{Delay}}$ in participants meeting angiographic criteria for good (32.9 ± 8.1 seconds) vs. poor (36.8 ± 8.0 seconds) responses ($p=0.13$). In logistic regression, with age and race included, CVR_{Max} remained significant and $\text{CVR}_{\text{Delay}}$ was not significant. **Figure 15** summarizes case examples of a 28-year-old White participant meeting criteria for good (i.e., $>1/3$ MCA territory revascularized) response to surgery, as well as a 28-year-old White participant meeting criteria for a poor response to surgery (i.e., $<1/3$ MCA territory revascularized). In BOLD experiments, EtCO_2 responses to stimulus was 5 ± 1 mmHg (mean \pm standard deviation). These effects are demonstrated on group-averaged reactivity maps in **Figure 16** and quantitative group-wise comparisons are presented in **Figure 17**.

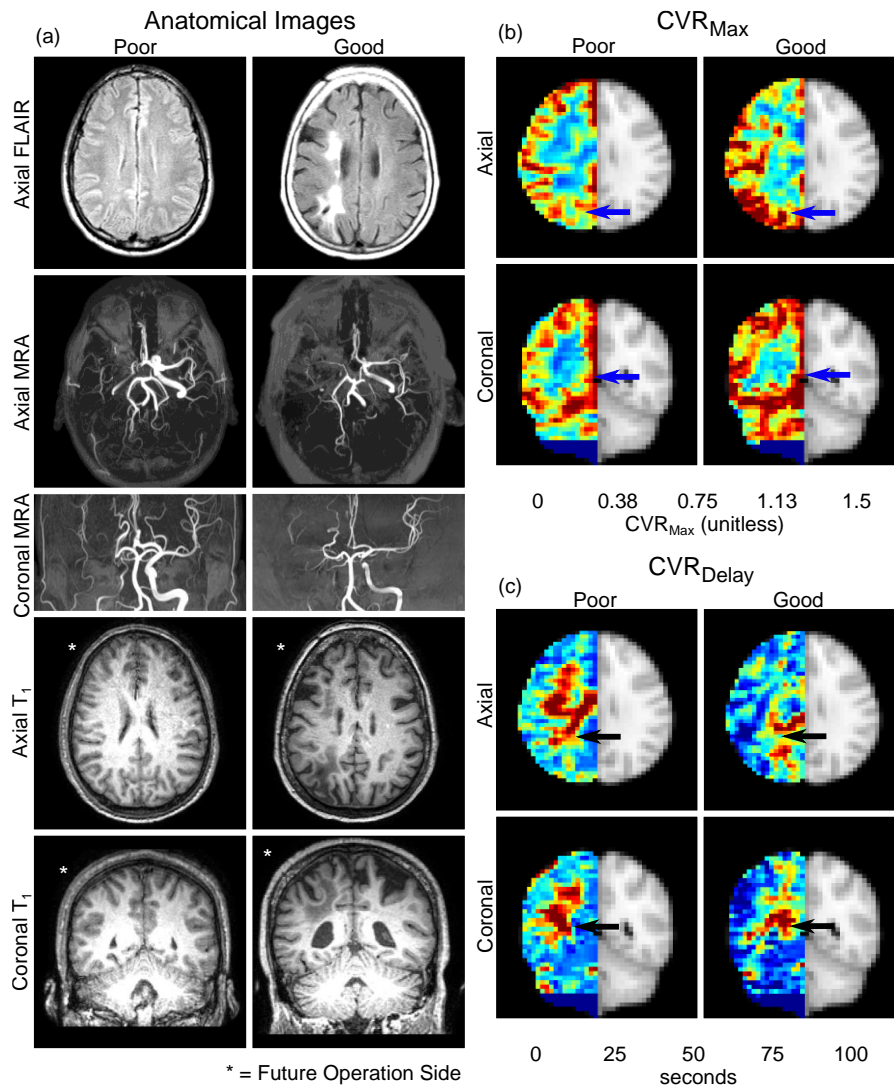


Figure 15 Structural and Functional MRI in Moyamoya Participants with Good and Poor Response to Revascularization Surgery. Group-averaged physiological parameter maps for participants meeting criteria for poor vs. good revascularization responses, with neoangiogenic collaterals filling $<1/3$ middle cerebral artery (MCA) territory (left) vs. $>1/3$ MCA territory (right) respectively. The physiological parameters are normalized maximal cerebrovascular reactivity (top, a; CVR_{Max}) and delay in maximal response to cerebrovascular stimulus (bottom, b; CVR_{Delay}), with the focus of this study on the tissue in the vertebrobasilar artery flow-territory. Participants with good surgical outcomes also had higher CVR_{Max} (blue arrow). A trend for reduced CVR_{Delay} for those with good vs. poor outcomes was also observed (black arrow). *P*-values for these trends are summarized in **Figure 17**.

In secondary analysis of non-imaging parameters, age was a significant predictor of response to surgery where participants with poor response to surgery (age 50 ± 11 years) were older than those with good response to surgery (age $=41 \pm 14$ years). This effect remained significant when age analysis comparing response groups was repeated excluding participants with syndromic moyamoya. Race was also significantly associated with surgical response, whereby White participants had higher collateralization scores post-surgery compared to Black participants (poor response = 9 Black 9 White; good response = 4 Black 19 White). There was no significant difference between males and females for surgical response ($p=0.21$; poor response = 13 female 5 male; good response = 21 female 2 male).

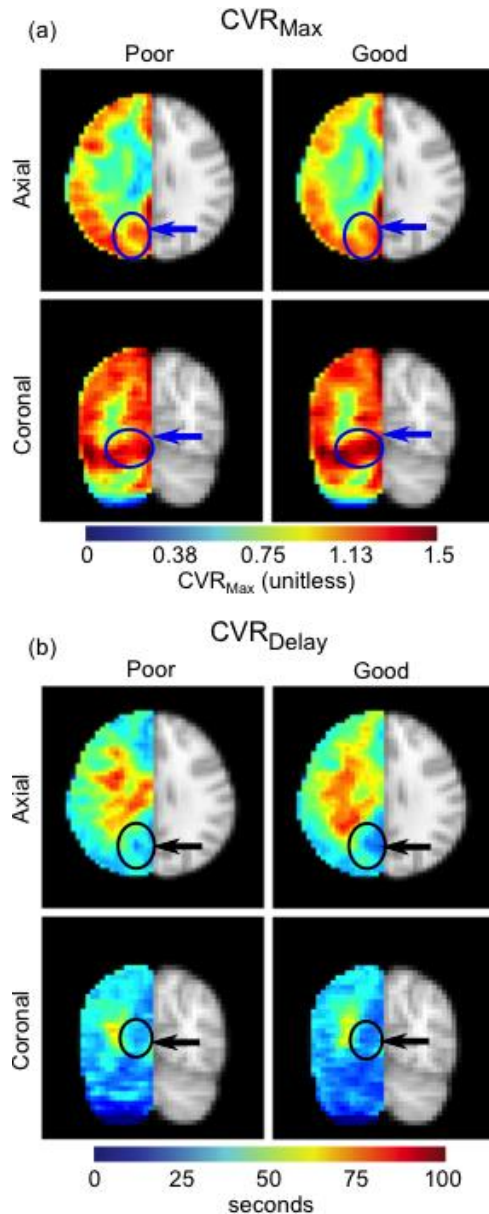


Figure 16. Group-Averaged CVR Parameter Maps for Patients with Good and Poor Response to Revascularization. Case examples of pre-surgical imaging in participants who met angiographic criteria for poor vs. good surgical outcomes at one-year follow-up. A 28-year-old White female with good response (right column) had idiopathic moyamoya, EDAS surgery, and had 22.7 months between revascularization surgery and DSA. A 28-year-old White male with poor response (left column) had idiopathic moyamoya, combination direct-indirect surgery, and had 39.7 months between surgery and DSA. Pre-surgical anatomical images and angiography for participants with good (right) and poor (left) responses to revascularization are shown in (a). Trends identified in Figure 2 and Figure 3 are also demonstrated here, where mean VBA-territory CVR_{Max} is lower (b; blue arrow- Poor Response: 0.94; Good Response: 1.37), and CVR_{Delay} is higher (c; black arrow- Poor Response 37.9s; Good Response: 22.7s), in the participant with the poorer response.

To fully characterize the cohort, properties of response groups are recorded here. There was no difference ($p=1.00$) in surgical outcome between participants who received combination vs. indirect procedures (combination revascularization: poor response 4/9 (44%), good response 5/9 (56%) vs. indirect revascularization: 14/32 (44%) poor response, 18/32 (56%) good response). There was also no statistical difference ($p=0.38$) in surgical outcome between idiopathic vs. syndromic participants (idiopathic: poor response 14/35 (40%), good response 21/35 (60%) vs. syndromic: 4/6 (67%) poor response, 2/6 (33%) good response). There was no difference ($p=1.00$) in racial diversity between idiopathic vs. syndromic moyamoya participants (idiopathic: 11/35 (31%) Black, 24/35 (69%) White; syndromic: 2/6 (33%) Black, 4/6 (67%) White).

Additional cohort characteristics regarding moyamoya subtype macrovascular morphology were also tested and recorded here. There was no statistical difference ($p=0.60$) in surgical procedure assigned to idiopathic vs. syndromic moyamoya (idiopathic: indirect 28/35 (80%), direct+indirect 7/35 (20%); syndromic: indirect 4/6 (67%) direct+indirect 2/6 (33%)). Consistent with expectations, participants with idiopathic moyamoya were significantly younger than

those with syndromic moyamoya secondary to atherosclerosis (idiopathic: 42 ± 13 years; syndromic: 60 ± 8 years). There was no significant difference in the presence or absence of a fetal or fetal-like circle of Willis in those meeting angiographic criteria for good vs. poor responses to surgery (**Table 5**; $p=0.47$). Of 23 hemispheres meeting criteria for good surgical outcomes, 17.4% had a PCOM greater than or equal to the size of the P1 segment of the PCA, compared to 27.7% of 18 hemispheres meeting criteria for poor surgical outcomes. Additionally, CVR_{Max} (non-fetal= 1.10 ± 0.12 ; fetal-type= 1.07 ± 0.07 ; $p=0.49$;) and CVR_{Delay} (non-fetal= 36.51 ± 13.90 seconds; fetal-type: 35.10 ± 10.46 seconds; $p=0.91$) were not different between participants with different circle of Willis variants. Finally, mSS was not different between participants with good vs. poor surgical outcomes ($p=1.00$).

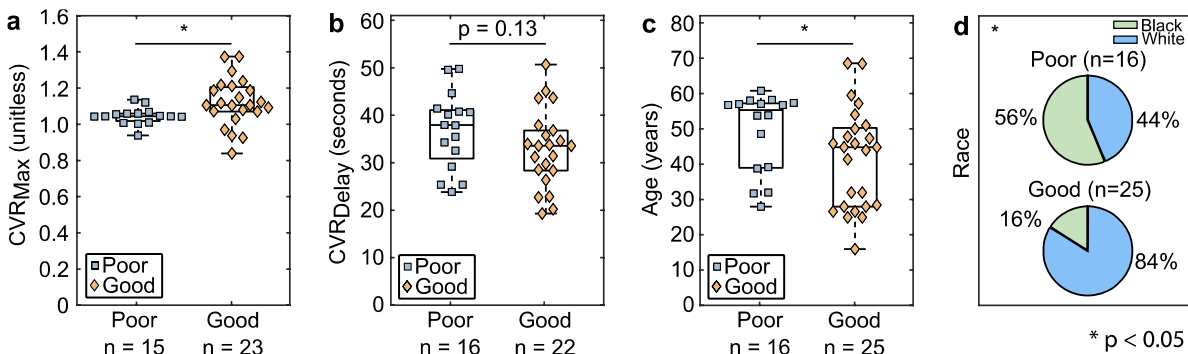


Figure 17 Group-Wise Comparisons Between Functional and Demographic Parameters which Distinguish Surgical Outcome. Boxplots for three continuous parameters, and a pie chart for one categorical parameter showing differences between participants with poor vs. good response. As shown in Figure 2, CVR_{Max} was significantly higher in participants who met angiographic criteria for a good surgical revascularization response (a; $p=0.02$). Although not reaching the threshold for significance, CVR_{Delay} showed a trend for being lower (i.e., faster vascular response time to vasoactive stimulus), in the posterior flow-territory (b; $p=0.08$). Age is also a significant discriminatory predictor of response to surgery of all parameters considered (c ; $p=0.02$), with younger participants having better surgical outcomes. White participants significantly more frequently met angiographic criteria for a better response to surgery compared to Black participants (d; $p=0.04$). Small variations in sample size are seen in this figure due to the outlier exclusion process described in the Methods section.

3.4 Discussion

This study considered hemodynamic and demographic indicators of surgical revascularization outcome in a study of Black and White North American moyamoya participants. Hemodynamic parameters, specifically higher posterior territory reactivity, had potential for portending favorable revascularization responses. Age was a major indicator of revascularization response in moyamoya, whereby younger participants had greater post-surgical MCA territory neo-vascularization. Additionally, race was a significant factor contributing to revascularization, whereby White participants met angiographic criteria for a better revascularization response

more frequently compared to Black participants. This is particularly noteworthy due to the increasing awareness of moyamoya in North America ¹⁵⁶.

It has previously been observed that the VBA flow-territory, i.e. the posterior cerebral circulation, is typically less affected until advanced stages of moyamoya ¹⁵⁷. As vasculopathy progresses, tissue can be supplied by complex networks of arterial collaterals, which are increasingly supplied by the posterior circulation, the communicating arteries, and the ophthalmic artery ¹⁴⁶, ¹⁴⁷. This preservation of posterior cerebral vasculature may help to explain the role of posterior circulation in moyamoya response to revascularization therapy. In this study, greater posterior flow-territory CVR_{Max} , and reductions in CVR_{Delay} , in participants who responded better to surgical intervention provide evidence that participants with these reactivity profiles may have higher collateralization potential. Prior literature has indicated that alternate, especially posterior, flow territories may compensate for anterior impairment in moyamoya. One such study by Vernieri et al. analyzed stroke outcomes in participants with carotid artery occlusion as they relate to collateralization of the ophthalmic artery, the posterior communicating artery, and the anterior communicating artery. It was observed that the greater the number of territories that were collateralized, the lower the likelihood of stroke. Additionally, 60% of participants with no collateralization had a subsequent stroke compared to 38% of participants with only posterior communicating artery collateralization ¹⁴⁶. Furthermore, Strother et al. included 39 participants with moyamoya disease and 33 controls, and found that the ratio of posterior communicating artery lumen diameter to precavernous ICA lumen diameter was significantly higher in participants with moyamoya, indicating posterior contributions to anterior circulation functional impairment¹⁴⁷.

This study's finding that greater posterior reactivity performance indicates likelihood for greater MCA territory reperfusion in response to revascularization in moyamoya extends these studies to demonstrate the likely relevance of pre-surgical posterior circulation reactivity on collateralization success. However, it is also important to note that differences in reactivity, while statistically significant, are frequently subtle. Similar to other diagnostic imaging tools, these trends should complement the broader clinical history and vascular status for the patient, but do not provide a definitive biomarker or revascularization potential. In this study, VBA flow-territory changes indicate potential for MCA territory reperfusion, not necessarily that these posterior flow territories themselves are developing additional collateral networks in response to surgical revascularization. It should also be noted that revascularization surgery for moyamoya is generally considered standard of care for patients with new or recurrent stroke, and performing

a randomized clinical trial whereby participants are randomized into non-surgical arms is unethical.

In this study, cerebrovascular compliance was measured with time-delay analysis. Other methods for measuring CVR that do not correct for reactivity response time, may underestimate reactivity, when long delay times are present as in moyamoya, as has recently been shown ⁹. While the method implemented in this study for acquiring reactivity parameters has the limitation of requiring the delivery of a hypercapnic stimulus, the gas challenge was well tolerated, and no participants reported adverse events during the scan, or discontinued the scan due to discomfort. Promising methods for measuring reactivity using resting state (i.e., without gas stimuli) are under development, in which either breath modulation or resting state CO₂ fluctuations in the blood are used as regressors for estimating different metrics of vascular compliance and reactivity ^{89, 95, 158, 159}. These methods may have promise as well for quantifying reactivity in patients with cerebrovascular disease.

This study utilized CVR parameters, rather than baseline CBF, as hypothesized biomarkers of revascularization potential. This is partly due to accurate measurement of CBF in moyamoya being complex with MRI-based approaches. As the arterial blood T₁ at 3T (1600-1900 ms) is shorter arterial circulation times in moyamoya (frequently 2000-3000 ms), it is often difficult to evaluate CBF reliably using ASL in moyamoya, as labeled blood water remains in the arterial tree, prior to arriving at the capillary exchange site ^{102, 117}. Additionally, other MRI-based CBF methods generally require exogenous contrast agents, which are being regulated more strictly, suffer from difficulties in arterial input function estimation, and are non-ideal for surveillance.

There are several physiological implications of this work as well. Although it has been reported that pediatric populations have more efficacious responses to surgical intervention compared to adults, this study utilizes gold standard post-surgical DSA to confirm that younger adults also have improved surgical outcomes compared to older adults ⁴⁴. Therefore, these findings highlight that age is likely a relevant factor in portending revascularization response in adults as well.

Additionally, revascularization differences between Black and White participants were observed; these differences may have several contributing factors. Polymorphism in the gene RNF213 has been associated with moyamoya disease, and results suggest that race, and as such additional genetic variants, may partially predispose patients to better vs. poorer revascularization

outcomes^{24, 160}. More specifically, moyamoya vasculopathy is associated with angiogenic circulating markers including inflammatory cytokines, circulating progenitor cells, and inflammatory mediators¹⁴⁸. Some individuals may develop few collaterals following revascularization, as the prerequisite circulating factors of angiogenesis may not be present in sufficient concentration. This complexity may be increased by genetic factors that mediate circulating markers of angiogenesis¹⁴⁹. Differences in polymorphisms and potentially associated circulating markers between Black, White, and Asian patients could contribute to the difference in revascularization response. An associated issue may arise from differences in endothelial function, as known differences in chemical equilibrium of superoxide, nitric oxide, and peroxynitrite may predispose Black patients to unique responses to revascularization, even in the presence of similar vascular growth factors¹⁶¹. It is also possible that differences in response to revascularization are attributable to underlying co-morbidities, such as diabetes mellitus and hypertension, which are more common in Black than White individuals¹⁶². However, age, sex, BMI, type 2 diabetes, smoking, and hypertension were not significantly different between Black and White participants in this study. Further studies into the relationships between vessel wall thickening¹⁶³, circulating markers¹⁴⁸, genetics^{149, 164}, and imaging markers for moyamoya are needed to improve the collective understanding of, and treatments for, North American moyamoya.

3.4.1 Limitations

One limitation, which is common in most moyamoya studies, is sample size. This study included 31 participants enrolled over approximately six years, all of whom were well characterized with hemodynamic MRI and surveillance DSA. This study only enrolled adults, required that all participants undergo indirect revascularization, and excluded syndromic participants with sickle cell anemia who have additional reactivity aberrations secondary to the downstream effects of reduce blood oxygen content. This limitation precluded the use of multivariate approaches, however groups were matched for relevant co-variables and these are presented for completeness. To ensure adequate statistical power, the analyses focused on the primary hypothesis, which was isolated to a brain region that was anticipated to contribute considerably to cerebrovascular function in later stages of moyamoya, namely the VBA flow-territory. Therefore, while the sample size was modest, analysis was focused to evaluate a specific hypothesis albeit with the obvious caveat that not all modifiable risk factors could be taken into account, sample size concerns are likely influential in the discovery that significance was reduced for CVR parameters in multi-variate analysis. An additional limitation is that this study

utilized only one scanner, and was performed at a single institution. A third limitation is that idiopathic and syndromic participants with moyamoya secondary to atherosclerosis were included. However, syndromic patients with sickle cell anemia were excluded who have hyperemia secondary to reduced blood oxygen content, and corresponding reduced vascular reserve capacity ¹⁶⁵. Additionally, demographics for both cohorts were reported, and considered participants with syndromic moyamoya separately in a secondary subanalysis to evaluate the role of idiopathic vs. syndromic moyamoya. The expected phenotypic similarity between idiopathic moyamoya and moyamoya secondary to atherosclerosis was supported by this subanalysis. Finally, a future study including only participants with unilateral revascularization surgery could investigate the influence reactivity parameters in the contralateral hemisphere have on revascularization outcomes, and this comparison has previously been shown to have clinical relevance ¹⁶⁶. However, as moyamoya progresses, there is frequently bilateral involvement and revascularization of both hemispheres, and as such the population included here is representative of a generalizable idiopathic moyamoya cohort.

3.4.2 Conclusion

We provide evidence for pre-surgical VBA flow-territory cerebrovascular reactivity being greater in moyamoya participants with greater arterial collateralization in the MCA territory at a one-year follow up for revascularization surgery. This highlights that topographical features of preserved cerebral auto-regulation in moyamoya may contribute to neoangiogenic potential. It was also observed that younger participants, as well as White relative to Black participants, had greater MCA territory collateralization in response to surgical revascularization. Findings provide additional evidence that surgical outcome and disease etiology may be different within North Americans with different racial backgrounds, and that age, race, and posterior hemodynamic patterns should be considered when evaluating potential for treatment response.

CHAPTER 4: Vascular Space Occupancy and Refocused Dual-Echo Asymmetric Spin Echo Variants Improve Quantitative Estimates of Cerebral Metabolism

4.1 Introduction

While oxygen extraction fraction has been shown to be an important biomarker for stroke outcomes, this parameter is typically not considered, due to inaccessibility of methods for measuring it. In this chapter, we improve on an MRI method called the asymmetric spin echo,

which is a non-invasive MRI method for estimating oxygen extraction fraction. Improved accessibility of methods for measuring oxygen extraction could improve stroke outcomes, as this parameter informs on tissue function and stroke risk.

Measures of cerebral metabolism can be made with O-15 PET, however this technique requires ionizing radiation exposure, arterial sampling, and an on-site cyclotron due to the short half-life of O-15, and is therefore suboptimal for surveillance or research studies²². However, alternative methods using MRI are under development for measuring cerebral physiology non-invasively. These metrics are pCASL for cerebral blood flow⁶³, BOLD for cerebrovascular reactivity⁹, Vascular Space Occupancy (VASO) for cerebral blood volume (CBV)¹⁶⁷, and TRUST⁷⁰ or the Asymmetric Spin Echo (ASE)¹⁶⁸ for OEF. Regarding OEF, TRUST has demonstrated high reproducibility, and has been successfully implemented for informing treatment decisions^{14, 169}. However, TRUST is restricted to a single whole-brain measure of OEF and does not provide any other information regarding cerebral metabolism. Alternatively, ASE provides a topographical map of OEF, and also provides a topographical map of venous cerebral blood volume (vCBV) as well.

ASE utilizes a spin echo, with an off-center refocusing pulse to introduce R2' weighting, which is influenced by intravascular oxygen saturation. An extravascular tissue model has been developed for susceptibility effects in brain tissue, which approximates the blood vessel network as infinite-cylinders with negligibly small volume, from which ASE data can be fit for OEF and vCBV using R2', known susceptibility parameters, and hematocrit¹⁷⁰. This method is promising¹⁶⁸, however it has several limitations^{76, 170}. This tissue model only accounts for extravascular tissue signal, and assumes that all susceptibility effects are caused by deoxygenated blood contributions. However, other origins of susceptibility, such as variable iron content¹⁷¹ and field inhomogeneity¹⁷², exist in tissue. The model also treats blood vessels as randomly oriented cylinders, and assumes that the volume of the blood vessels in each voxel is negligible compared to the tissue volume in that voxel¹⁷⁰. These assumptions are not sound in regions of the brain where vessels collect into large veins. Partial volume effects, especially with CSF, can contaminate signal. As a result, ASE measurements may be most reliable in white-matter, where tissue is typically more homogenous, vessel orientation is closer to random, partial volume effects with CSF are minimal, and confounding effects from large vessels are minimized¹⁶⁸. Finally, ASE is often implemented as a multi-readout approach¹⁷², with no refocusing pulse between echoes. As ASE measurements are sensitive to extraneous susceptibility effects, refocusing pulses between consecutive readouts in ASE may help to control for these unaccounted-for sources of susceptibility.

To help control for the unaccounted for intravascular signal in ASE measurements, Methods for nulling intravascular signal have shown success using bi-polar gradients¹⁶⁸. However, bi-directional gradients must be fine-tuned to null intravascular signal, signal nulling is dependent on the chosen encoding velocity parameter, and practically they can only null blood flowing in one direction unless multiple gradients are implemented. Furthermore, this signal nulling module adds to echo time, resulting in reduced MRI signal at readout. Another method for nulling intravascular signal has been developed previously, associated with the vascular space occupancy (VASO) technique¹⁷³, originally designed for estimating cerebral blood volume. VASO uses an inversion pre-pulse with a TI tuned to null intravascular blood water signal, and has been used for measuring cerebral blood volume. However, a similar pre-pulse may be played before the asymmetric spin echo sequence, which may null intravascular signal while avoiding the limitations associated with bipolar gradients, since the VASO pulse will be before the ASE sequence, and not during.

While ASE is a promising method for measuring cerebral metabolism, further developments are needed to overcome its limitations. Variations of ASE have been implemented, including multi-echo approaches and bi-directional gradients for nulling intravascular signal^{168, 172}, though these methods have not solved the issues associated with ASE implementation. In this work, we investigate reproducibility of two novel ASE variants for measuring OEF. First, an ASE variant with a refocusing pulse between the first and second readout is novel, as previous applications of ASE have not implemented a refocusing pulse between consecutive readouts in multi-readout approaches. Second, Vascular Space Occupancy Asymmetric Spin Echo (VASO-ASE) uses a pre-pulse similar to VASO, which nulls intravascular signal. The VASO- prepulse in ASE will negate intravascular signal, thus increasing the measured signals conformation to the assumptions made in the ASE R2' tissue model¹⁷⁰. We hypothesize that novel ASE variants, refocused dual-echo ASE and VASO-ASE, will produce more physiological OEF and CBV values, confirmed by comparison to OEF values measured by TRUST in healthy controls.

4.2 Methods

4.2.1 Participant Recruitment

All participants provided informed, written consent, and the Vanderbilt University Institutional Review Board approved all components of the study. Participants were recruited from Vanderbilt. Criteria for inclusion were adult healthy controls with no known history of neurological condition or cerebrovascular disease. Images were read by a board-certified neuroradiologist for incidental findings including chronic infarct, anatomical abnormalities, or neurodegeneration, these were recorded and their implications were considered for the participants' inclusion in this study. White matter lesions were not considered criteria for exclusion.

4.2.2 Acquisition

All participants underwent an MRI protocol on a Philips (Best, The Netherlands) Ingenia 3.0T containing structural sequences, as well as ASE and TRUST sequences for evaluating reproducibility and cerebral metabolism.

Structural Imaging. All participants underwent axial 2D Fluid-Attenuation-Inversion-Recovery (FLAIR; TR/TI/TE=11000/2800/120 ms; resolution=0.96x1.29x4.00 mm) and 3D T1-weighted MPRAGE (TR/TE=8.2/3.7; spatial resolution=1.0x1.0x1.0 mm).

Asymmetric Spin Echo (ASE). All ASE variants were acquired with TR=4400ms and TE₁=64ms. For sequences with a second echo, TE₂=107ms. Resolution=3.44x3.44x3.00mm, and multi-slice variants had 13 slices with a 3mm slice gap. Parallel imaging was off. Slice acquisition in each TR was acquired with equidistant temporal slice spacing and interleaved spatial acquisition. Fat saturation was accomplished with a SPIR pulse. Peripheral Nerve Stimulation (PNS) and Gradient modes were both set to high (Max B₁=13.5 μ T, Max gradient strength = 22.5 mT/m, max slew rate 180 mT/m/ms) to reduce the duration of the EPI readout, preserving R2' weighting. The refocusing pulse, the shifting of which makes the spin echo asymmetric, is shifted temporally from TE₁/2 by a value τ . τ ranges from 0 to 20 ms acquired in intervals of 0.5ms, resulting in 41 total tau values, each of which is acquired in a separate measurement. Measurements of consecutive tau had randomized acquisition, consistent across all scans and

subjects, to minimize the impact of scanner drift over the ASE scan duration. Two separate scans were acquired each for three ASE variants,

- i) ASE_{RF-} , a multi-slice ASE sequence with no 180-degree refocusing pulse between the first and second echoes, and the standard method for implementing ASE (**Figure 18a**),
- ii) ASE_{RF+} , a multi-slice ASE sequence with a 180-degree refocusing pulse between the first and second echoes (**Figure 18b**),
- iii) Vascular-Space-Occupancy ASE (VASO-ASE), a single-slice single-echo ASE sequence with a pre-pulse at 1039 ms before the excitation pulse for nulling intravascular signal (**Figure 18c**)¹⁷³.
- iv) One scan was acquired for a single slice ASE_{RF-} scan was also acquired in each participant to evaluate single slice ASE against multi slice ASE (**Figure 19**).

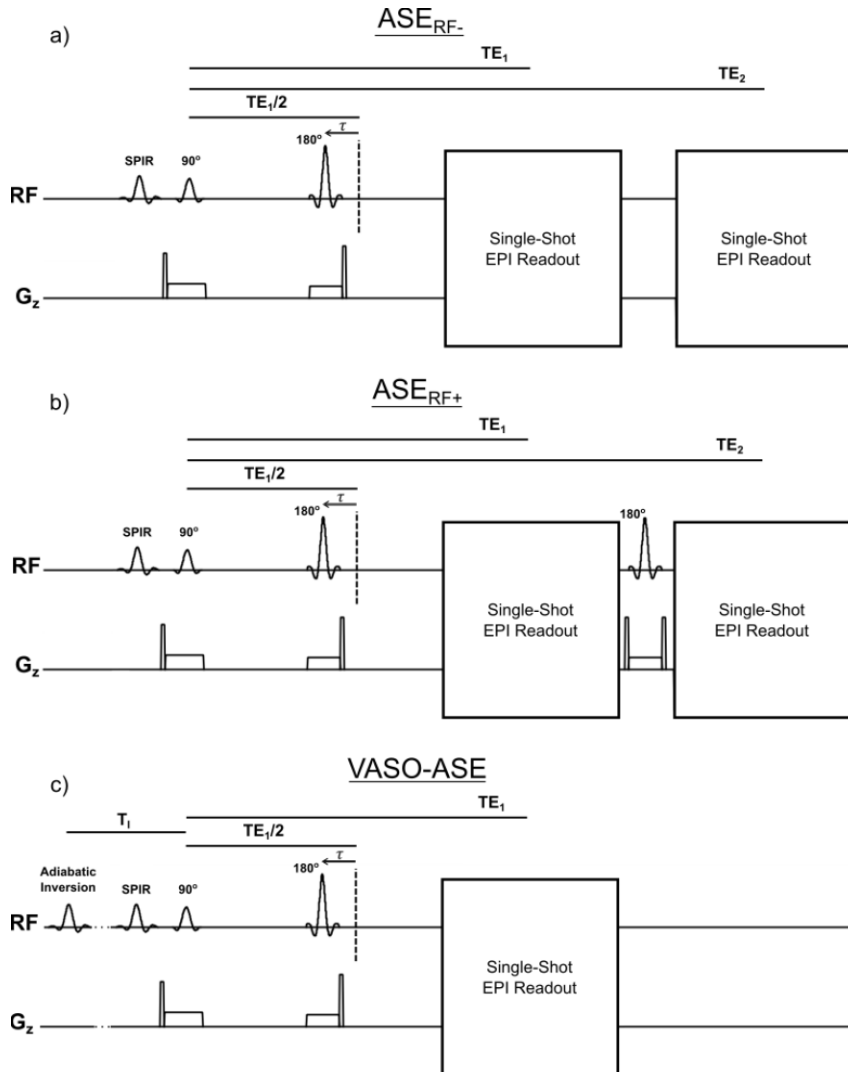


Figure 18. All Pulse Sequences for the Asymmetric Spin Echo (ASE) that are Investigated in Chapter 4. TR= 4400ms and TE₁=62ms. For sequences with a second echo, TE₂=107ms. For VASO-ASE T₁=1039ms, the inversion time for nulling intravascular signal with TR=4400ms. Non-refocused dual echo ASE (ASE_{RF-}) is shown in a) and is the standard method for implementing ASE. Refocused dual echo ASE (ASE_{RF+}) is shown in b) and adds a refocusing pulse between the first and second readout in ASE, which should reduce the extraneous effects of R2' decay between the first and second echo. Vascular space occupancy ASE (VASO-ASE) is in c) and adds an intravascular signal nulling pre-pulse which is intended to bring the measured ASE signal better in compliance with the model which is fit to calculate physiological parameters from ASE. Due to slice timing constraints, VASO-ASE is single echo and single slice, while all other methods have two echoes and 13 slices.

TRUST. TRUST was acquired for measuring whole-brain oxygen extraction fraction^{69, 70}. First cerebral blood-water is either inverted (label) or not (control), followed by a post label delay of 1022 ms. During the post-labeling delay, spins are labeled with a train of refocusing pulses, separated by 10 ms each. This creates an effective TE (eTE), during which T₂ weighting is achieved. Four eTE values are acquired, eTE=1ms, 40ms, 80ms, and 160ms. Arterial oxygen saturation (Ya) was also measured during TRUST with an MRI-compatible pulse-oximeter.

4.2.3 Image Analysis and Processing

Structural Imaging. FLAIR and T1-weighted images were used to record lesions and any structural abnormalities.

ASE. Calculation of physiological parameters has been described in previous literature^{168, 172}. Briefly, a susceptibility model, which relates OEF, R2' and vCBV¹⁷⁰, is fit with logarithmic signal against τ . First, a linear model is fit to logarithmic long-tau signal values ($\tau > 10$ ms), simultaneously for both the first and second echo, which gives the relaxation parameter R2'. A linear model is used because long-tau approximations of the model are linear in τ ¹⁷⁰. The logarithmic short-tau ($\tau \leq 10$) signal values are then fit to a model, which is quadratic in tau as indicated by short-tau approximations of the susceptibility model, and gives vCBV. An example of this fitting is shown in **Figure 20**. These parameters can be input to the equation below to calculate OEF.

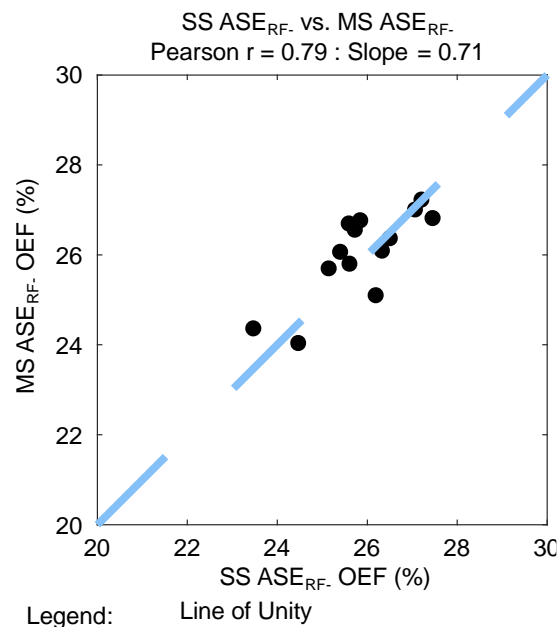


Figure 19 Comparison of Corresponding Single-Slice and Multi-Slice ASE Methods. There was some concern between comparing values from VASO-ASE and other multi-slice ASE variants, so a single slice ASE_{RF} scan was acquired for each participant. However, correlation between the single-slice and multi-slice version of ASE_{RF} have good correlation of WM OEF has good reproducibility.

$$OEF = \frac{R2'}{\gamma \cdot vCBV \cdot \frac{4}{3} \cdot \pi \cdot \Delta\chi_0 \cdot Hct \cdot B_0} \quad (22)$$

Where γ is the gyromagnetic ratio in radians $267.5e6 \frac{1}{s \cdot T}$, $\Delta\chi_0$ is the susceptibility difference between fully oxygenated and fully deoxygenated blood per unit hematocrit $0.18e-6^{174}$, Hct is the small-vessel hematocrit calculated as 85% of the large-vessel hematocrit which is 42 a standard value for healthy controls, and B_0 is the strength of the main magnetic field, 3 Tesla in this case.

For all ASE maps, acquired data were smoothed with a 3-by-3 voxel kernel (10.32 x 10.32 mm) prior to processing, and these images were used to measure mean values. Mean values were acquired by co-registering the images to a standard MNI space, using FSL FLIRT¹⁰³ with T_1 as an intermediary template, and measuring mean values in a standard white-matter and grey-matter atlas. For completeness, to present our data as images with relatively low-resolution sometimes are, the maps were up-sampled to 1mm isotropic, smoothed again with a 9mm x 9mm matrix, and a white-matter mask was applied to eliminate signal from grey matter and CSF voxels.

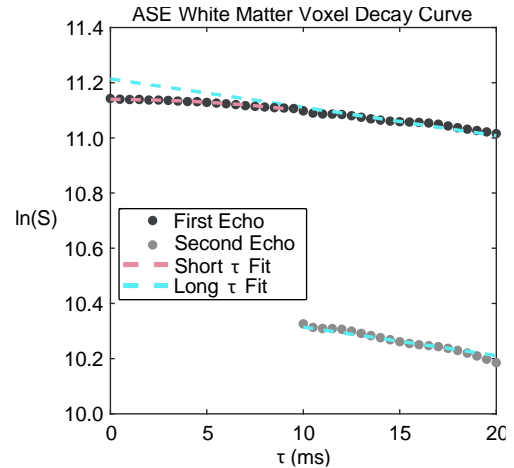


Figure 20 Decay and Signal Fitting in Asymmetric Spin Echo. Decay curve and fitting from a WM voxel in an ASE_{RF}-acquisition. Long tau is fit for R_2' , short tau is fit for vCBV, and OEF is calculated using the procedure described in the methods.

SNR was calculated for OEF maps using a subtraction method¹⁷⁵. The first and second OEF maps are subtracted from one another to acquire a noise map. Images were co-registered and standard MNI atlases were used for ROIs. An ROI map, either for WM or GM, was used to calculate a mean signal value in the ROI from the first OEF map, and a mean noise value from the standard deviation of the signal intensity in the ROI. SNR in the region was calculated as the mean signal divided by $\sqrt{2}$ times the noise value. All images were qualitatively assessed for motion during each scan, and were excluded if motion precluded adequate fitting of ASE data. Where signal maps are shown of acquired ASE images, signal is in arbitrary units, normalized to the 95th percentile of the signal in the $\tau = 0$ ms image for the first echo.

TRUST. TRUST methodology has also been documented previously^{69, 70}. A model calibrated for healthy adult hemoglobin⁸⁸ relating T_2 , hematocrit, and venous blood oxygen saturation (Y_v) can be fit. T_2 is measured from TRUST fitting, hematocrit is assumed to the standard healthy control value 42, and Y_v is calculated from the calibrated model. This is repeated with three measurements, and the signal intensity from the superior sagittal sinus after each eTE gives a

decay curve which can be fit for T_2 . Arterial blood oxygen saturation (Y_a) is measured with pulse-oximetry during the TRUST scan, and OEF can be calculated as shown below.

$$OEF = \frac{Y_a - Y_v}{Y_a} \quad (23)$$

4.2.4 Statistical Analysis

ASE variants are tested to compare reproducibility, as well as correlation with TRUST-measured OEF. Group-wise comparisons are made using a Wilcoxon Rank-Sum test with a significance threshold of $p=0.05$ (Bonferonni correction to $p=0.013$ for four methods used to calculate OEF). Intraclass correlation coefficient (ICC) was calculated for reproducibility metrics, where $ICC = 0.7 - 0.8$ is considered moderate, $ICC = 0.8 - 0.9$ is considered good, and $ICC > 0.9$ is considered great reproducibility. Pearson's r is calculated for reproducibility assessment with the same consideration thresholds as for ICC. A linear model is fit to the data for reproducibility to identify the slope, which can inform on correspondence of one measure to another. Bland-Altman plots were also calculated to visualize reproducibility. Statistical tests are performed on OEF, however other ASE parameters ($vCBV$ and $R2'$) are only evaluated qualitatively, as they are not part of hypothesis testing.

4.3 Results

4.3.1 Participant Demographics

This study includes $n=14$ participants scanned between March 1st and August 8th of 2021. Participants were 27.7 ± 5.2 years old (range=21-42 years), and the population was 50% male and 50% female (**Table 7**). The racial makeup of the cohort was 11/14 (79%) White, 2/14 (14%) Asian, and 1/14 (7%) Black.

4.3.2 Imaging Results

Signal images in ASE for slice seven of thirteen are shown in **Figure 21**. In all ASE variants and for all echoes, signal decreases with increasing tau value. Note that the second echo signal decrease from $\tau = 0$ ms to $\tau = 20$ ms is greater for ASE_{RF-} than for ASE_{RF+}.

Representative quantitative OEF, vCBV, and R2' maps

for each ASE variant are shown in **Figure 22** and boxplots with group-wise mean WM results from each ASE variant are in **Figure 23**. In **Figure 22**, a) shows images as they are output from processing, and b) shows the same topographic maps as they are sometimes shown colloquially with up-sampling and more intensive smoothing. P-values for OEF are shown in **Figure 23** a). OEF reported from ASE_{RF-} was statistically lower than TRUST-measured OEF ($p < 0.01$), however OEF values from ASE_{RF+} ($p = 0.35$) and VASO-ASE ($p = 0.19$) were not significantly different from this standard. Mean values for ASE-measured vCBV are shown in **Figure 23** b). Mean values for ASE-measured R2' are in **Figure 23** c). OEF, vCBV, R2' results, and p-values are shown in **Table 8**.

Scan #	Age	Race	Sex	OEF TRUST	OEF ASE _{RF-}	OEF ASE _{RF+}	OEF VASO-ASE
1	27	White	M	39.8	27	37.7	35.3
2	31	White	F	37.7	24.4	35.8	32.2
3	29	White	F	47.8	26.6	36.2	36.5
4	24	White	F	36.6	24	34	34.0
5	28	Black	M	39.3	26.8	37.7	33.3
6	29	White	F	44	26.7	35.2	35.2
7	42	White	M	36.8	26.1	36.6	32.8
8	32	White	M	31.5	25.7	35.3	33.2
9	24	White	M	38.1	25.8	36	31.3
10	25	Asian	M	44.6	26.4	39	33.9
11	21	White	F	37.2	26.1	40.1	39.8
12	22	White	F	42.4	27.2	40.2	37.2
13	28	White	F	39.3	26.8	36.2	32.2
14	26	Asian	M	36.1	25.1	35.8	34.2
Mean	28	-	-	39.4	26.1	36.8	34.4
St. Dev.	5	-	-	4.2	1.0	1.9	2.3

Table 7 Demographic and MRI-Measured Parameter Estimates of All Participants in Chapter 4. Demographic information for all 14 participants of this study. The cohort was scanned between March 1st and August 8th 2021, and were 27.7 ± 5.2 years old, and was 50% female. Additionally, mean OEF values are shown for the first acquisition of TRUST and each ASE method. For all ASE measures, OEF shown are mean white-matter values.

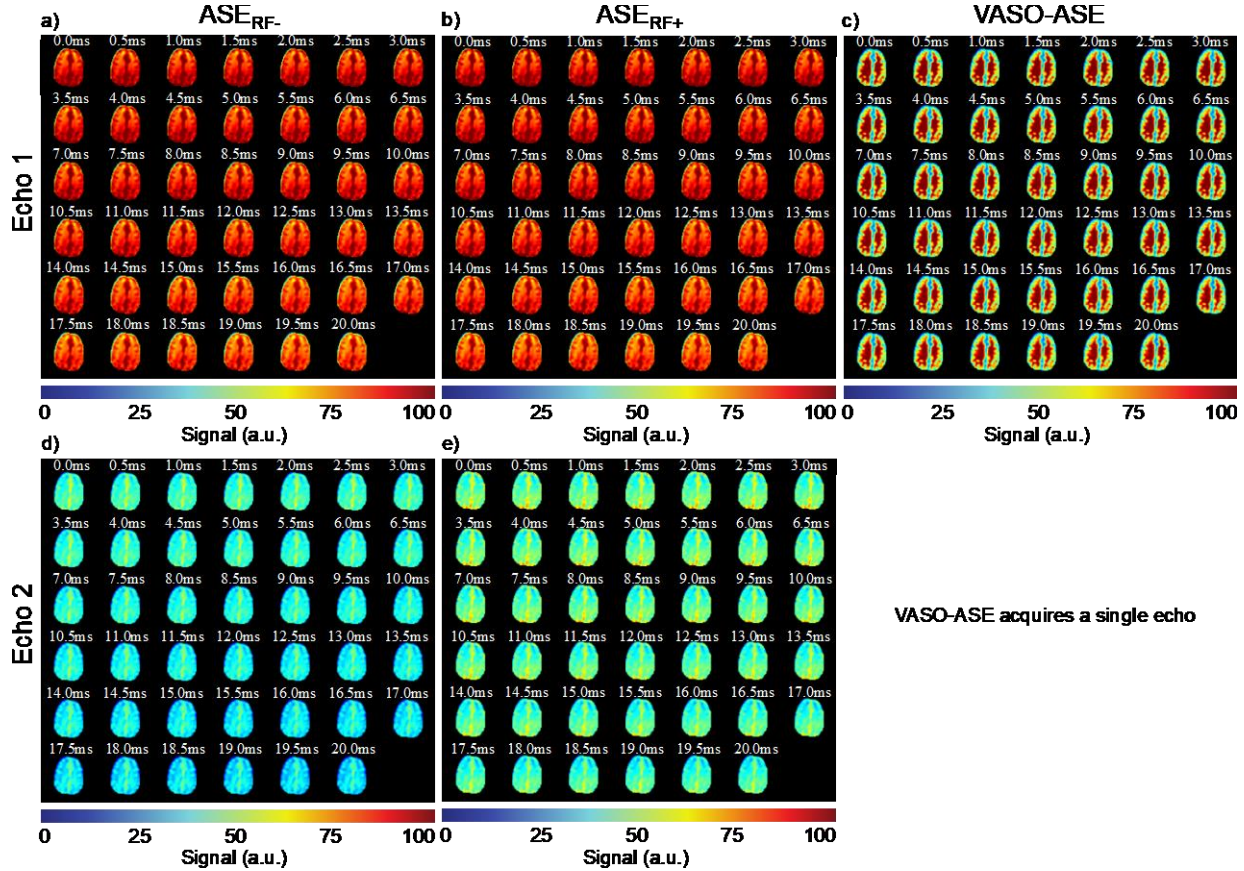


Figure 21 A Signal Montage for Each ASE Method and Each Echo. Mean signal decreases over τ for all methods and all echoes. Mean signal decrease over τ is greater for ASE_{RF-} than for ASE_{RF+}.

SNR values for OEF maps in white matter and grey matter (GM) are shown in **Figure 24**. SNR was statistically lower in GM compared to WM in ASE_{RF-} ($p < 0.01$) and VASO-ASE ($p < 0.01$), but not ASE_{RF+}. Both VASO-ASE ($p < 0.01$) and ASE_{RF+} ($p < 0.01$) had lower WM SNR than ASE_{RF-}, and VASO-ASE had lower WM SNR than ASE_{RF+} ($p < 0.01$). SNR and p-values are shown in **Table 8**.

Reproducibility measures were also taken for each ASE variant (**Figure 25** and **Table 8**). Reproducibility was similar between TRUST, ASE_{RF-}, and ASE_{RF+}, however reproducibility was poor for VASO-ASE.

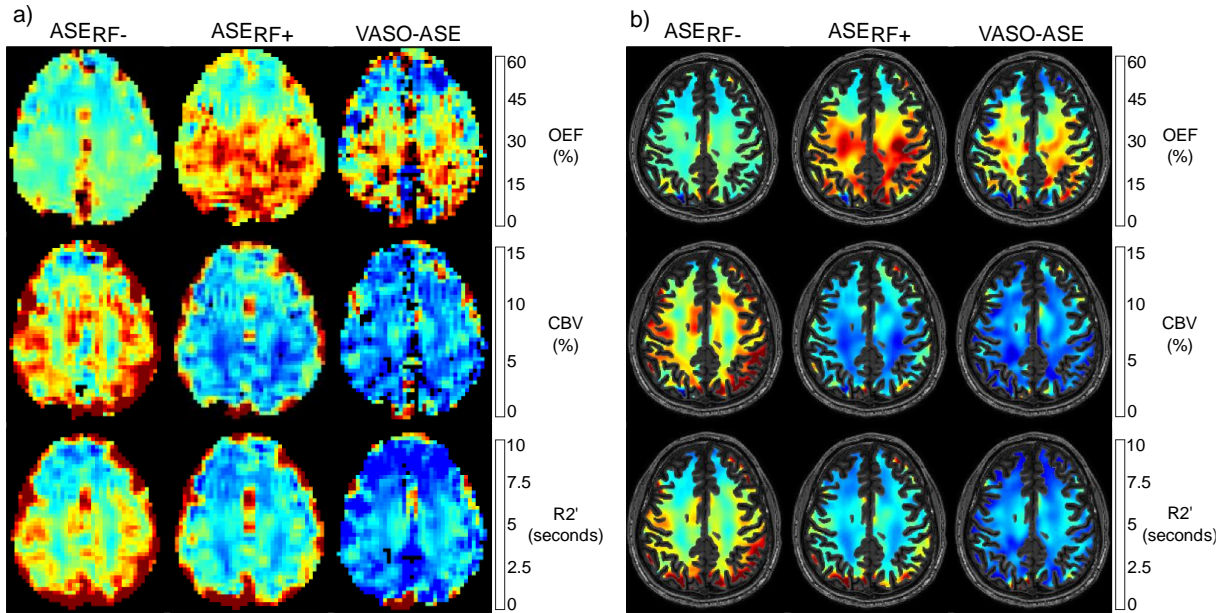


Figure 22 Representative Parameter Maps for all ASE Variants. Representative images for each physiological parameter map calculated from ASE and each ASE variant are shown in a) and b). The images as they are output from processing, and from which values in this study are extracted are shown in a). Functional images are sometimes presented, as an up-sampled, smoothed, grey matter masked version of the images from a) are shown in b).

4.4 Discussion

In this study, OEF measures from three variants of the asymmetric spin echo pulse sequence were tested for reproducibility with a better-established MRI method for measuring OEF in the brain called TRUST. ASE without a refocused second echo (ASE_{RF-}) is the most commonly implemented version of ASE, which has two echoes with no refocusing pulse between the first and second echo. A novel variant of ASE utilizing a refocusing pulse (ASE_{RF+}) is the

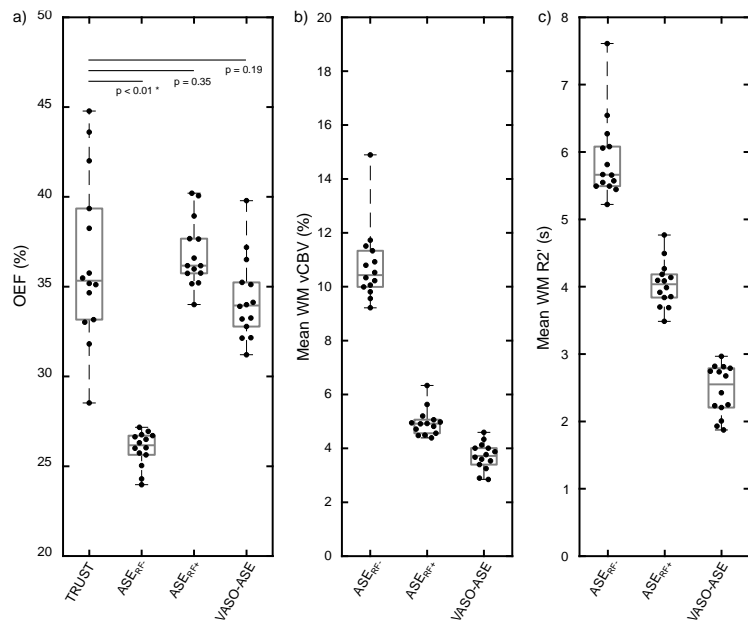


Figure 23 TRUST and ASE Variant Mean Value Group-Wise Comparisons. Mean values for each parameter map are shown in a, b, and c. OEF is shown in a), for which hypothesis testing was performed demonstrating that ASE_{RF-} produces lower OEF values ($p < 0.01$) compared to TRUST measured OEF, but ASE_{RF+} ($p = 0.035$) and VASO-ASE ($p = 0.012$) do not. Mean values for vCBV (d) and R_2' (e) are also shown, however these measurements were not part of hypothesis testing.

first novel variant of ASE tested in this study, which is identical to ASE_{RF-} except that a refocusing pulse is executed between the first and second echo. Vascular space occupancy ASE (VASO-ASE) is the second novel ASE method tested in this study, which only has one echo, however an intravascular signal nulling pre-pulse is designed to cause ASE signal to conform better to the susceptibility model assumption that intravascular signal is negligible¹⁷⁰. This study found that OEF values output by ASE_{RF+} and VASO-ASE are not significantly different from TRUST, held as a standard in this study, though ASE_{RF-} produces OEF values that are non-physiological and significantly less than that of TRUST (**Figure 23**).

OEF values are compared between each method in this study in **Figure 23 a)**, where it is demonstrated that there is not a statistical difference between TRUST-measured OEF, and mean white matter (WM) OEF from the two novel ASE variants. TRUST measured OEF has been validated in prior literature for reproducibility and accuracy^{70, 88}. The cause of improved correspondence between novel ASE methods and the TRUST method is different for each method. For ASE_{RF+}, this change is the result of the refocusing pulse. The model from Yablonskiy et al. 1994^{170, 176} which is the basis of calculating OEF, vCBV, and R₂' from ASE is a model of extravascular tissue signal, which strictly considers susceptibility effects from randomly oriented cylinders, deoxygenated blood vessels in this case. However, other sources of susceptibility in the brain exist, such as iron concentrations¹⁷¹ and field inhomogeneity¹⁷². When

	TRUST	ASE _{RF-}	ASE _{RF+}	VASO-ASE
OEF (%; mean ± St. Dev.)	36.5±4.6%	26.1±1.0%	36.8±1.9%	34.4±2.3%
OEF (%; range)	28.6 – 44.8	24.0 – 27.2	34.1 – 40.2	31.3 – 39.8
vCBV (%)	-	10.8±1.4%	5.0±0.5%	3.7±0.4%
R ₂ ' (s)	-	5.9±0.6s	4.0±0.3s	2.5±0.3s
p-Value ASE OEF vs. TRUST OEF	-	<0.01	0.35	0.19
OEF Map SNR				
SNR (WM)	-	6.3±1.5	2.7±0.5	2.1±0.3
SNR(GM)	-	4.2±1.0	2.3±0.5	1.5±0.2
p-Value OEF SNR(GM) vs. OEF SNR(WM)	-	<0.01	0.15	<0.01
OEF Reproducibility				
Intraclass Correlation Coefficient	0.98	0.91	0.89	0.61
Pearson's r	0.96	0.93	0.9	0.62
Slope	1.04	1.1	0.73	0.65

Table 8 Mean and Standard Deviation Values for TRUST and ASE Variants

the refocusing pulse is played between the first and second echo in ASE_{RF+}, these unaccounted-for sources of susceptibility may be better controlled. This effect may be the cause of the observed lower decay times, lower and more physiological measures of vCBV, as well as higher and more physiological measures of OEF. Improvements from VASO-ASE also help to account for assumptions made by the Yablonskiy model, though a different assumption. By nulling signal from deoxygenated blood, which decays rapidly compared to tissue, a similar effect is observed. Eliminating rapidly decaying venous blood signal, which is not accounted for in the model, also results in lower decay times, and may be the cause of lower and more physiological measures of vCBV, as well as higher and more physiological measures of OEF observed in VASO-ASE.

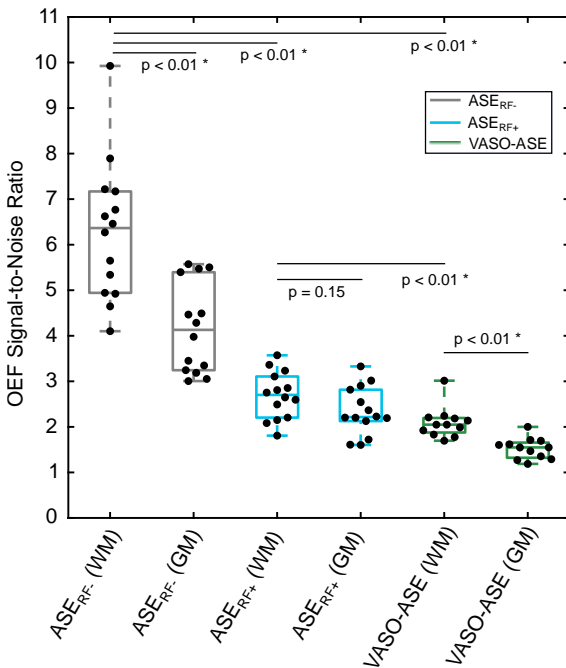


Figure 24 Group-Wise Comparisons of Signal-to-Noise Ratio in All ASE Variants. Box plots showing mean SNR values for white matter and grey matter regions calculated from oxygen extraction fraction maps. SNR was lower in GM compared to WM for ASE_{RF-} ($p > 0.01$) and VASO-ASE ($p < 0.01$), but not in ASE_{RF+} ($p = 0.15$). WM SNR was lower than ASE_{RF-} for ASE_{RF+} ($p < 0.01$) and for VASO-ASE ($p < 0.01$), and VASO-ASE OEF SNR was lower than ASE_{RF+} WM SNR ($p < 0.01$). GM = Grey Matter. WM = White Matter. Both VASO-ASE ($p < 0.01$) and ASE_{RF+} ($p < 0.01$) had lower WM SNR than ASE_{RF-}, and VASO-ASE had lower WM SNR than ASE_{RF+} ($p < 0.01$). Two participants had motion on one VASO-ASE scan, and therefore a subtraction to calculate OEF was not possible, so these participants were excluded.

SNR values displayed in **Figure 24** also warrant discussion. For ASE_{RF-} and VASO-ASE, GM SNR is significantly lower than that for WM, which is not the case for ASE_{RF+}. The reductions in GM SNR from the OEF image may be caused by several factors that make GM signal less reliable in ASE, including CSF contamination, larger vessels, less randomly oriented vessels as they converge into large veins. ASE_{RF+} doesn't display this effect, possibly because of its mechanism for controlling extraneous susceptibility effects, described in the previous paragraph. Additionally, ASE_{RF+} WM SNR was found to be lower than that of ASE_{RF-}. This may be because ASE_{RF+} reports a wider range of, and more physiological, OEF values. This wider range of values may increase noise. Finally, while the absolute values of OEF and vCBV that are measured with VASO-ASE are closer to physiological values, VASO-ASE also has the poorest reproducibility and SNR. The cause of this is likely that while the T_1 in the VASO pre-pulse is chosen to null intravascular signal

completely, extravascular signal is also affected^{167, 173}. This reduces SNR of the acquired VASO-ASE images, which can lead to poorer fitting and lower SNR values in the OEF image.

The results of this study may inform best implementation practices of ASE. This study has found that both novel variants, ASE_{RF+} and VASO-ASE, improve the physiological measurement of ASE compared to the standard ASE_{RF-} method. However, reproducibility and SNR analyses indicate that ASE_{RF+} and ASE_{RF-} outperform VASO-ASE in those regards. Additionally, slice-timing issues complicate multi-slice applications of VASO. These findings indicate that ASE_{RF+} may improve the reliability for measuring OEF and vCBV for ASE applications intended to measure these physiological parameters. However, a correlation analysis of white matter OEF values measured from ASE_{RF-} and ASE_{RF+} demonstrates a slight correlation between the methods ($r=0.58$). This correlation indicates that these two methods are reporting on similar underlying physiology, and even though ASE_{RF+} produces more physiological measures of OEF, ASE_{RF-} and previous studies which utilize it retain their value in understanding cerebral physiology.

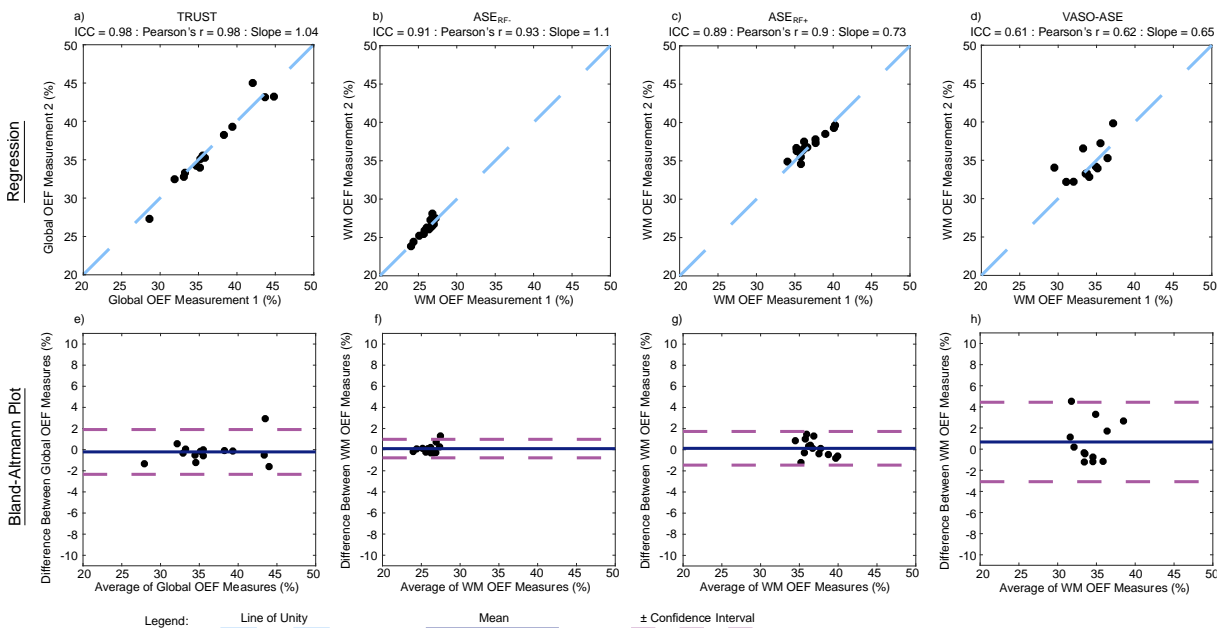


Figure 25 Reproducibility Measures of all ASE Variants and TRUST. Regression and Bland-Altman Plots for reproducibility of TRUST, ASE_{RF-}, ASE_{RF+}, and VASO-ASE. Reproducibility metrics were high for TRUST, ASE_{RF-}, and ASE_{RF+}, with Pearson's $r \geq 0.9$ for each, but not for VASO-ASE which had Pearson's $r=0.61$. Two patients had motion in one VASO-ASE scan, and were therefore excluded from reproducibility analyses.

4.4.1 Limitations

This study's findings should be regarded with several limitations. First, one existing variant of ASE which uses bipolar gradients for nulling intravascular signal was not investigated in this study¹⁶⁸. However, it is worth noting that this method increases TE, is incompletely

effective depending on b-value choice, and also can be dependent on vessel orientation and gradient scheme. A second important limitation is that while OEF values are compared between TRUST and ASE, TRUST is technically a whole-brain measure of OEF, while ASE mean values in this study were calculated in white matter. The motivation for this choice is CSF contamination, as discussed in the paragraphs above. This limitation is minor, since a meta-analysis of OEF values between grey and white matter using gold-standard PET methodology found no difference between grey and white matter OEF values¹⁷⁷. Finally, while VASO-ASE is novel and gives further insight into the relationship between intravascular signal and calculated physiological parameters of ASE, due to timing issues, this method is limited to only one echo and only one slice. Regardless, VASO-ASE was found to not be the best performing method for measuring OEF compared to ASE_{RF+}. Concerns regarding comparing the single-slice VASO-ASE method to the other multi-slice methods are addressed in **Figure 19**, which demonstrates that mean values between single-slice and multi-slice methods similar, and **Figure 26**, which demonstrates that relationships between VASO-ASE and other methods is preserved when all methods use only one echo.

4.4.2 Conclusion

This study measured three variants of the asymmetric spin echo pulse sequence, two of which are novel and were designed with the intention of bringing the acquired data in correspondence with the assumptions made by the model on which this method is founded¹⁷⁰. Hypothesis testing focused on OEF metrics, as OEF shows promise for reporting on cerebrovascular stress, though there is no well-established non-invasive

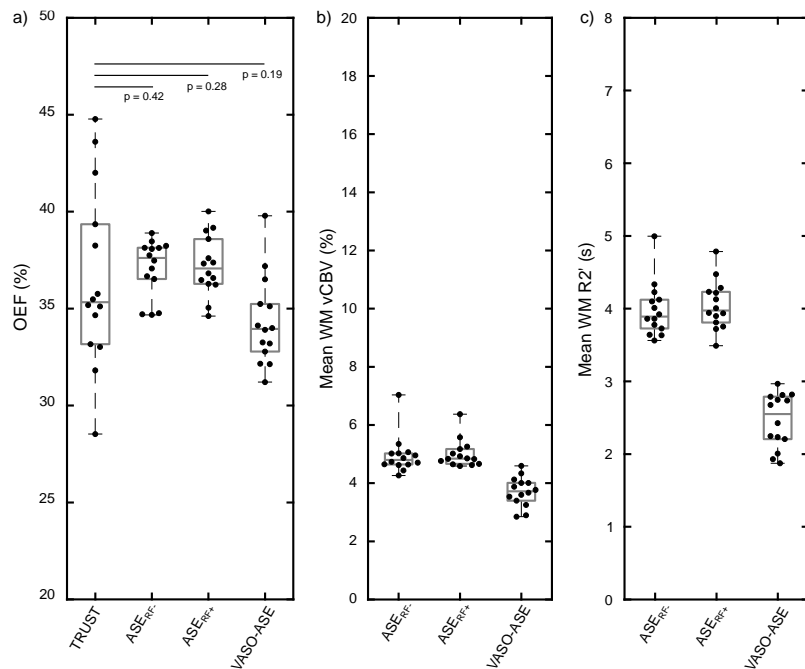


Figure 26 Physiological Parameters of TRUST and ASE Using Only the First ASE Echo. This is a similar plot as in Figure 5, however in all multi-echo acquisitions, the second echo was excluded. This was to demonstrate that differences in OEF that were identified between TRUST and the ASE methods were not due to differences in number of echoes. ASE_{RF-} and ASE_{RF+} are no longer differentiated in this analysis, because the only difference between the two is whether the second echo is refocused or not. All other identified statistical trends are preserved.

method for acquiring topographic images of OEF. We found that refocused dual-echo ASE produced more physiological values of OEF and vCBV than the standard non-refocused method, and also that it has good reproducibility metrics.

CHAPTER 5: CONCLUSION

The work in this thesis is designed to help improve methods for detecting stroke risk in patients with cerebrovascular disease and for triaging those patients for therapies. Stroke is the leading cause of adult disability, a leading cause of death, and people with cerebrovascular disease are at dramatically increased risk of stroke, more than a seven-fold increase from moyamoya disease for example. By improving our ability to assign effective therapies early in disease course, further improvement in functional imaging methodologies can reduce the frequency and severity of stroke.

Current methodology for interrogating recurrent stroke risk after a stroke or transient ischemic attack or for initial stroke risk in extremely high risk populations such as those with sickle cell disease primarily involves structural and anatomical measurements of tissue and vasculature, especially with angiography. However, if functional measurements are not made, a participant's stroke profile is not fully characterized. Functional measurements however are often difficult to perform, and may be invasive. Non-invasive MRI methods for measuring cerebral blood flow and oxygen extraction fraction are in development, however both of these continue to pose challenges that prevent adequate interpretation and acquisition in all patients. This challenge is the motivation for each of the three aims in this text.

The first aim in this work addressed the concern that cerebrovascular reactivity imaging is confounded by long response times, and as a result arterial spin labeling measured cerebral blood flow produces hyper-intensity artifacts that confound image interpretation in patients with highly-developed arterial collateral networks, moyamoya in this case. Interpreting these images is difficult, because hyper-intensity artifacts indicate collateral networks, but collateral networks can indicate both a strong compensation response to moyamoya, as well as late stages of disease. We found that novel characteristics of reactivity and blood flow images, namely reactivity delay and standard deviation of cerebral blood flow, can out-perform standard image characteristics, mean blood flow and baseline reactivity, for distinguishing stenosis severity in patients with moyamoya when input to machine learning algorithms.

The second aim was intended to improve triaging of moyamoya patients for therapies. Moyamoya is progressive, and no therapies halt or reverse the disease. Surgical

revascularization is the leading therapy for moyamoya, however not all patients have efficacious response to therapy. Since moyamoya primarily affects anterior vasculature, we hypothesized that posterior territory reactivity parameters could inform on success of revascularization surgery. We found that greater posterior territory maximum reactivity in response to a respiratory vasoactive stimulus was significantly associated with positive response to surgical intervention.

Finally, in the third aim, we developed novel variants of an MRI pulse sequence, called the asymmetric spin echo, which can be used to non-invasively measure topographic maps of oxygen extraction fraction and cerebral blood volume. We identified that novel asymmetric spin echo variants output mean white-matter oxygen extraction values that are physiological, whereas other asymmetric spin echo variants underestimate oxygen extraction fraction to non-physiological levels.

Stroke treatment has improved over the last 30 years, with major milestones achieved via large clinical trials such as the NASCET, CREST, and SAMMPRIS trials. The introduction of tPA drugs for treatment of acute stroke has also improved outcomes. However, treatment for non-atherosclerotic conditions like moyamoya lags behind the recent developments in stroke treatment. Moyamoya treatment first involves the administration of blood thinners for preventing microthrombi, however revascularization surgery remains the most common treatment for moyamoya. Unfortunately, a lack of randomized clinical trials results in treatment decisions for moyamoya being subjective, and outcomes are varied, as there are not standardized criteria for triaging patients with moyamoya for surgery. Outcomes in moyamoya may be improved by improving methods for interrogating moyamoya functional status.

Functional imaging methods with MRI are generally accessible and have demonstrated applicability for interpreting stroke risk, as well as acting as biomarkers for response to therapies. However functional imaging methods are often confounded in cases of abnormal physiology. Cerebral blood flow measurements with MRI in cerebrovascular disease are complicated by long arterial transit times, which preclude uniform quantification of CBF. Cerebral reactivity measurements, while are impacted less by abnormal physiology, do not have a standardized measurement protocol. External vasoactive stimuli are generally implemented, although protocols using endogenous stimuli are being developed. External stimuli can be either pharmacologic agents, such as acetazolamide, or respiratory stimuli of several varieties incorporating carbon dioxide. Additionally, the flow rate of respiratory stimuli is contentious as well. Implementation of functional imaging modalities would benefit greatly from a greater

understanding of the effects abnormal physiology has on blood flow, and from standardization of measurement protocol in the case of reactivity.

I believe that the future of moyamoya treatment will comprise further development of functional imaging techniques as described above, as well as an improved understanding of moyamoya progression and compensation. The origin of moyamoya is unclear. We know that it is genetically linked, occurs more frequently in females, and can be idiopathic or syndromic, but the risk factors are complicated. Additionally, outcomes in moyamoya are often determined by angiogenic response to stenosis, however the factors which determine this response are also unclear. Circulating and genetic factors have been identified which interact with one another, however certainty regarding these variables eludes us. As angiogenic response is important for moyamoya outcome, angiogenic factors which underlie this response are critical for developing further treatments and triaging of moyamoya. One important component regarding the future of moyamoya treatment is the development and quantification of genetic and circulating factors, which contribute to angiogenesis.

A study which I foresee elucidating large parts of moyamoya treatment is one in which all of these factors are considered in parallel. Blood tests should be performed on each participant to measure circulating factors, genetic tests should also be performed which will help to quantify identified genetic components of moyamoya. Participants should receive functional and angiographic imaging pre- and post- surgically, which will help to elucidate the role that functional, genetic, and circulating parameters have on moyamoya outcome to interventions. Ideally, this will also inform on the parameters that determine neovascularization, and further pharmacologic research can help to induce revascularization responses following surgical intervention.

The completion of each of the aims in this work contributes to the body of literature, and available methods for, non-invasive assessment of tissue function. This work also demonstrates that functional tissue parameters provide information on tissue-level compensation for cerebrovascular impairment that anatomical information does not provide on its own. These methods, when refined through further research, and the consideration of functional information alongside anatomical information, can help to improve stroke prevention and outcomes, as well as triaging for intervention and therapies.

REFERENCES

1. Donahue MJ, Achten E, Cogswell PM, et al. Consensus statement on current and emerging methods for the diagnosis and evaluation of cerebrovascular disease. *J Cereb Blood Flow Metab.* 2017; 271678X17721830.
2. Feigin VL. Stroke epidemiology in the developing world. *Lancet.* 2005; 365: 2160-1.
3. Feigin V and Hoorn SV. How to study stroke incidence. *Lancet.* 2004; 363: 1920.
4. Bos MJ, Koudstaal PJ, Hofman A and Ikram MA. Modifiable etiological factors and the burden of stroke from the Rotterdam study: a population-based cohort study. *PLoS Med.* 2014; 11: e1001634.
5. Ferguson GG, Eliasziw M, Barr HW, et al. The North American Symptomatic Carotid Endarterectomy Trial : surgical results in 1415 patients. *Stroke.* 1999; 30: 1751-8.
6. Chimowitz MI, Lynn MJ, Derdeyn CP, et al. Stenting versus aggressive medical therapy for intracranial arterial stenosis. *N Engl J Med.* 2011; 365: 993-1003.
7. DeBeer T, Jordan LC, Lee CA, et al. Evidence of transfusion-induced reductions in cerebral capillary shunting in sickle cell disease. *Am J Hematol.* 2020; 95: E228-E30.
8. Guilliams KP, Fields ME, Ragan DK, et al. Red cell exchange transfusions lower cerebral blood flow and oxygen extraction fraction in pediatric sickle cell anemia. *Blood.* 2018; 131: 1012-21.
9. Donahue MJ, Strother MK, Lindsey KP, Hocke LM, Tong Y and Frederick BD. Time delay processing of hypercapnic fMRI allows quantitative parameterization of cerebrovascular reactivity and blood flow delays. *J Cereb Blood Flow Metab.* 2016; 36: 1767-79.
10. Liebeskind DS, Cotsonis GA, Saver JL, et al. Collaterals dramatically alter stroke risk in intracranial atherosclerosis. *Ann Neurol.* 2011; 69: 963-74.
11. Borghammer P, Cumming P, Ostergaard K, et al. Cerebral oxygen metabolism in patients with early Parkinson's disease. *J Neurol Sci.* 2012; 313: 123-8.
12. Powers WJ, Videen TO, Markham J, Black KJ, Golchin N and Perlmutter JS. Cerebral mitochondrial metabolism in early Parkinson's disease. *J Cereb Blood Flow Metab.* 2008; 28: 1754-60.
13. Donahue MJ, Dethrage LM, Faraco CC, et al. Routine clinical evaluation of cerebrovascular reserve capacity using carbogen in patients with intracranial stenosis. *Stroke.* 2014; 45: 2335-41.
14. Qi Y, Liu P, Lin Z, Lu H and Wang X. Hemodynamic and Metabolic Assessment of Neonates With Punctate White Matter Lesions Using Phase-Contrast MRI and T2-Relaxation-Under-Spin-Tagging (TRUST) MRI. *Front Physiol.* 2018; 9: 233.

15. Jordan LC, Gindville MC, Scott AO, et al. Non-invasive imaging of oxygen extraction fraction in adults with sickle cell anaemia. *Brain*. 2016; 139: 738-50.
16. Derdeyn CP, Videen TO, Grubb RL, Jr. and Powers WJ. Comparison of PET oxygen extraction fraction methods for the prediction of stroke risk. *J Nucl Med*. 2001; 42: 1195-7.
17. Iwama T, Akiyama Y, Morimoto M, Kojima A and Hayashida K. Comparison of positron emission tomography study results of cerebral hemodynamics in patients with bleeding- and ischemic-type moyamoya disease. *Neurosurg Focus*. 1998; 5: e3.
18. Grubb RL, Jr., Derdeyn CP, Fritsch SM, et al. Importance of hemodynamic factors in the prognosis of symptomatic carotid occlusion. *JAMA*. 1998; 280: 1055-60.
19. Watchmaker JM, Frederick BD, Fusco MR, et al. Clinical Use of Cerebrovascular Compliance Imaging to Evaluate Revascularization in Patients With Moyamoya. *Neurosurgery*. 2018.
20. Baron JC, Rougemont D, Lebrun-Grandie P, et al. Local Cerebral Blood Flow and Oxygen Consumption in Evolving Irreversible Ischemic Infarction Heiss WD, Phelps ME (eds) *Positron Emission Tomography of the Brain Springer, Berlin, Heidelberg*. 1983.
21. Fan AP, Jahanian H, Holdsworth SJ and Zaharchuk G. Comparison of cerebral blood flow measurement with [15O]-water positron emission tomography and arterial spin labeling magnetic resonance imaging: A systematic review. *J Cereb Blood Flow Metab*. 2016; 36: 842-61.
22. Ter-Pogossian MM, Eichling JO, Davis DO and Welch MJ. The measure in vivo of regional cerebral oxygen utilization by means of oxyhemoglobin labeled with radioactive oxygen-15. *J Clin Invest*. 1970; 49: 381-91.
23. Guey S, Tournier-Lasserre E, Herve D and Kossorotoff M. Moyamoya disease and syndromes: from genetics to clinical management. *Appl Clin Genet*. 2015; 8: 49-68.
24. Scott RM and Smith ER. Moyamoya disease and moyamoya syndrome. *N Engl J Med*. 2009; 360: 1226-37.
25. Phi JH, Wang KC, Lee JY and Kim SK. Moyamoya Syndrome: A Window of Moyamoya Disease. *J Korean Neurosurg Soc*. 2015; 57: 408-14.
26. Yousaf T, Dervenoulas G and Politis M. Advances in MRI Methodology. *Int Rev Neurobiol*. 2018; 141: 31-76.
27. Lameka K, Farwell MD and Ichise M. Positron Emission Tomography. *Handb Clin Neurol*. 2016; 135: 209-27.
28. Huang B, Law MW and Khong PL. Whole-body PET/CT scanning: estimation of radiation dose and cancer risk. *Radiology*. 2009; 251: 166-74.

29. Fleischmann D, Chin AS, Molvin L, Wang J and Hallett R. Computed Tomography Angiography: A Review and Technical Update. *Radiol Clin North Am.* 2016; 54: 1-12.
30. Mistretta CA and Grist TM. X-ray digital subtraction angiography to magnetic resonance-digital subtraction angiography using three-dimensional TRICKS. Historical perspective and computer simulations: a review. *Invest Radiol.* 1998; 33: 496-505.
31. Ell PJ. Single photon emission computed tomography (SPET) of the brain. *J Neurosci Methods.* 1990; 34: 207-17.
32. Schafer ME. Fundamentals of High-Resolution Ultrasound in Breast Implant Screening for Plastic Surgeons. *Clin Plast Surg.* 2021; 48: 59-69.
33. Chaplin V and Caskey CF. Multi-focal HIFU reduces cavitation in mild-hyperthermia. *J Ther Ultrasound.* 2017; 5: 12.
34. Adams R, McKie V, Nichols F, et al. The use of transcranial ultrasonography to predict stroke in sickle cell disease. *N Engl J Med.* 1992; 326: 605-10.
35. Lopez-Lorente AI and Mizaikoff B. Mid-infrared spectroscopy for protein analysis: potential and challenges. *Anal Bioanal Chem.* 2016; 408: 2875-89.
36. Saver JL. Time is brain--quantified. *Stroke.* 2006; 37: 263-6.
37. Writing Group M, Mozaffarian D, Benjamin EJ, et al. Heart Disease and Stroke Statistics-2016 Update: A Report From the American Heart Association. *Circulation.* 2016; 133: e38-360.
38. Donnan GA, Fisher M, Macleod M and Davis SM. Stroke. *Lancet.* 2008; 371: 1612-23.
39. Schwamm LH, Wu O, Song SS, et al. Intravenous thrombolysis in unwitnessed stroke onset: MR WITNESS trial results. *Ann Neurol.* 2018; 83: 980-93.
40. Albers GW, Lansberg MG, Kemp S, et al. A multicenter randomized controlled trial of endovascular therapy following imaging evaluation for ischemic stroke (DEFUSE 3). *Int J Stroke.* 2017; 12: 896-905.
41. Prabhakaran S, Ruff I and Bernstein RA. Acute stroke intervention: a systematic review. *JAMA.* 2015; 313: 1451-62.
42. Clinical alert: benefit of carotid endarterectomy for patients with high-grade stenosis of the internal carotid artery. National Institute of Neurological Disorders and Stroke Stroke and Trauma Division. North American Symptomatic Carotid Endarterectomy Trial (NASCET) investigators. *Stroke.* 1991; 22: 816-7.
43. Brott TG, Howard G, Roubin GS, et al. Long-Term Results of Stenting versus Endarterectomy for Carotid-Artery Stenosis. *N Engl J Med.* 2016; 374: 1021-31.

44. Hallemeier CL, Rich KM, Grubb RL, Jr., et al. Clinical features and outcome in North American adults with moyamoya phenomenon. *Stroke*. 2006; 37: 1490-6.
45. Kassim AA and DeBaun MR. Sick cell disease, vasculopathy, and therapeutics. *Annu Rev Med*. 2013; 64: 451-66.
46. Juttukonda MR, Donahue MJ, Waddle SL, et al. Reduced oxygen extraction efficiency in sickle cell anemia patients with evidence of cerebral capillary shunting. *J Cereb Blood Flow Metab*. 2021; 41: 546-60.
47. Ferreira LK, Rondina JM, Kubo R, et al. Support vector machine-based classification of neuroimages in Alzheimer's disease: direct comparison of FDG-PET, rCBF-SPECT and MRI data acquired from the same individuals. *Rev Bras Psiquiatr*. 2017: 0.
48. Malatesha G, Singh NK, Bharija A, Rehani B and Goel A. Comparison of arterial and venous pH, bicarbonate, PCO₂ and PO₂ in initial emergency department assessment. *Emerg Med J*. 2007; 24: 569-71.
49. Powers WJ. Cerebral hemodynamics in ischemic cerebrovascular disease. *Ann Neurol*. 1991; 29: 231-40.
50. Ni WW, Christen T, Rosenberg J, Zun Z, Moseley ME and Zaharchuk G. Imaging of cerebrovascular reserve and oxygenation in Moyamoya disease. *J Cereb Blood Flow Metab*. 2017; 37: 1213-22.
51. Kawashima M, Noguchi T, Takase Y, Ootsuka T, Kido N and Matsushima T. Unilateral hemispheric proliferation of ivy sign on fluid-attenuated inversion recovery images in moyamoya disease correlates highly with ipsilateral hemispheric decrease of cerebrovascular reserve. *AJNR Am J Neuroradiol*. 2009; 30: 1709-16.
52. Brown RW, Cheng Y-CN, Haacke EM, Thompson MR and Venkatesan R. *Magnetic Resonance Imaging: Physical Principles and Sequence Design, 2nd Edition*. Wiley-Blackwell, 2014.
53. Crescenzi R, Donahue PMC, Petersen KJ, et al. Upper and Lower Extremity Measurement of Tissue Sodium and Fat Content in Patients with Lipedema. *Obesity (Silver Spring)*. 2020; 28: 907-15.
54. Petersen KJ, Garza M, Donahue PMC, et al. Neuroimaging of Cerebral Blood Flow and Sodium in Women with Lipedema. *Obesity (Silver Spring)*. 2020; 28: 1292-300.
55. van Zijl PC and Yadav NN. Chemical exchange saturation transfer (CEST): what is in a name and what isn't? *Magn Reson Med*. 2011; 65: 927-48.

56. Brant-Zawadzki M, Gillan GD and Nitz WR. MP RAGE: a three-dimensional, T1-weighted, gradient-echo sequence--initial experience in the brain. *Radiology*. 1992; 182: 769-75.
57. Saranathan M, Worters PW, Rettmann DW, Winegar B and Becker J. Physics for clinicians: Fluid-attenuated inversion recovery (FLAIR) and double inversion recovery (DIR) Imaging. *J Magn Reson Imaging*. 2017; 46: 1590-600.
58. Lu H, Nagae-Poetscher LM, Golay X, Lin D, Pomper M and van Zijl PC. Routine clinical brain MRI sequences for use at 3.0 Tesla. *J Magn Reson Imaging*. 2005; 22: 13-22.
59. Brant-Zawadzki M, Atkinson D, Detrick M, Bradley WG and Scidmore G. Fluid-attenuated inversion recovery (FLAIR) for assessment of cerebral infarction. Initial clinical experience in 50 patients. *Stroke*. 1996; 27: 1187-91.
60. Filippi M and Agosta F. Diffusion tensor imaging and functional MRI. *Handb Clin Neurol*. 2016; 136: 1065-87.
61. Wymer DT, Patel KP, Burke WF, 3rd and Bhatia VK. Phase-Contrast MRI: Physics, Techniques, and Clinical Applications. *Radiographics*. 2020; 40: 122-40.
62. Roy TL, Forbes TL, Dueck AD and Wright GA. MRI for peripheral artery disease: Introductory physics for vascular physicians. *Vasc Med*. 2018; 23: 153-62.
63. Alsop DC, Detre JA, Golay X, et al. Recommended implementation of arterial spin-labeled perfusion MRI for clinical applications: A consensus of the ISMRM perfusion study group and the European consortium for ASL in dementia. *Magn Reson Med*. 2015; 73: 102-16.
64. Williams DS, Detre JA, Leigh JS and Koretsky AP. Magnetic resonance imaging of perfusion using spin inversion of arterial water. *Proc Natl Acad Sci U S A*. 1992; 89: 212-6.
65. Wang J, Alsop DC, Li L, et al. Comparison of quantitative perfusion imaging using arterial spin labeling at 1.5 and 4.0 Tesla. *Magn Reson Med*. 2002; 48: 242-54.
66. Faraco CC, Strother MK, Dethrage LM, et al. Dual echo vessel-encoded ASL for simultaneous BOLD and CBF reactivity assessment in patients with ischemic cerebrovascular disease. *Magn Reson Med*. 2015; 73: 1579-92.
67. Lu H, Clingman C, Golay X and van Zijl PC. Determining the longitudinal relaxation time (T1) of blood at 3.0 Tesla. *Magn Reson Med*. 2004; 52: 679-82.
68. Silvennoinen MJ, Clingman CS, Golay X, Kauppinen RA and van Zijl PC. Comparison of the dependence of blood R2 and R2* on oxygen saturation at 1.5 and 4.7 Tesla. *Magn Reson Med*. 2003; 49: 47-60.
69. Lu H and Ge Y. Quantitative evaluation of oxygenation in venous vessels using T2-Relaxation-Under-Spin-Tagging MRI. *Magn Reson Med*. 2008; 60: 357-63.

70. Lu H, Xu F, Grgac K, Liu P, Qin Q and van Zijl P. Calibration and validation of TRUST MRI for the estimation of cerebral blood oxygenation. *Magn Reson Med.* 2012; 67: 42-9.
71. Hartog C and Bloos F. Venous oxygen saturation. *Best Pract Res Clin Anaesthesiol.* 2014; 28: 419-28.
72. An H and Lin W. Quantitative measurements of cerebral blood oxygen saturation using magnetic resonance imaging. *J Cereb Blood Flow Metab.* 2000; 20: 1225-36.
73. Gauthier CJ and Hoge RD. Magnetic resonance imaging of resting OEF and CMRO(2) using a generalized calibration model for hypercapnia and hyperoxia. *Neuroimage.* 2012; 60: 1212-25.
74. Bulte DP, Kelly M, Germuska M, et al. Quantitative measurement of cerebral physiology using respiratory-calibrated MRI. *Neuroimage.* 2012; 60: 582-91.
75. He X and Yablonskiy DA. Quantitative BOLD: mapping of human cerebral deoxygenated blood volume and oxygen extraction fraction: default state. *Magn Reson Med.* 2007; 57: 115-26.
76. Stone AJ, Holland NC, Berman AJL and Blockley NP. Simulations of the effect of diffusion on asymmetric spin echo based quantitative BOLD: An investigation of the origin of deoxygenated blood volume overestimation. *Neuroimage.* 2019; 201: 116035.
77. Donahue MJ, Hoogduin H, van Zijl PC, Jezzard P, Luijten PR and Hendrikse J. Blood oxygenation level-dependent (BOLD) total and extravascular signal changes and DeltaR2* in human visual cortex at 1.5, 3.0 and 7.0 T. *NMR Biomed.* 2011; 24: 25-34.
78. Lin W and Powers WJ. Oxygen metabolism in acute ischemic stroke. *J Cereb Blood Flow Metab.* 2018; 38: 1481-99.
79. Powers WJ, Grubb RL, Jr., Darriet D and Raichle ME. Cerebral blood flow and cerebral metabolic rate of oxygen requirements for cerebral function and viability in humans. *J Cereb Blood Flow Metab.* 1985; 5: 600-8.
80. Wang DJ, Alger JR, Qiao JX, et al. Multi-delay multi-parametric arterial spin-labeled perfusion MRI in acute ischemic stroke - Comparison with dynamic susceptibility contrast enhanced perfusion imaging. *Neuroimage Clin.* 2013; 3: 1-7.
81. Zaharchuk G, El Mogy IS, Fischbein NJ and Albers GW. Comparison of arterial spin labeling and bolus perfusion-weighted imaging for detecting mismatch in acute stroke. *Stroke.* 2012; 43: 1843-8.
82. Silvestrini M, Vernieri F, Pasqualetti P, et al. Impaired cerebral vasoreactivity and risk of stroke in patients with asymptomatic carotid artery stenosis. *JAMA.* 2000; 283: 2122-7.

83. Bokkers RP, van Osch MJ, van der Worp HB, de Borst GJ, Mali WP and Hendrikse J. Symptomatic carotid artery stenosis: impairment of cerebral autoregulation measured at the brain tissue level with arterial spin-labeling MR imaging. *Radiology*. 2010; 256: 201-8.
84. Kitajima M, Hirai T, Shigematsu Y, et al. Assessment of cerebral perfusion from bypass arteries using magnetic resonance regional perfusion imaging in patients with moyamoya disease. *Jpn J Radiol*. 2010; 28: 746-53.
85. Wise RG, Harris AD, Stone AJ and Murphy K. Measurement of OEF and absolute CMRO₂: MRI-based methods using interleaved and combined hypercapnia and hyperoxia. *Neuroimage*. 2013; 83: 135-47.
86. Derdeyn CP, Videen TO, Yundt KD, et al. Variability of cerebral blood volume and oxygen extraction: stages of cerebral haemodynamic impairment revisited. *Brain*. 2002; 125: 595-607.
87. Watchmaker JM, Juttukonda MR, Davis LT, et al. Hemodynamic mechanisms underlying elevated oxygen extraction fraction (OEF) in moyamoya and sickle cell anemia patients. *J Cereb Blood Flow Metab*. 2016: 271678X16682509.
88. Bush A, Borzage M, Detterich J, et al. Empirical model of human blood transverse relaxation at 3 T improves MRI T₂ oximetry. *Magn Reson Med*. 2017; 77: 2364-71.
89. Liu P, Li Y, Pinho M, Park DC, Welch BG and Lu H. Cerebrovascular reactivity mapping without gas challenges. *Neuroimage*. 2017; 146: 320-6.
90. Kang KH, Kim HS and Kim SY. Quantitative cerebrovascular reserve measured by acetazolamide-challenged dynamic CT perfusion in ischemic adult Moyamoya disease: initial experience with angiographic correlation. *AJNR Am J Neuroradiol*. 2008; 29: 1487-93.
91. Liu P, Xu C, Lin Z, et al. Cerebrovascular reactivity mapping using intermittent breath modulation. *Neuroimage*. 2020; 215: 116787.
92. Malte H and Lykkeboe G. The Bohr/Haldane effect: a model-based uncovering of the full extent of its impact on O₂ delivery to and CO₂ removal from tissues. *J Appl Physiol (1985)*. 2018; 125: 916-22.
93. Bright MG, Bulte DP, Jezard P and Duyn JH. Characterization of regional heterogeneity in cerebrovascular reactivity dynamics using novel hypocapnia task and BOLD fMRI. *Neuroimage*. 2009; 48: 166-75.
94. Thomas BP, Liu P, Park DC, van Osch MJ and Lu H. Cerebrovascular reactivity in the brain white matter: magnitude, temporal characteristics, and age effects. *J Cereb Blood Flow Metab*. 2014; 34: 242-7.

95. Liu P, Liu G, Pinho MC, et al. Cerebrovascular Reactivity Mapping Using Resting-State BOLD Functional MRI in Healthy Adults and Patients with Moyamoya Disease. *Radiology*. 2021; 299: 419-25.
96. Juttukonda MR, Davis LT, Lants SK, et al. A Prospective, Longitudinal Magnetic Resonance Imaging Evaluation of Cerebrovascular Reactivity and Infarct Development in Patients With Intracranial Stenosis. *J Magn Reson Imaging*. 2021; 54: 912-22.
97. Roach BA, Donahue MJ, Davis LT, et al. Interrogating the Functional Correlates of Collateralization in Patients with Intracranial Stenosis Using Multimodal Hemodynamic Imaging. *AJNR Am J Neuroradiol*. 2016; 37: 1132-8.
98. Zhou J, Wilson DA, Ulatowski JA, Traystman RJ and van Zijl PC. Two-compartment exchange model for perfusion quantification using arterial spin tagging. *J Cereb Blood Flow Metab*. 2001; 21: 440-55.
99. Aslan S, Xu F, Wang PL, et al. Estimation of labeling efficiency in pseudocontinuous arterial spin labeling. *Magn Reson Med*. 2010; 63: 765-71.
100. Chen Z, Zhang X, Yuan C, Zhao X and van Osch MJP. Measuring the labeling efficiency of pseudocontinuous arterial spin labeling. *Magn Reson Med*. 2017; 77: 1841-52.
101. Juttukonda MR, Jordan LC, Gindville MC, et al. Cerebral hemodynamics and pseudo-continuous arterial spin labeling considerations in adults with sickle cell anemia. *NMR Biomed*. 2017; 30.
102. Fan AP, Guo J, Khalighi MM, et al. Long-Delay Arterial Spin Labeling Provides More Accurate Cerebral Blood Flow Measurements in Moyamoya Patients: A Simultaneous Positron Emission Tomography/MRI Study. *Stroke*. 2017; 48: 2441-9.
103. Woolrich MW, Jbabdi S, Patenaude B, et al. Bayesian analysis of neuroimaging data in FSL. *Neuroimage*. 2009; 45: S173-86.
104. Collij LE, Heeman F, Kuijjer JP, et al. Application of Machine Learning to Arterial Spin Labeling in Mild Cognitive Impairment and Alzheimer Disease. *Radiology*. 2016; 281: 865-75.
105. Baldi P, Brunak S, Chauvin Y, Andersen CA and Nielsen H. Assessing the accuracy of prediction algorithms for classification: an overview. *Bioinformatics*. 2000; 16: 412-24.
106. Gao R, Tang Y, Xu K, et al. Deep Multi-path Network Integrating Incomplete Biomarker and Chest CT Data for Evaluating Lung Cancer Risk. *Proc SPIE Int Soc Opt Eng*. 2021; 11596.
107. Grovik E, Yi D, Iv M, Tong E, Rubin D and Zaharchuk G. Deep learning enables automatic detection and segmentation of brain metastases on multisequence MRI. *J Magn Reson Imaging*. 2020; 51: 175-82.

108. Lee HH, Tang Y, Bao S, Abramson RG, Huo Y and Landman BA. Rap-Net: Coarse-to-Fine Multi-Organ Segmentation with Single Random Anatomical Prior. *Proc IEEE Int Symp Biomed Imaging*. 2021; 2021: 1491-4.
109. Gao R, Tang Y, Khan MS, et al. Cancer Risk Estimation Combining Lung Screening CT with Clinical Data Elements. *Radiol Artif Intell*. 2021; 3: e210032.
110. Orru G, Pettersson-Yeo W, Marquand AF, Sartori G and Mechelli A. Using Support Vector Machine to identify imaging biomarkers of neurological and psychiatric disease: a critical review. *Neurosci Biobehav Rev*. 2012; 36: 1140-52.
111. Pereira S, Pinto A, Alves V and Silva CA. Brain Tumor Segmentation Using Convolutional Neural Networks in MRI Images. *IEEE Trans Med Imaging*. 2016; 35: 1240-51.
112. Oliveira PP, Jr., Nitrini R, Busatto G, Buchpiguel C, Sato JR and Amaro E, Jr. Use of SVM methods with surface-based cortical and volumetric subcortical measurements to detect Alzheimer's disease. *J Alzheimers Dis*. 2010; 19: 1263-72.
113. Yoon J, Gong E, Chatnuntawech I, et al. Quantitative susceptibility mapping using deep neural network: QSMnet. *Neuroimage*. 2018; 179: 199-206.
114. Lebedev AV, Westman E, Van Westen GJ, et al. Random Forest ensembles for detection and prediction of Alzheimer's disease with a good between-cohort robustness. *Neuroimage Clin*. 2014; 6: 115-25.
115. Akselrod-Ballin A, Galun M, Gomori JM, et al. Automatic segmentation and classification of multiple sclerosis in multichannel MRI. *IEEE Trans Biomed Eng*. 2009; 56: 2461-9.
116. Cortes C and Vapnik V. Support-Vector Networks. *Machine Learning*. 1995; 20.
117. Donahue MJ, Ayad M, Moore R, et al. Relationships between hypercarbic reactivity, cerebral blood flow, and arterial circulation times in patients with moyamoya disease. *J Magn Reson Imaging*. 2013; 38: 1129-39.
118. Dai W, Garcia D, de Bazelaire C and Alsop DC. Continuous flow-driven inversion for arterial spin labeling using pulsed radio frequency and gradient fields. *Magn Reson Med*. 2008; 60: 1488-97.
119. Faraco CC, Strother MK, Siero JC, et al. The cumulative influence of hyperoxia and hypercapnia on blood oxygenation and $R^*(2)$. *J Cereb Blood Flow Metab*. 2015; 35: 2032-42.
120. Greve DN and Fischl B. Accurate and robust brain image alignment using boundary-based registration. *Neuroimage*. 2009; 48: 63-72.
121. Mutsaerts HJ, Petr J, Vaclavu L, et al. The spatial coefficient of variation in arterial spin labeling cerebral blood flow images. *J Cereb Blood Flow Metab*. 2017; 37: 3184-92.

122. Zaharchuk G, Do HM, Marks MP, Rosenberg J, Moseley ME and Steinberg GK. Arterial spin-labeling MRI can identify the presence and intensity of collateral perfusion in patients with moyamoya disease. *Stroke*. 2011; 42: 2485-91.
123. Hendrikse J, van der Grond J, Lu H, van Zijl PC and Golay X. Flow territory mapping of the cerebral arteries with regional perfusion MRI. *Stroke*. 2004; 35: 882-7.
124. Donahue MJ, Strother MK and Hendrikse J. Novel MRI approaches for assessing cerebral hemodynamics in ischemic cerebrovascular disease. *Stroke*. 2012; 43: 903-15.
125. Fan RE, Chen PH and Lin CJ. Working set selection using second order information for training support vector machines. *J Mach Learn Res*. 2005; 6: 1889-918.
126. Youden WJ. Index for rating diagnostic tests. *Cancer*. 1950; 3: 32-5.
127. Liu X. Classification accuracy and cut point selection. *Stat Med*. 2012; 31: 2676-86.
128. Fluss R, Faraggi D and Reiser B. Estimation of the Youden Index and its associated cutoff point. *Biom J*. 2005; 47: 458-72.
129. Kohavi R. A Study of Cross-Validation and Bootstrap for Accuracy Estimation and Model Selection. *International Joint Conference on Artificial Intelligence*. 1995.
130. Ibaraki M, Nakamura K, Toyoshima H, et al. Spatial coefficient of variation in pseudo-continuous arterial spin labeling cerebral blood flow images as a hemodynamic measure for cerebrovascular steno-occlusive disease: A comparative (15)O positron emission tomography study. *J Cereb Blood Flow Metab*. 2018: 271678X18781667.
131. Woods JG, Chappell MA and Okell TW. A general framework for optimizing arterial spin labeling MRI experiments. *Magn Reson Med*. 2018.
132. Liu P, Welch BG, Thomas BP, et al. Sensitivity and specificity of cerebrovascular reactivity in predicting surgical decisions in Moyamoya patients. *International Society for Magnetic Resonance in Medicine*. 2017; Paris 2018.
133. Asadi H, Dowling R, Yan B and Mitchell P. Machine learning for outcome prediction of acute ischemic stroke post intra-arterial therapy. *PLoS One*. 2014; 9: e88225.
134. Burges C. A Tutorial on Support Vector Machines for Pattern Recognition. *Data Mining and Knowledge Discovery*. 1998; 2: 121-67.
135. LeCun Y, Bengio Y and Hinton G. Deep learning. *Nature*. 2015; 521: 436-44.
136. Niu Y, Gong E, Xu J, Thamm T, Pauly J and Zaharchuk G. Improved Prediction of the Final Infarct from Acute Stroke Neuroimaging Using Deep Learning. *International Society for Magnetic Resonance in Medicine*. 2017; Paris 2018.
137. Zhang W, Li R, Deng H, et al. Deep convolutional neural networks for multi-modality iso-intense infant brain image segmentation. *Neuroimage*. 2015; 108: 214-24.

138. Ho TK. Random Decision Forests. *Proceedings of 3rd International Conference on Document Analysis and Recognition*. 1995; 1: 278-82.
139. Mitra J, Bourgeat P, Fripp J, et al. Lesion segmentation from multimodal MRI using random forest following ischemic stroke. *Neuroimage*. 2014; 98: 324-35.
140. Pan H, Shi W, Li H, Zhang H, Li C and Wang Y. Clinical Prediction of Surgical Revascularization Outcome in Moyamoya Disease Via Transcranial Color Sonography. *J Stroke Cerebrovasc Dis*. 2020; 29: 105154.
141. Waddle SL, Juttukonda MR, Lants SK, et al. Classifying intracranial stenosis disease severity from functional MRI data using machine learning. *J Cereb Blood Flow Metab*. 2020; 40: 705-19.
142. Juttukonda MR, Davis LT, Lants SK, et al. A Prospective, Longitudinal Magnetic Resonance Imaging Evaluation of Cerebrovascular Reactivity and Infarct Development in Patients With Intracranial Stenosis. *J Magn Reson Imaging*. 2021.
143. Blockley NP, Griffeth VE, Simon AB, Dubowitz DJ and Buxton RB. Calibrating the BOLD response without administering gases: comparison of hypercapnia calibration with calibration using an asymmetric spin echo. *NeuroImage*. 2015; 104: 423-9.
144. Bhogal AA, De Vis JB, Siero JCW, et al. The BOLD cerebrovascular reactivity response to progressive hypercapnia in young and elderly. *Neuroimage*. 2016; 139: 94-102.
145. Lee M, Zaharchuk G, Guzman R, Achrol A, Bell-Stephens T and Steinberg GK. Quantitative hemodynamic studies in moyamoya disease: a review. *Neurosurgical focus*. 2009; 26: E5.
146. Vernieri F, Pasqualetti P, Matteis M, et al. Effect of collateral blood flow and cerebral vasomotor reactivity on the outcome of carotid artery occlusion. *Stroke*. 2001; 32: 1552-8.
147. Strother MK, Anderson MD, Singer RJ, et al. Cerebrovascular collaterals correlate with disease severity in adult North American patients with Moyamoya disease. *AJNR Am J Neuroradiol*. 2014; 35: 1318-24.
148. Fang YC, Wei LF, Hu CJ and Tu YK. Pathological Circulating Factors in Moyamoya Disease. *Int J Mol Sci*. 2021; 22.
149. Mikami T, Suzuki H, Komatsu K and Mikuni N. Influence of Inflammatory Disease on the Pathophysiology of Moyamoya Disease and Quasi-moyamoya Disease. *Neurol Med Chir (Tokyo)*. 2019; 59: 361-70.
150. Agarwalla PK, Stapleton CJ, Phillips MT, Walcott BP, Venteicher AS and Ogilvy CS. Surgical outcomes following encephaloduroarteriosynangiosis in North American adults with moyamoya. *J Neurosurg*. 2014; 121: 1394-400.

151. Chiu R, Chaker A, McGuire LS, et al. Socioeconomic Inequities in the Surgical Management of Moyamoya Disease. *World Neurosurg.* 2021.
152. Ghaffari-Rafi A, Ghaffari-Rafi S and Leon-Rojas J. Socioeconomic and demographic disparities of moyamoya disease in the United States. *Clin Neurol Neurosurg.* 2020; 192: 105719.
153. Dusick JR, Gonzalez NR and Martin NA. Clinical and angiographic outcomes from indirect revascularization surgery for Moyamoya disease in adults and children: a review of 63 procedures. *Neurosurgery.* 2011; 68: 34-43; discussion
154. Matsushima T, Inoue T, Katsuta T, et al. An indirect revascularization method in the surgical treatment of moyamoya disease--various kinds of indirect procedures and a multiple combined indirect procedure. *Neurol Med Chir (Tokyo).* 1998; 38 Suppl: 297-302.
155. Mugikura S, Takahashi S, Higano S, Shirane R, Sakurai Y and Yamada S. Predominant involvement of ipsilateral anterior and posterior circulations in moyamoya disease. *Stroke.* 2002; 33: 1497-500.
156. Feghali J, Xu R, Yang W, et al. Differing Surgical Outcomes in a Multiethnic Cohort Suggest Racial Phenotypes in Moyamoya Disease. *World Neurosurg.* 2019; 128: e865-e72.
157. Hishikawa T, Tokunaga K, Sugiu K and Date I. Clinical and radiographic features of moyamoya disease in patients with both cerebral ischaemia and haemorrhage. *Br J Neurosurg.* 2013; 27: 198-201.
158. Stickland RC, Zvolanek KM, Moia S, Ayyagari A, Caballero-Gaudes C and Bright MG. A practical modification to a resting state fMRI protocol for improved characterization of cerebrovascular function. *Neuroimage.* 2021; 239: 118306.
159. Moia S, Stickland RC, Ayyagari A, Termenon M, Caballero-Gaudes C and Bright MG. Voxelwise optimization of hemodynamic lags to improve regional CVR estimates in breath-hold fMRI. *Annu Int Conf IEEE Eng Med Biol Soc.* 2020; 2020: 1489-92.
160. Ma J, Liu Y, Ma L, Huang S, Li H and You C. RNF213 polymorphism and Moyamoya disease: A systematic review and meta-analysis. *Neurol India.* 2013; 61: 35-9.
161. Kalinowski L, Dobrucki IT and Malinski T. Race-specific differences in endothelial function: predisposition of African Americans to vascular diseases. *Circulation.* 2004; 109: 2511-7.
162. Carnethon MR, Pu J, Howard G, et al. Cardiovascular Health in African Americans: A Scientific Statement From the American Heart Association. *Circulation.* 2017; 136: e393-e423.

163. Cogswell PM, Lants SK, Davis LT, Juttukonda MR, Fusco MR and Donahue MJ. Vessel Wall and Lumen Features in North American Moyamoya Patients. *Clin Neuroradiol.* 2020; 30: 545-52.
164. Patel PD, Velazquez JL and Arora RR. Endothelial dysfunction in African-Americans. *Int J Cardiol.* 2009; 132: 157-72.
165. Vaclavu L, Meynart BN, Mutsaerts H, et al. Hemodynamic provocation with acetazolamide shows impaired cerebrovascular reserve in adults with sickle cell disease. *Haematologica.* 2019; 104: 690-9.
166. Thamm T, Guo J, Rosenberg J, et al. Contralateral Hemispheric Cerebral Blood Flow Measured With Arterial Spin Labeling Can Predict Outcome in Acute Stroke. *Stroke.* 2019; 50: 3408-15.
167. Lu H and van Zijl PC. A review of the development of Vascular-Space-Occupancy (VASO) fMRI. *Neuroimage.* 2012; 62: 736-42.
168. An H and Lin W. Impact of intravascular signal on quantitative measures of cerebral oxygen extraction and blood volume under normo- and hypercapnic conditions using an asymmetric spin echo approach. *Magn Reson Med.* 2003; 50: 708-16.
169. Morris EA, Juttukonda MR, Lee CA, et al. Elevated brain oxygen extraction fraction in preterm newborns with anemia measured using noninvasive MRI. *J Perinatol.* 2018.
170. Yablonskiy DA and Haacke EM. Theory of NMR signal behavior in magnetically inhomogeneous tissues: the static dephasing regime. *Magn Reson Med.* 1994; 32: 749-63.
171. Ropele S and Langkammer C. Iron quantification with susceptibility. *NMR Biomed.* 2017; 30.
172. An H and Lin W. Cerebral oxygen extraction fraction and cerebral venous blood volume measurements using MRI: effects of magnetic field variation. *Magn Reson Med.* 2002; 47: 958-66.
173. Donahue MJ, Sideso E, MacIntosh BJ, Kennedy J, Handa A and Jezzard P. Absolute arterial cerebral blood volume quantification using inflow vascular-space-occupancy with dynamic subtraction magnetic resonance imaging. *J Cereb Blood Flow Metab.* 2010; 30: 1329-42.
174. Weisskoff RM and Kiihne S. MRI susceptometry: image-based measurement of absolute susceptibility of MR contrast agents and human blood. *Magn Reson Med.* 1992; 24: 375-83.
175. Kellman P and McVeigh ER. Image reconstruction in SNR units: a general method for SNR measurement. *Magn Reson Med.* 2005; 54: 1439-47.

176. Yablonskiy DA. Quantitation of intrinsic magnetic susceptibility-related effects in a tissue matrix. Phantom study. *Magn Reson Med.* 1998; 39: 417-28.
177. Fan AP, An H, Moradi F, et al. Quantification of brain oxygen extraction and metabolism with [(15)O]-gas PET: A technical review in the era of PET/MRI. *Neuroimage.* 2020; 220: 117136.